BROWNIAN DYNAMICS SIMULATION OF DILUTE POLYMER CHAINS

by

Semant Jain

A dissertation submitted in partial fulfillment
of the requirements for the degree of
Doctor of Philosophy
(Chemical Engineering)
in The University of Michigan
2008

Doctoral Committee:

Professor Ronald G. Larson, Chair
Professor Robert M. Ziff
Associate Professor Jens-Christian D. Meiners
Assistant Professor Michael Mayer

“Are you doing what you are supposed to be doing
or are you doing the same old rubbish?”

~ Steve McFarren
Coach, University of Michigan Ballroom Dance Team

Dedication

To Mom & Dad

Acknowledgements

During the four years of my PhD research, I have been helped by several people whose assistance I would like to gratefully acknowledge. First and foremost, I would like to thank Professor Ronald G. Larson for accepting me into his group in the middle of the academic year. Having learned so much from his penchant for ensuring the most-minute details were thoroughly checked, I consider having had a chance to do research under his guidance a true privilege. He was always available for discussion even while he was traveling and his incredibly busy schedule. His assistance has been invaluable while I was writing my research papers, preparing oral and poster presentations for conferences, and rehearsing research seminars for job interviews. He has truly been a wonderful thesis advisor and after graduation I will miss him.

I am also very grateful to Professor Robert M. Ziff, Associate Professor Jens-Christian D. Meiners, and Assistant Professor Michael Mayer for serving on my committee. I have always appreciated their advice be it in my preliminary meeting, annual review, or data meeting. In particular, I would like to mention Professor Robert M. Ziff who was also the department's graduate program chair. He was the first faculty member at University of Michigan with whom I came in contact with and his warm personality came through from the very beginning—in the emails and telephone conversations I had with him when I was in India—which made me feel that I would

enjoy my time at Michigan. I will remain indebted to him for offering me a position in his group while Professor Larson was considering my application. He was always checking on how things were proceeding whenever I used to run into him in the corridor or over the several lunches I had with him at the Indian restaurants. Finally, I am very grateful to him for awarding me the Rackham's Dissertation Fellowship from the department's block grant allocation which funded my final semester.

I have also had the pleasure of interacting with some other faculty members at Michigan such as Associate Professor Nicholas A. Kotov who offered me a fully funded research assistant position in his group when I was in the midst of changing groups. Again, when I was looking for a 50% Graduate Student Instructor appointment, he readily accepted my application. Among other professors would be Professor Johannes W. Schwank who was always a source of inspiration and excitement in his class and while I was working with him on converting my term project into a research paper. Of the different professors for whom I have served under as a Graduate Student Instructor, I thoroughly enjoyed working for Associate Professor Michael J. Solomon whose organization and coordination skills made the task so much easier. I have also had the good fortune of interacting with Dr. Susan Montgomery as the Undergraduate Program Advisor who always offered very useful advise when I was a Graduate Student Instructor.

By no means could my graduate studies have been completed without the help of my friends. I had vital input from Anshuman Roy, Nimisha Srivastava, and Tudor Stoenescu whenever I had to make some critical decisions. Additionally, discussions with Larson group members such as Bruce Schiamberg, Chih Chen Hsieh, and Zuowei Wang were always very insightful and helpful. In my final years at Michigan, I was paired with

Dr. Allise Wachs and Paul Nkansah as my mentors through the College of Engineering's mentorship program. I am very thankful to them for having shared exceptionally useful career advice and for having spent their time so generously with me.

I have always had the support of the staff members at the Department of Chemical Engineering. Notably, Susan Hamlin's efficiency and knowledge of University of Michigan's system was always amazing. Other staff members such as Michael Africa, Melissa Bowers, Leslie Cypert, Shelley Fellers, Christine Moellering, Claire O'Connor, and Rhonda Sweet were also invariably obliging.

In the wider university community, the International Center has served as an incredible resource offering indispensable counsel in my cultural transition to United States. I have always appreciated the social events and trips organized for international students, especially during thanksgiving and Christmas, by the Enumenical Center and International Residence. Specifically, I would like to acknowledge Robert "Bob" E. Smith and Carole J. Smith for being my 2006 Thanksgiving host family.

Finally, I would like to recognize the assistance provided by Sweetland Writing Center for editing my research reports and papers. Singularly, I am very grateful to Barbara Ohrstrom and Dr. Kendrick Matthew "Matt" Kelley who taught me so much about writing in the countless writing workshops I had with them.

Table of Contents

List of Tables

List of Figures

List of Symbols

Abbreviations

$\overset{0}{A}$	Angstrom, 10^{-10} m.
ds	Double strand.
HI	Hydrodynamic interaction effect.
MSD	Mean square displacement (m^2).
nm	Nanometer, 10^{-9} m.
RMS	Root mean square.
ss	Single strand.

Letters

a	Bead radius (m).
a_n	Parameter in the rotational potential (n = 0, 1, …, 5) (-). Defined in equation 34.
b	Spring length (m).
b_K	Kuhn length (m).
C_∞^B	Contribution to the characteristic ratio from the bending force (-). Defined in equation 52.
C_∞^T	Contribution to the characteristic ratio from the rotational force (-). Defined in equation 53.
$\cos\phi_i$	Cosine of the i^{th} torsional angle (-).
$\langle\cos\phi\rangle$	Average of the cosine of the torsional angle (-).
$\langle\cos\theta_C\rangle$	Average value of the cosine of the complementary bending angle (-).
$\cos\theta_i$	Cosine of the i^{th} bending angle (-). Defined in equation 25.
$\langle\cos\theta\rangle$	Average of the cosine of the bending angle (-).
$d_{i,j}^E$	MSD for the j^{th} strand measured experimentally at the i^{th} observation point (m^2).
D	Total simulation duration (s).
D_G	End-monomer diffusion coefficient (in Chapter 2) (m^2/s). Defined in equation 7.
D_G	Center-of-mass diffusion coefficient (in Chapter 3) (m^2/s).
$d_{i,j}^{NM}$	MSD for the j^{th} strand computed using normal mode analysis at the i^{th} observation point (m^2).
$\underline{F}_B^i$	Bending force acting on the i^{th} bead (N). Defined in equation 37.

$\underline{F}_R^i$	Random brownian force acting on the i^{th} bead (N). Defined in equation 35.
$\underline{F}_S^i$	Stretching force acting on the i^{th} bead (N). Defined in equation 36.
$\underline{F}_T^i$	Rotational torsional force acting on the i^{th} bead (N). Defined in equation 42.
G_R'	Reduced storage modulus (-). Defined in equation 13.
G_R''	Reduced loss modulus (s^{-1}) . Defined in equation 14.
$g(r,s)$	Radial distribution function (m^{-3}). Computed as shown in equation 74.
h^*	Hydrodynamic interaction (-). Defined in equation 1.
H	Hookean spring constant (J). Defined in equation 58.
i	Experimental observation number (-).
j	Strand number ($j=1 \equiv 2400 \ \ bases, j=2 \equiv 6700 \ \ bases, j=3 \equiv 23100 \ \ bases$).
k	Normal mode number (-).
k_B	Boltzmann constant (1.38065 x 10^{-23} m^2 kg s^{-2} K^{-1}).
ℓ^i	i^{th} bond length (m).
ℓ_0	Equilibrium bond length, 1.53 x 10^{-10} m.
ℓ	Length of a ss-DNA base (m).
L	Total length of the ss-DNA strand (m).
L	Fully extended length of a polymer chain (m). Defined in equation 66.
m	Mass of a bead (in Chapter 2) (Dalton).
m	Slope of mean square displacement versus averaging interval (in Chapter 3) (m^2/s).
$\underline{m}$	Cross product of the vectors connecting beads i, j, and k. Computed as shown in equation 27.
n	Number of bases in the ss-DNA strand (-).
$\underline{n}$	Cross product of the vectors connecting beads j, k, and l. Computed as shown in equation 28.
N_K	Total number of Kuhn steps (-).
$N_{K,S}$	Number of Kuhn steps per spring (-).
N_j^O	Number of observation points for the j^{th} strand from Shusterman et al.'s data.
N_S	Number of springs (-).
$p(\phi)$	Probability distribution function for the torsional angle (rad^{-1}). Defined in equation 54.
$p(\theta)$	Probability distribution function for the bending angle (rad^{-1}).
$p(\phi_0)$	Probability of the torsional angle having a value ϕ_0 (-).
$p(\theta_0)$	Probability of the bending angle having a value θ_0 (-).
p_{G^-}	Probability of finding a torsional bond in the gauche$^-$ state (-).
p_{G^+}	Probability of finding a torsional bond in the gauche$^+$ state (-).
p_T	Probability of finding a torsional bond in the trans state (-).
$\underline{q}_k$	Normal mode coordinate defined using Fixman's approach (m). Computed as shown in equation 68.

$\langle q_k q_k(s) \rangle$	Normal mode autocorrelation function (-). Computed as shown in equation 67.
$\sqrt{\langle R^2 \rangle_0}$	Equilibrated end-to-end spring length (m). Defined in equation 20.
$\underline{r}^i$	Position vector for the i^{th} bead (m).
R_g	Radius of gyration (m). Defined in equation 19.
r_k^i	k^{th} coordinate of the i^{th} bead (m).
T	Solvent temperature (K)
U_{RD}	Ratio of the radius of gyration to the hydrodynamic radius (-). Defined in equation 18.
$U_{\eta\tau}$	Ratio of the characteristic relaxation time to the longest relaxation time (-). Defined in equation 21.
$\underline{R}(t)$	End-to-end vector for the polymer at time t (m).
$\underline{R}_S^i$	Spring vector for the i^{th} bond (m).
$\langle R^2 \rangle_0$	Mean-square end-to-end distance for the polymer chain (m^2). Defined in equation 65.
$\langle R^2 \rangle_{0,S}$	Mean-square end-to-end distance for a spring (m^2). Computed as shown in equation 59.
$\langle RR(s) \rangle\|_{\text{Sim}}$	End-to-end vector autocorrelation function from simulations (-). Computed as shown in equation 55.
$\langle RR(s) \rangle\|_{\text{Th}}$	End-to-end vector autocorrelation function from theory (-). Computed as shown in equation 61.
$\langle R_S R_S(s) \rangle\|_{\text{Sim}}$	Spring vector autocorrelation function from simulations (-). Computed as shown in equation 60.
$\langle R_S R_S(s) \rangle\|_{\text{Th}}$	Spring vector autocorrelation function from theory (-). Computed as shown in equation 64.
s	Averaging interval for the autocorrelation function (s).
$S(q,s)$	Scattering function defined for the case of dilute polymer chains in equations 72 and 73.
T	Temperature (K).
$\langle uu(s) \rangle\|_{\text{Sim}}$	Unit spring vector autocorrelation function from simulations (-). Computed as shown in equation 56.
$\langle uu(s) \rangle\|_{\text{Th}}$	Unit spring vector autocorrelation function from theory (-). Computed as shown in equation 63.
$\underline{u}^i$	Unit spring vector (m). Computed as shown in equation 24.
$V_{\phi=0^0}, V_T$	Potential of the trans state (J/mol).
$V_{\phi=\pm 60^0}, V_{GT}$	Potential of the barrier state between the gauche$^{\pm}$ and trans states (J/mol).
$V_{\phi=\pm 120^0}, V_G$	Potential of the gauche$^{\pm}$ states (J/mol).
$V_{\phi=\pm 180^0}, V_C$	Potential of the cis state (J/mol).

V_B^i	Bending potential for the i^{th} bending angle (J).
V_S^i	Stretching potential for the i^{th} bond.
V_T^i	Rotational potential for the i^{th} torsional angle (J).
$\overline{X_k}(t)$	Normal mode autocorrelation function definition using equations in Krushev et al., 2002. Computed as shown in equation 71.

Greek

β	Ratio of the frictional constant to the bead mass (s^{-1}).
β^2	Inverse of mean square end-to-end distance for a spring, $3/2\langle R^2\rangle_{0,S}$ (m^{-2}). Defined in equation 59.
$\varepsilon_{I,j}$	RMS error for the j^{th} strand alone (-). Defined in equation 15.
ε_S	RMS error for the 2400 and 6700 strands (-). Defined in equation 17.
ε_G	RMS error for the 2400, 6700, and 23100 strands (-). Defined in equation 16.
ϕ_i	i^{th} torsional angle (rad).
γ_θ	Bending potential constant (J).
γ_ϕ	Rotational potential constant (J).
γ_S	Stretching potential constant (kg s^{-2}).
η_S	Solvent viscosity (Pa s).
λ_i	Relaxation frequency (s^{-1}).
θ_C	Complementary of the bending angle (rad), $\theta_C \equiv \pi - \theta$, as defined in equation 25.
θ_i	i^{th} bending angle (rad). Defined in equation 25.
θ_0	Ideal bending angle, $109^0 47'$ or 2.578 rad.
τ_0	Characteristic relaxation time (s).
τ_i	i^{th} relaxation time (s).
τ_p	Rotational relaxation time (s). Theoretical definition in equation 62.
ν_F^k	Relaxation rate corresponding to the k^{th} normal mode using Fixman's definition (s^{-1}). Computed as shown in equation 67.
ν_K^k	Relaxation rate corresponding to the k^{th} normal mode using Krushev's definition (s^{-1}). Computed as shown in equation 70.
ω	Oscillation frequency (Hz).
ζ	Drag coefficient (kg/s). Defined in equation 2.
ζ_T	Total frictional drag for the chain (kg/s).

Abstract

Local motion of polymers is extremely important while studying the behavior of single strand DNA in DNA unzipping and replication, understanding rheological properties of polymers in confined in narrow gaps for head-disk interface design for hard disk drives, and designing membrane structure for small molecule permeation through a dense polymeric membrane. So, in order to understand the mechanism of energy dissipation of dilute polymer solutions at high frequencies, I carry out a Brownian dynamics study of a linear bead-spring chain in which the beads represent individual backbone atoms, a stiff Fraenkel spring potential maintains the distance between atoms near 1.53 $\mathring{A}$, a bending potential maintains tetrahedral bonding angles, a torsional potential imposes realistic barriers to torsional transitions, and white noise represents the Brownian force from the solvent. With this model, I find that the end-to-end vector autocorrelation function from the simulation is in excellent agreement with the theoretical Rouse model predictions. Nevertheless, the autocorrelation function of the bond orientation vectors—which delineates the relaxation of the stress tensor—exhibits a much slower decay then predicted by the coarse-grain Rouse theory except near the longest relaxation time even for chains with as many as 50 bonds. I find that both the bending and torsional potentials slow down the contributions of local relaxation modes, bringing

the relaxation of short chains (less than 50 bonds) closer to single exponential behavior than to the Rouse spectrum, in qualitative agreement with observations of birefringence relaxation [Lodge et al. (1982) *J. Poly. Sci.* **20**, 1409]. Also, my normal mode predictions using the bead-spring model provides an excellent fit to data for 2400 and 6700 base single-strand DNA molecules [Shusterman et al. (2004) *Phy. Rev. Lett.* **92**(4), 048303] and the fit yields 12 Kuhn steps per spring and a value of 0.12 for the standard hydrodynamic interaction parameter—very close to the values typical of conventional polymers such as polystyrene. Thus, my results are generally in agreement with a recent notion of a "dynamical Kuhn length" in which torsional barriers to chain motion, can suppress high frequency contribution to viscoelasticity [Larson (2004) *Macromol.* **37**, 5110].

Chapter 1

Introduction

The long chain nature of polymers causes polymer motion to extend over many orders of magnitude in time from vibrations at picoseconds, high frequency torsional and vibrational behavior, up to the slow reorientation of whole molecules approaching macroscopic times [1]. Thus, study of local motion is expected to further the understanding of the chemical structure so that mechanical properties and material response during processing can be improved. However, in order to account for local effects, bending and torsional effects must be taken into account explicitly which has not been done in the standard coarse-grained models that have been used for carrying out theoretical analysis on polymers. Such a local microscopic analysis is also relevant in understanding rheological properties of polymers confined in narrow gaps of the order of 1 nm for designing head-disk interface of high recording hard disk drives [2]. In such small confines, the polymer behavior is significantly different from that in the bulk. Another application of this work is in furthering the understanding of solution-diffusion concept using which small molecules in the liquid state permeate through a dense polymeric membrane. In a process like this, understanding the membrane structure

enables researchers to better the membrane design and performance [3]. In processes such as DNA unzipping, where the double strand unravels into single strands, while extensive experimental and theoretical work has been carried out on double strand DNA, much less attention has been devoted to single strand DNA. Once again, similar to other polymers, in order to carry out a theoretical analysis on ss-DNA, the local bond motion need to taken into account explicitly.

The slow dynamics of polymers in dilute solution are well described in the linear viscoelastic regime by the decades-old Rouse-Zimm theory [4, 5] which coarse-grains a polymer chain into a sequence of frictional beads connected by Hookean springs. Such a description is not expected to capture fast dynamics dominated by the local motions of one or a few backbone bonds since at long time scales such dynamics are expected to be subsumed into the effective bead drag coefficient and spring constant of the bead-spring chain. The success of this approach has been demonstrated in numerous comparisons of the bead-spring model to experimental data for long polymers in dilute solution [6].

What remains unresolved is the manner in which this coarse-grained bead-spring model breaks down at shorter time and distance scales than those for which linear 'springs' capture reasonably well the configurations of the chain. One might expect that at short times (or high frequencies) viscoelastic experiments would show indications of high-frequency modes that are controlled by motions of small groups of bonds that are influenced by bending and torsional potentials. Nevertheless, very surprisingly, experiments by Schrag, Lodge, and coworkers [7-9] have shown that the Rouse-Zimm [4, 5] bead-spring chain model can describe reasonably well the entire frequency range of dilute polystyrene or polyisoprene chains—even at frequencies high enough that single

springs are expected to be strongly excited. This is true as long as the number of springs is chosen so that each spring represents a sub-molecule of molecular weight 4500 $\pm$ 500 for the case of polystyrene [6] and 2400 for polyisoprene [9] which in both cases corresponds to around 100 backbone bonds. In contrast, both experiments and simulations in melts show multiple 'local' modes associated with relaxation of individual or small groups of bonds which couple to similar relaxations of bonds of neighboring chains [9-13]. What is mysterious is why such modes do not appear in the viscoelastic measurements of dilute polymer solutions.

First, in order to test this observation on other polymers, I carry out a study on single strand DNA (ss-DNA). ss-DNA can also be thought of as an ordinary polymer as long as its tendency to self-base-pair is suppressed by using highly alkaline conditions and somewhat elevated temperatures [14]. This work followed the recent development of optically visible DNA as a model polymer molecule which was one of the four major contributors to the rapid progress in the quantitative prediction of molecular deformation and stretching [15].

ss-DNA's small persistence length makes it even more similar to ordinary synthetic polymers such as polystyrene than is double stranded DNA. Recently, Shusterman et al. [14, 16] reported for the first time the stochastic motion of individual monomers within isolated single- and double-stranded DNA. By attaching a fluorescent label specifically to a single base at the end of the chain, they used fluorescence correlation spectroscopy to monitor the motion of 2400, 6700, and 23100 base ss-DNA polymers in dilute solutions (0.03 to 0.3 molecules in an average confocal microscopy volume). This yielded data containing essentially the same information as linear

viscoelastic rheological measurements. Strand separation was achieved by maintaining an extremely alkaline condition (pH = 12.3) and an elevated temperature (37^0 C). Thereafter, the authors measured the end monomer's mean square displacement (MSD) over five decades in time interval, Δt, and found two distinct power-law regions. In one regime, encompassing intermediate times (Δt = 5 - 40 x 10^{-3} s), the MSD exhibited a slope of 0.69, which is similar to that predicted by the Zimm model for theta solvents in the non-draining limit where the slope is 2/3. At long times (Δt > 40 x 10^{-3} s), the mean square displacement (MSD) was found to be linear in Δt and described the bulk diffusion of the coil as a whole. Here, 'time' is used as a short-hand for 'time interval' between measurements of monomer positions. Viscoelastic measurements for ss-DNA can be computed using the bead-spring model by invoking a normal mode approximation with pre-averaged hydrodynamic interaction. Amelar et al.'s work [6] on polystyrene in Aroclor 1248 is an example of a successful demonstration of the use of normal modes to predict polymer properties. Hence, I use the normal mode analysis to predict the chain-end diffusion behavior of ss-DNA. I follow this by comparing the bead-spring model parameters for ss-DNA to those for polystyrene and find that ss-DNA's hydrodynamic parameters are similar to those of polystyrene.

Next, I find suggestions in literature [13, 17] that torsional barriers to bond rotation might confer a large 'dynamic stiffness' to polymers that slows down modes requiring fast bond motion causing their relaxation to overlap with the terminal zone for short chains. This might occur only in dilute solutions, and not in the melt, because in the melt the diffusive motions of the chain are on length scales larger than that of bond rotation. Additionally, the high friction of the medium in melts slows down the bond

rotations more than the local bonds. As a result, in the melt (but not in dilute solution), the local rotational barriers can be surmounted faster than diffusive relaxation on longer length scales can occur. Hence, the relaxation of local modes can be temporally distinguished from the longer-range, diffusive modes.

To test such ideas and to better understand the mechanism of energy dissipation at high frequencies in dilute solutions, one must study a polymer chain model that endows each short backbone bond with realistic bending and torsional angle restrictions [17]. Therefore, I conduct a Brownian dynamics study of a linear polymer chain in which the beads represent individual backbone atoms, stiff Fraenkel spring forces maintain the distance between atoms at 1.53 $\overset{0}{\text{A}}$, bending forces maintain tetrahedral bonding with a bending angle of 109^0 47', torsional forces maintain realistic barriers to torsional transitions. I also add white noise that represents the Brownian force from the solvent. Then, I collate my calculations of the end-to-end vector and individual spring vector autocorrelation functions predicted by Brownian dynamics simulations using this model to that foretold by the theoretical coarse-grained Rouse model. In addition, I reckon the relaxation rates and amplitudes for all modes and contrast my estimations to theoretical predictions and simulations carried out for the melt state described in literature. Finally, I also work out the time dependent scattering function, $S(q,t)$, from the model and discuss how these results differ from both the Rouse-Zimm theory and experimental data.

Chapter 2

Single-strand DNA as a dilute polymer chain

In physics, the equations are deterministic. When systems are too complex to be described in detail, or a detailed description is too difficult to handle, a stochastic aspect is introduced to model incomplete knowledge. Thus, possible macro states characterized by coarse-grained variable(s) are presented in place of a full detailed microstate [18]. The Langevin equation, an example of a stochastic differential equation, describes the highly irregular motion of a Brownian particle as a result of collisions with the many small surrounding molecules. Peters (2000) stated that even if the initial trajectory of the Brownian particle is kept identical in all experiments, having the same initial trajectory of all the solvent particles would be beyond control [18]. In cases such as this, where the deterministic repetition of experiments is not possible, an averaged description is preferred. In this chapter, I describe the standard coarse-graining techniques that have been used for understanding viscoelasticity of dilute polymer chains and how I adapt them to understand the behavior of single-strand DNA.

2.1. Coarse graining

For describing the rheological behavior of polymers, the overall architecture is more important than the chemical composition of monomers [19]. The level of coarse-graining required to simulate a polymer is set by the requirement that the coarse-grained model must retain enough fine-scale features to represent the configuration distribution in sufficient detail to provide accurate values of forces and stresses. The most commonly used coarse-grained models of polymer chains are the bead-rod and the bead-spring models.

A freely jointed bead-rod chain—also called Kramer's (1946) chain [20] —is a model for a linear polymer chain. In the model, the beads act as discrete sources of friction, the joints are fully flexible, and the rods provide rigid constraints on the motion of the beads. The rods hold up the beads at a constant relative distance and since they physically correspond to one Kuhn [21-23] step, they act as the smallest rigid length scale in the model [18]. With statistical mechanics as the basis, the force required to increase the chain separation has been shown [24-26] to be proportional to the end-to-end distance, i.e., the entropic force behaves as a Hookean spring for small deformations. However, on account of the constraint on the rod length, a stochastic simulation of polymer models with rigid links combined with extremely irregular Brownian motion is more complex than bead-spring simulations. Of the two correct implementations [18] of the governing stochastic equations, the first 'naïve' approach gives the correct discretization but a more elegant solution was proposed by Ottinger (1994) [27] using the stochastic differential equations in a rigorous manner.

Real polymers are not freely jointed chains but a freely jointed chain will have the same equilibrium mean square end-to-end length, $\langle R^2 \rangle_0$, and fully extended length, L, as any real polymer in a theta solvent if the freely jointed step length, b_K, and the number of steps, N_K, of the freely jointed chain are chosen appropriately, i.e., $b_K^2 N_K = \langle R^2 \rangle_0$ and $b_K N_K = L$ [19, 28]. Figure 1 shows the bead-rod and bead-spring model coarse graining a polymer chain.

In very dilute solutions, the chains in the solvent fluid are separated far enough to ignore the interaction between the neighboring molecules. Examples of dilute solution polymer applications include fiber spinning and drag reduction by polymer additives. However, in dilute solutions, a few complicating non-local internal interactions can be distinguished [18, 28]:

- Hydrodynamic interaction (HI): This is defined as the motion of one part of a polymer chain creating disturbances in the solvent velocity field which can affect the drag exerted by the solvent on other parts of the same chain. The velocity field generated by the motion of one particle which is transmitted through the medium not only influences other particle's motion but also its hydrodynamic force, torque, and stresslet [29]. Figure 2 shows the manner in which the motion of all beads affects the motion of a single bead through HI.

  In the limit of linear viscoelasticity, the effect of hydrodynamic interactions can be seen through some parameters characterizing the flow. In a theta solvent, τ_1 scales as M^2 and $M^{1.5}$ while $[\eta]_0$ scales as M^1 and $M^{0.5}$ [30] when the HI effects are neglected and account for respectively. The scaling exponents have been found to decrease in the presence of HI because hydrodynamic coupling 'shield' one part of the chain

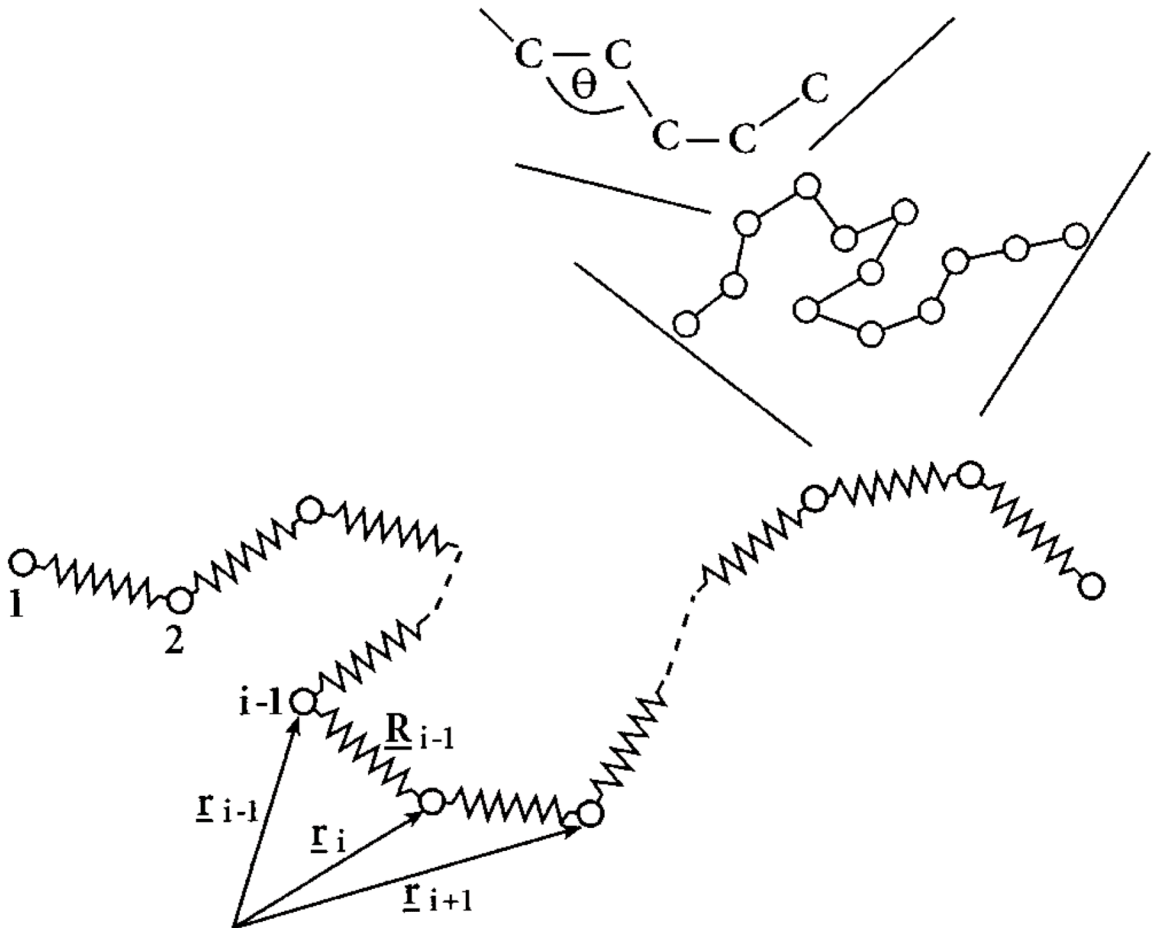

Figure 1. Illustration showing a real polymer chain with a carbon-carbon backbone containing bending and torsional angles being coarse grained onto a freely jointed bead-rod chain and further coarse graining of the bead-rod model onto a bead-spring chain (Larson, 2004).

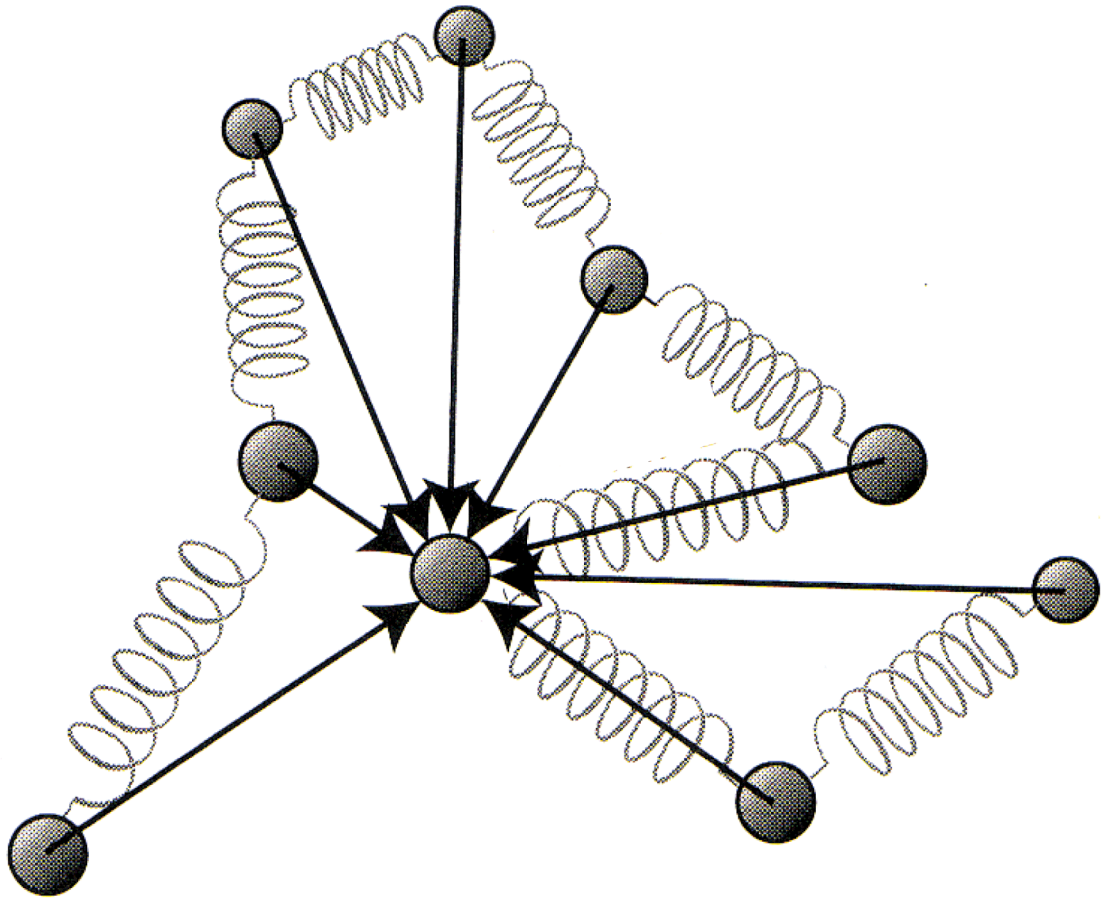

Figure 2. Illustration showing the motion of a bead being affected by all the other beads in the bead-spring chain through hydrodynamic interaction (Teraoka, 2002).

from another reducing drag on each part. As the molecular weight of the chain decreases, the 'shielding' effect becomes weaker. However, experiments down to 5000 Da—the lowest molecular weights investigated rheologically [6]—showed HI exerts a pronounced influence on linear viscoelasticity of even short chains.

- Excluded volume interaction: This is a short-range repulsion interaction between the atoms since they cannot occupy the same volume or space.
- Solvent effect: Depending on the chemical affinities of the solvent and the polymer thermodynamics might favor a polymer to be surrounded either by solvent molecules or by other polymer molecules. In case of a good solvent, the polymer coil extends itself; and in theta solvent, where the solvent and polymer share the same chemical composition, the balance is satisfied.
- Topological interaction: These interactions state that parts of polymer chain do not cross each other.

2.2. Bead-spring model

The bead-spring model replaces a polymer by $N_S + 1$ beads connected by N_S Hookean springs. These phantom springs are freely jointed and each represent enough monomers that the sub-chain end-to-end vectors obey Gaussian statistics [6]. The four model parameters are: a, the hydrodynamic radius of each bead, b, the root-mean-square length of each spring at equilibrium, N_S, the number of springs used to represent the chain, and η_S, the solvent viscosity. However, η_S is known for any particular solvent at a specified temperature, so the model parameters are essentially just three: a, b, and N_S.

From these independent parameters of the bead-spring model, the hydrodynamic interaction parameter, h^*, can be obtained as [6, 7]:

$$h^* = \frac{1}{\sqrt{12\pi^3}} \frac{\zeta}{b\eta_S} = \sqrt{\frac{3}{\pi}} \frac{a}{b} \tag{1}$$

where ζ, the drag coefficient, is defined as:

$$\zeta = 6\pi\eta_S a \tag{2}$$

Thus, I can alternatively specify the model parameters as: b, h^*, and N_S.

Accounting for hydrodynamic interactions (HI) in addition to the spring forces for all beads leads to a set of coupled integro-differential equations [5, 7]. However, using the approximate normal mode analysis with pre-averaged HI, the problem can be discretized into N_S independent equations—one for each of the N_S springs in the model. In this way, the predictions of the Rouse and Zimm models for the MSD can be obtained [14, 31].

In the bead-spring model, the characteristic frequency, λ_i, and relaxation time, τ_i, for the i^{th} mode for a polymer are related to each other by [7]:

$$\tau_i \lambda_i = \sqrt{\frac{\pi^3}{3}} \frac{\eta_S b^3 h^*}{k_B T} \tag{3}$$

where k_B is the Boltzmann constant and T is the solvent temperature.

Once the relaxation times are obtained, the following equations emerge for the mean square displacement of the p^{th} bead [32]:

$$\left\langle \left[r_{pp}(t) \right]^2 \right\rangle = 6D_G t + 24 \sum_{i=1}^{N_S} \frac{k_B T}{k_i} \left[\cos^2\left(\frac{ip\pi}{N_S} \right) \right] \left[1 - \exp\left(-\frac{t}{\tau_i} \right) \right] \tag{4}$$

The above equation can be simplified for the end beads (p = 1 or N_S+1) to:

$$\left\langle \left[r_{11}(t) \right]^2 \right\rangle = 6D_G t + 24 \sum_{i=1}^{N_S} \frac{k_B T}{k_i} \left[\cos^2 \left(\frac{i\pi}{N_S} \right) \right] \left[1 - \exp\left(-\frac{t}{\tau_i} \right) \right] \tag{5}$$

where

$$k_i = \frac{6\pi^2 k_B T}{N_S b^2} i^2 \tag{6}$$

and D_G represents the center-of-mass diffusion coefficient. For Gaussian chains and theta conditions, the center-of-mass diffusion coefficient is estimated through [6]:

$$D_G = \frac{k_B T}{\zeta} \left[\frac{1}{N_S + 1} + \frac{\sqrt{2^3} h^*}{(N_S + 1)^2} \sum_{j=1}^{N_S} \frac{N_S + 1 - j}{\sqrt{j}} \right] \tag{7}$$

While equation 7 (and the equations in this section) might seem to be valid only for theta solvents, the above equations have been commonly applied to good-solvent cases by adjusting the spring equilibrium length to be larger than theta dimension. This method, while not strictly valid for the scaling of coil size or diffusion coefficient with molecular weight, has been found to give good predictions for a range of molecular weights for common synthetic polymers such as polystyrene in Aroclor [6].

2.2.1. Calculation of relaxation modes

Based on the work of Lodge and Wu [7], I present a brief description of procedure to calculate the characteristic frequencies for an arbitrary number of springs by solving for the eigenvalues of an N_S x N_S symmetric matrix **B** whose elements are given as:

$$B_{pq} = H_{pq} + H_{p-1,q-1} - H_{p-1,q} - H_{p,q-1} \qquad p,\ q = 1,\ 2,...,\ N_S \tag{8}$$

where

$$H_{ij} = \begin{cases} 1 & i = j \\ h^* \sqrt{\dfrac{2}{|i-j|}} & i \neq j \end{cases} \quad i,j = 0,\ 1,\ 2,...,N_S \tag{9}$$

The N_S characteristic modes (frequencies) are the N_S roots λ (λ_1, λ_2, …, λ_S) of the equation:

$$\det\left(B_{pq} - \lambda\delta_{pq}\right) = 0 \tag{10}$$

2.2.2. Code validation

To solve for the eigenvalues, I write a code in Fortran based on Householder's method and the 'Q-R' method [33]. I validate my code by showing that the eigenvalues it generates are identical to the analytical values [7] for N_S = 1 or 2 and are in excellent agreement to Lodge and Wu's [7] tabulated characteristic frequencies for N_S = 2 to 300 with h^* varying from 0.05 – 0.2 (Figures 3 and 4).

Furthermore, in Figure 5, I find full agreement between data published in literature [6] to calculations using my model parameters and relaxation times for the intrinsic viscosity [6]:

$$[\eta] = \frac{RT}{M\eta_S} \sum_{k=1}^{N_S} \tau_k \tag{11}$$

where M is the molecular weight of the chain and η_S is the solvent viscosity. Similarly, I present in Figure 6 excellent agreement between published data [6] and my calculations for the infinite dilution diffusivity [6]:

$$D_0 = \frac{k_B T}{\zeta}\left[\frac{1}{N_S+1} + \left(\frac{1}{N_S+1}\right)^2 2^{1.5} h^* \sum_{j=1}^{N_S+1} \frac{N_S+1-j}{j^{0.5}}\right] \tag{12}$$

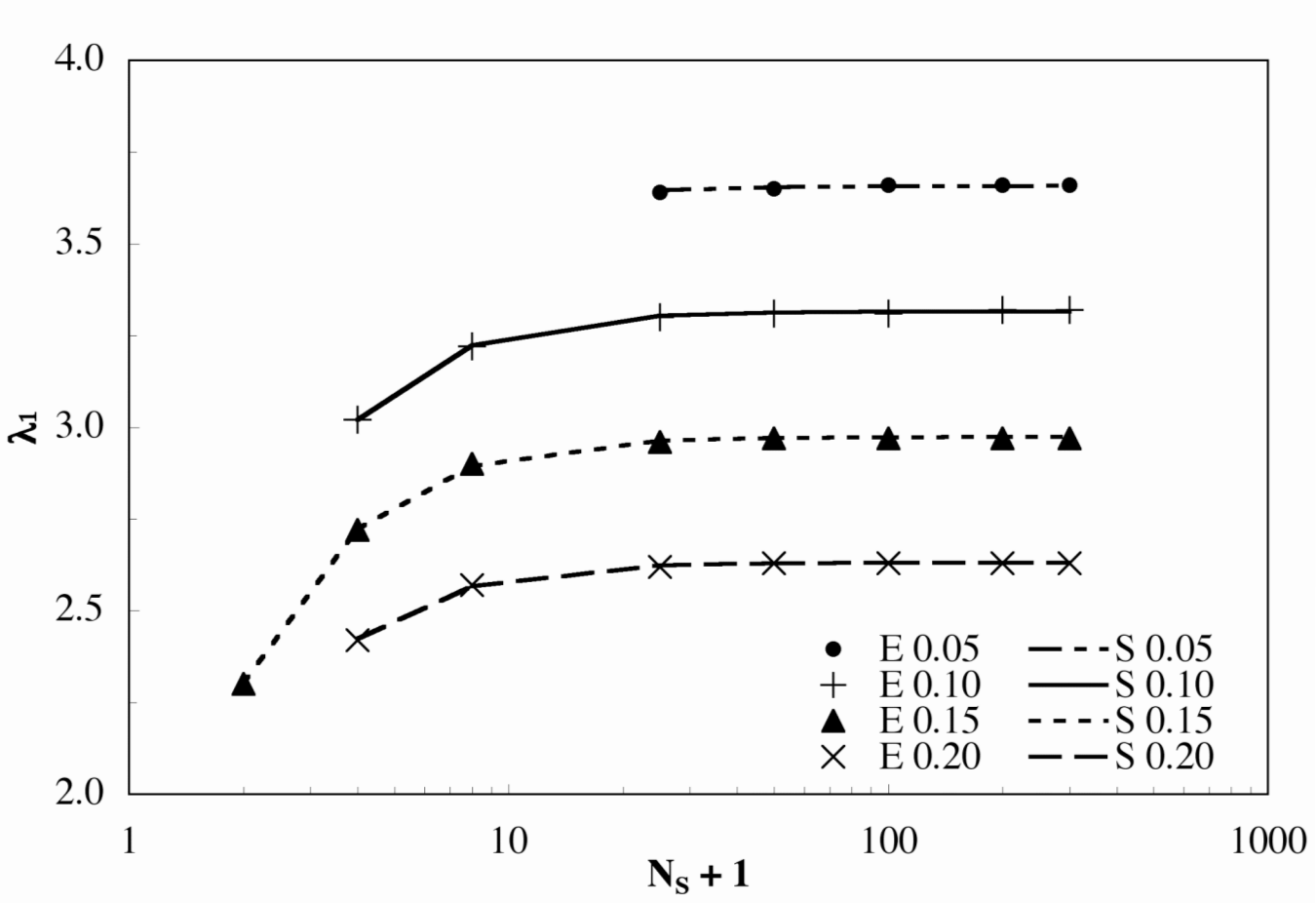

Figure 3. Comparison of the experimentally (E) computed longest characteristic frequency by Lodge and Wu (1971) to my corresponding simulation values (S) as a function of the number of beads, N_S+1, and the hydrodynamic interaction parameter, h^*, ranging from 0.05 to 0.20.

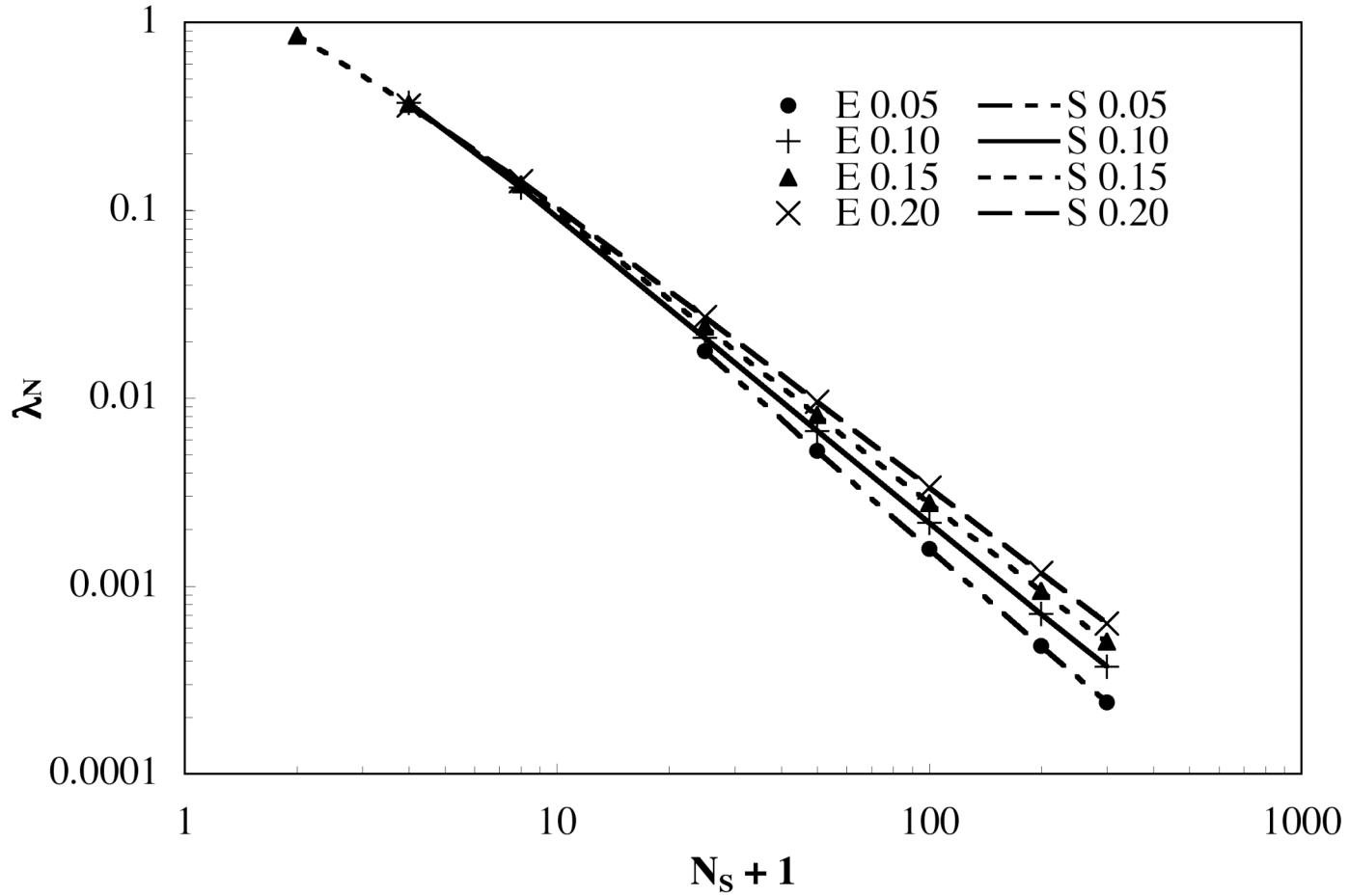

Figure 4. Comparison of the experimentally (E) computed shortest characteristic frequency by Lodge and Wu (1971) to my corresponding simulation values (S) as a function of the number of beads, N_S+1, and the hydrodynamic interaction parameter, h^*, ranging from 0.05 to 0.20.

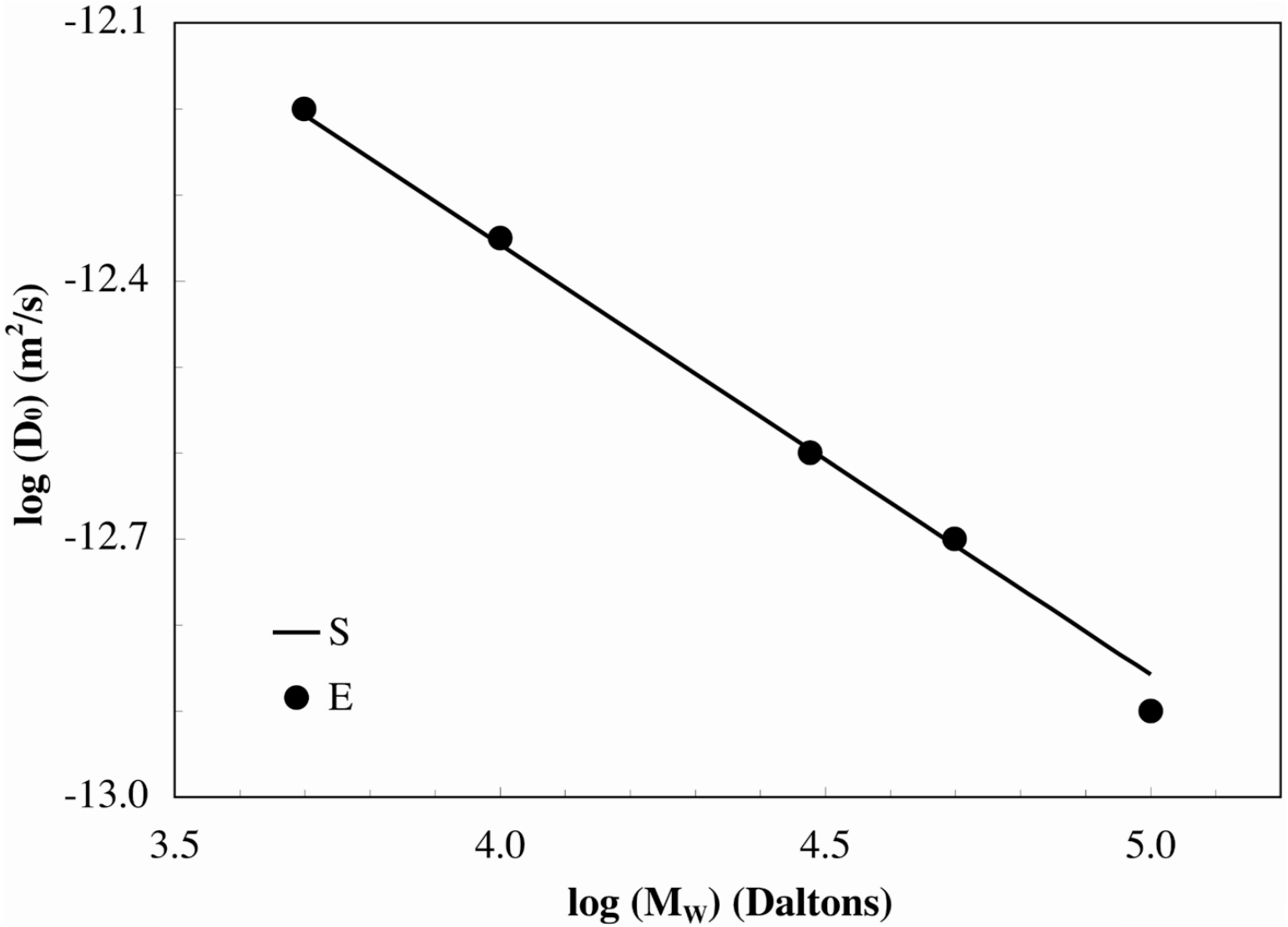

Figure 5. Comparison of the infinite dilution diffusivity, D_0, calculations for polystyrene by Amerlar et al. (1991) (E) to my corresponding simulation values (S) using a bead-spring model with $h^* = 0.15$, $b = 6 \times 10^{-9}$ m, and mass per spring, $M_S = 5000$ Daltons.

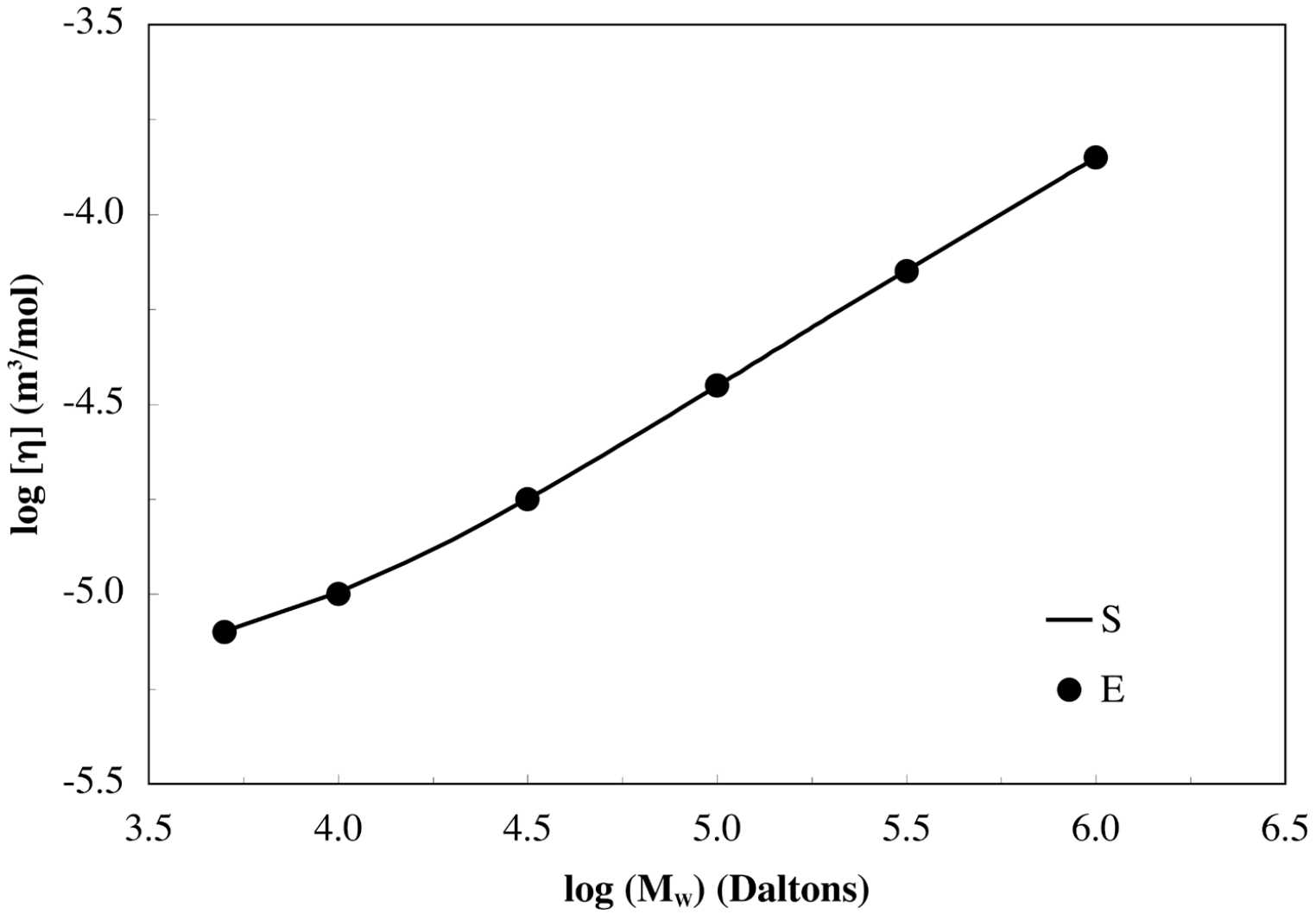

Figure 6. Comparison of the instrinsic viscosity, $[\eta]$, versus molecular weight, M_W, calculations for polystyrene in Arcolar 1248 at 25^{0}C by Amerlar et al. (1991) (E) using the bead-spring model with $h^* = 0.15$, $b = 6\text{x}10^{-9}$ m, and the mass of each spring, $M_S = 5000$ Daltons to my corresponding simulation values (S) using identical model parameters.

where ζ is the bead friction coefficient, 3.75 x 10^{-9} kg/s. The reduced storage and loss moduli can be computed from the relaxation times as [34, 35]:

$$G_R' = \sum_{i=1}^{N_S} \frac{\omega\tau_i^2}{1+\omega\tau_i^2} \tag{13}$$

and

$$G_R'' = \sum_{i=1}^{N_S} \frac{\omega\tau_i}{1+\omega\tau_i^2} \tag{14}$$

respectively. In these equations, ω is the oscillation frequency. When I plot these moduli in Figure 7 against the frequency multiplied by the characteristic relaxation time, $\tau_0 = \sum_{i=1}^{N_S} \tau_i$, my results match perfectly to the data and calculations of Johnson et al. [34, 35] for a polystyrene solution in a theta solvent.

2.2.3. Parameter optimization and error analysis

Now, I have enough information to begin analysis of the experimental data [14, 16] on single-strand DNA. To obtain the best-fit parameters, I need to carry out an optimization over all model parameters (b, N_S, and h^*). The first parameter—spring length—is initialized as the length of a base, l, and incremented in multiples of l. The second parameter—number of springs—starts off at unity and incremented in steps of one. The third parameter—hydrodynamic interaction strength—is initialized at 0 and incremented in steps of 0.01. h^* has a maximum value of 0.49 since any greater value would be physically unrealistic [19]. I then compute the MSD over the entire time domain using the parameter set under consideration. By stepping through parameter

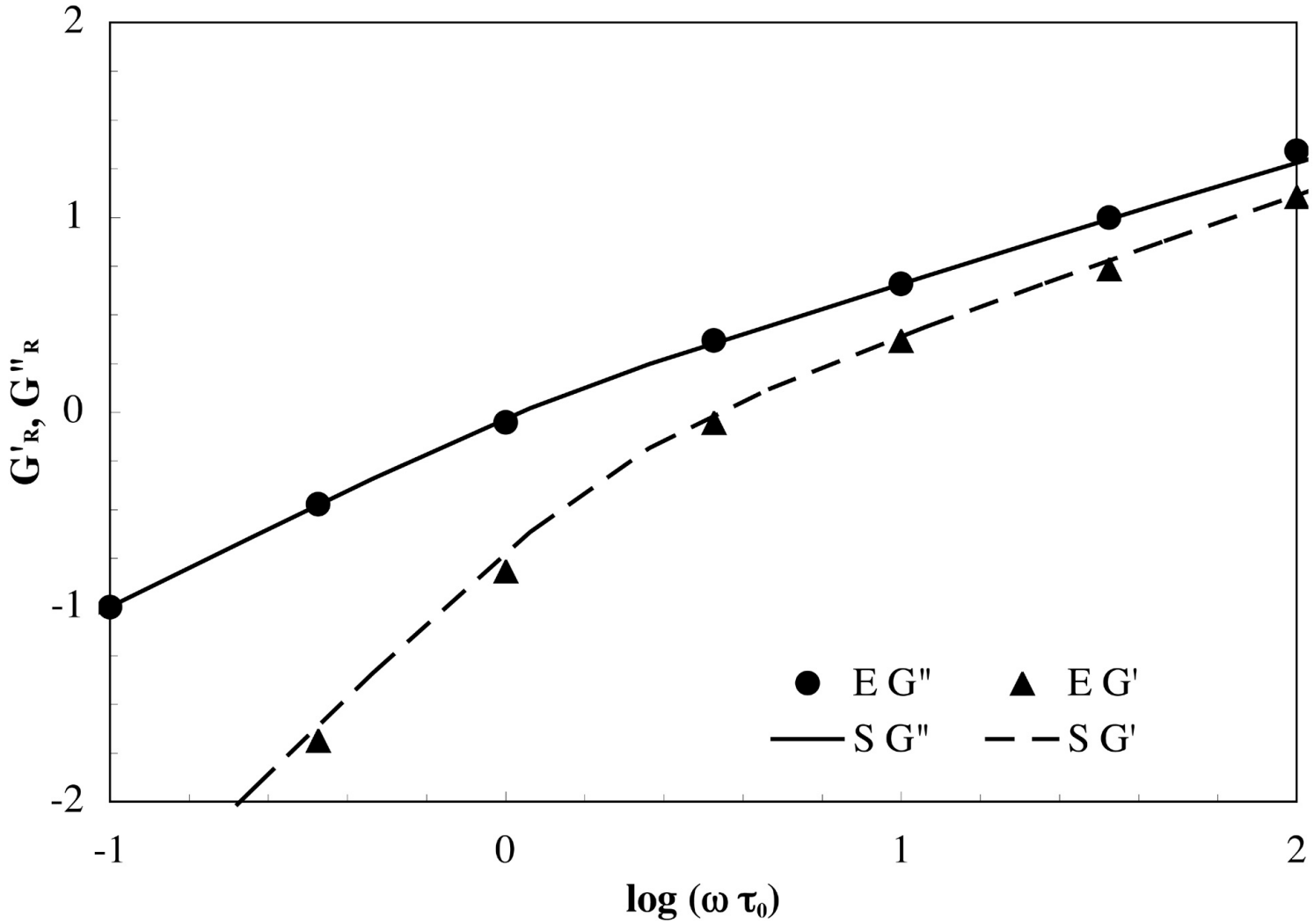

Figure 7. Comparison of the experimental data (E) collected by Johnson et al. (1970) of the reduced storage and loss modulii for polystyrene in Aroclor 1248 to my simulations (S) done using the bead-spring model.

values in a nested fashion, a through search of parameter space is carried out to find the global smallest difference between the theoretical and experimental MSD.

Specifically, to determine quantitatively the accuracy of the estimated parameters for a particular strand length, I compute the dimensionless root mean square error as:

$$\varepsilon_{I,j} = \sqrt{\frac{\sum_{i=1}^{N_j^O}\left(1 - d_{i,j}^{NM} / d_{i,j}^{E}\right)^2}{N_j^O}} \tag{15}$$

where $d_{i,j}^{NM}$ is the normal-mode-computed mean square displacement at the i^{th} observation point for the j^{th} strand, $d_{i,j}^{E}$ is the mean square displacement measured experimentally for the j^{th} strand at the i^{th} observation point, and N_j^O is the number of observation points for the j^{th} strand under consideration. Here, j refers to the DNA strand sequence number, i.e., j = 1 refers to 2400, j = 2 to 6700, and j = 3 to 23100 base ss-DNA. Based on fitting the experimental data supplied by one of the authors of Shusterman et al. [14, 16], I obtain N_1^O = 119, N_2^O = 131, and N_3^O = 131.

Similarly, I compute the global optimum error as:

$$\varepsilon_G = \sqrt{\sum_{j=1}^{3} \frac{\sum_{i=1}^{N_j^O}\left(1 - d_{i,j}^{NM} / d_{i,j}^{E}\right)^2}{3N_j^0}} \tag{16}$$

and the selectively scaled error for just strands 1 and 2 as:

$$\varepsilon_S = \sqrt{\sum_{j=1}^{2} \frac{\sum_{i=1}^{N_j^O}\left(1 - d_{i,j}^{NM} / d_{i,j}^{E}\right)^2}{2N_j^0}} \tag{17}$$

2.3. Results

2.3.1. Parameter fitting

Measurements of the mean square displacement data of ss-DNA were made by Shusterman et al. [14, 16] for three different strand lengths—2400, 6700, and 23100 base ss-DNA—which have been summarized in Figure 8. To predict properties for a given strand length, the bead-spring model uses the following parameters: η_S, h^*, b, and N_S. Of these parameters, η_S, the solvent viscosity, has the experimental value 6.9 x 10^{-4} Pa-s at 37^0 C. To obtain the remaining three model parameters, I run an optimization routine to identify the best-fit values under various constraints. I carry out the analysis in three parts.

First, I identify the global best-fit parameters for all the strands (2400, 6700, and 23100) and obtain $h^* = 0.14$, $b = 4.94$ x 10^{-8} m, and $N_S = 6$, 17, and 58 for the 2400, 6700, and 23100 base ss-DNA strands respectively. In this fit, the values of h^* and b are constrained to be identical for all molecules and N_S is proportional to number of bases in the DNA strand. I plot the resulting predictions in Figure 9. The experimental MSD of the 23100 base strand is almost identical to that of the MSD of the 6700 base strand at long times. Moreover, the MSD of the 23100 base strand follows a different slope—compared to the other shorter strands—at intermediate times. These observations lead me to believe that the experimental data of the longest chain are unreliable. One author [36] of the experimental work suggests insufficient denaturing conditions could have led to incomplete separation of the ss-DNA strands leading to intermittent formation of ds-DNA stretches. This phenomenon is most likely the cause of the anomalous

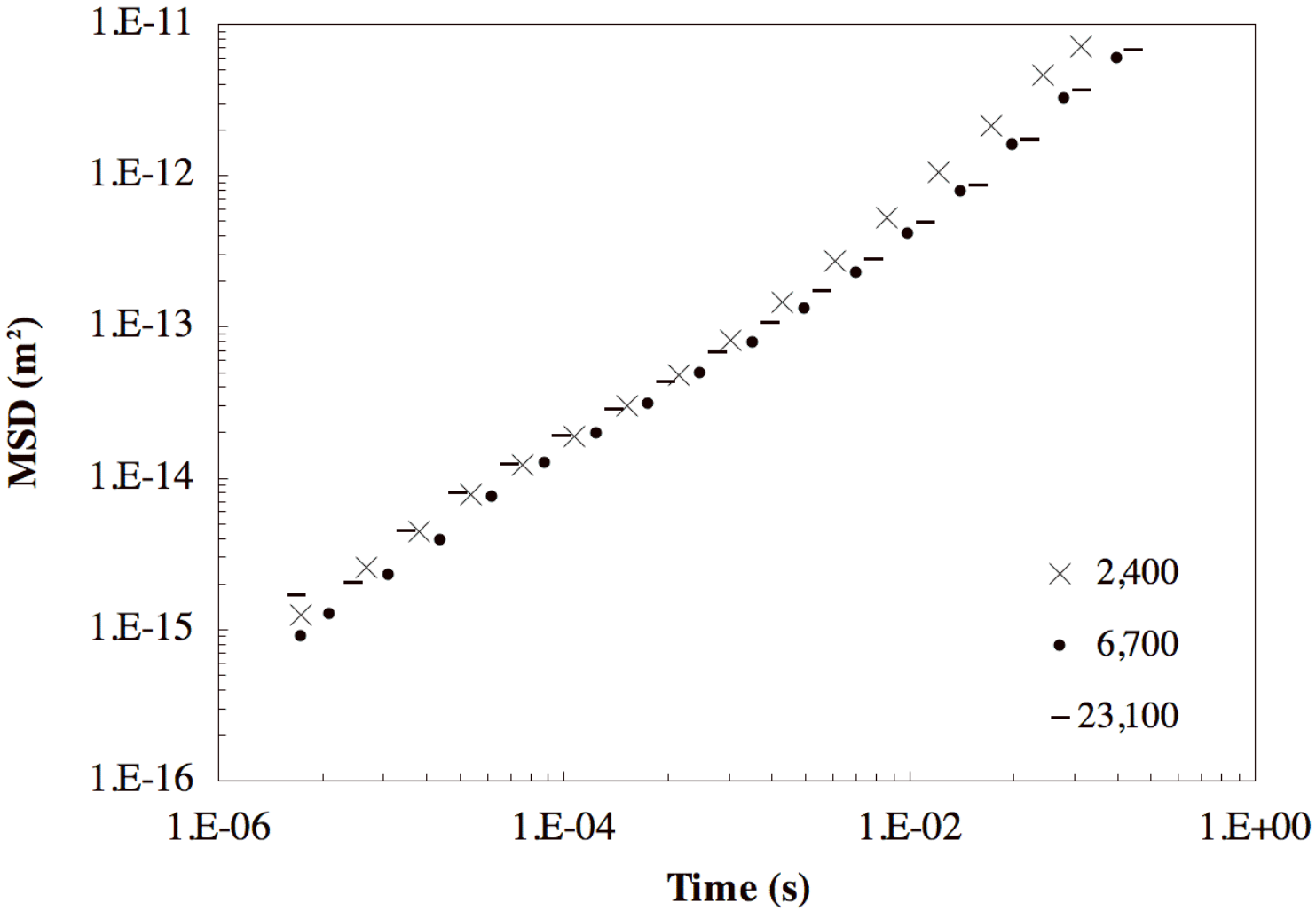

Figure 8. Experimental data for the 2,400, 6,700, and 23,100 base ss-DNA strands based on Figures 2 and 3a from Shusterman et al. (2004). Adapted and reprinted with permission from Shusterman et al. (2004). Copyrighted by the American Physical Society.

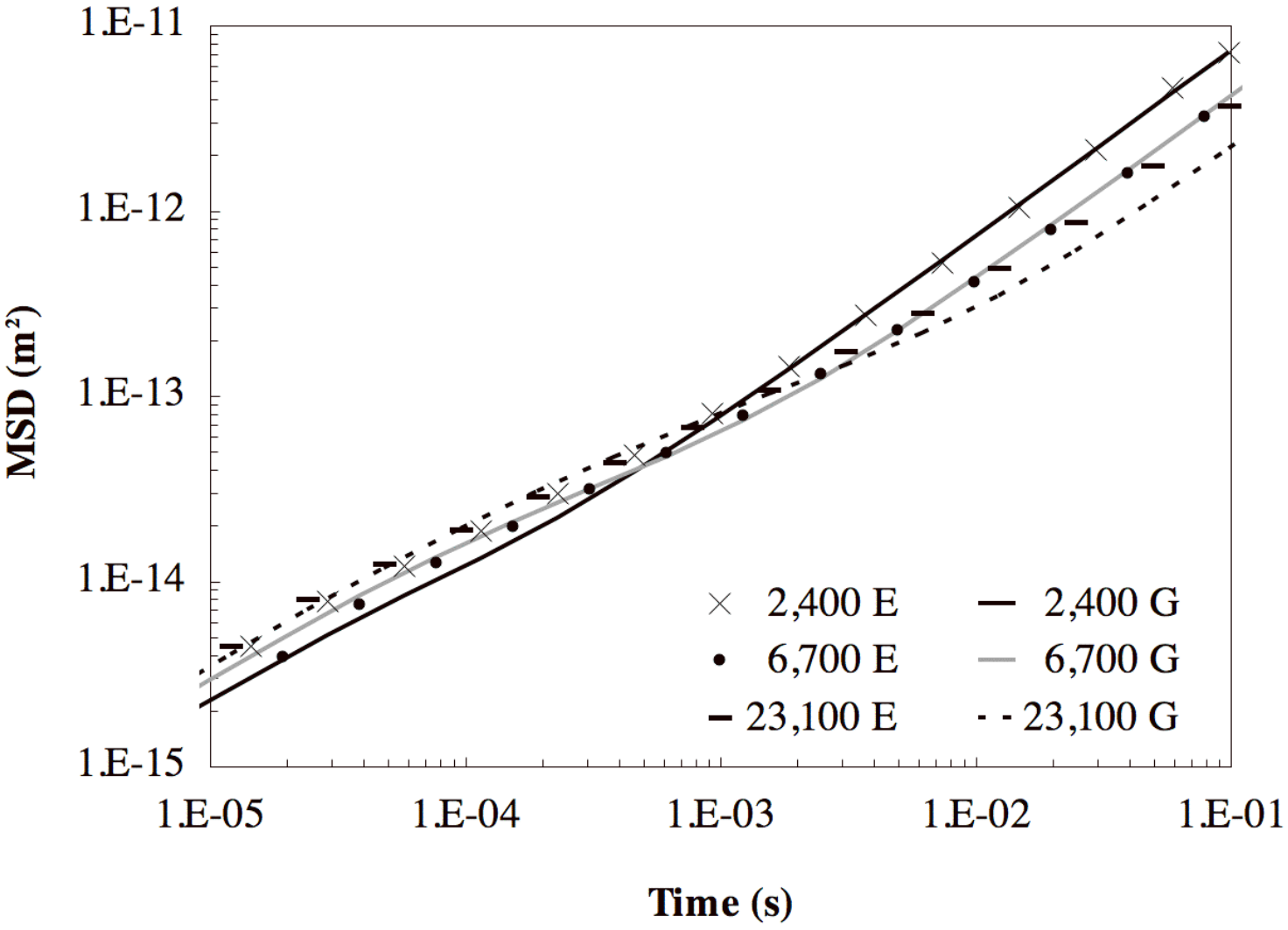

Figure 9. Comparison of experimental (E) and global (G) best-fit predictions for all three ss-DNA strands using $h^* = 0.14$ and $b = 4.94 \times 10^{-8}$ m and $N_S = 6$, 17, and 58 with error = 1.764, 1.081, and 2.166 for the 2,400, 6,700, and 23,100 base ss-DNA strands respectively.

behavior of the 23100 base ss-DNA. Thus, in the selective best-fit analysis, I ignore the 23100 base strand altogether, although, like the global best-fit, in selective best-fit, I constrain the values of h^* and b to be identical for all molecules and N_S to be proportional to number of bases.

Second, as described in Section 2.2.3, I identify the best-fit parameters based on the 2400 and 6700 ss-DNA strands alone. In this fit, the values obtained for h^* and b are 0.12 and 5.415 x 10^{-8} m respectively. Similar to the global best-fit parameters, the number of springs in this fit is scaled proportionally to the number of bases in each strand. This gives the number of springs, N_S, as 6 and 17 for the 2400 and 6700 strands, respectively, and the number of Kuhn steps per spring, $N_{K,S}$, as 12. As becomes clear from Figure 10, these parameters allow prediction of the long time behavior of the experimental data. At times less than 10^{-3} s, I note that the predictions deviate slightly from the experimental data.

The deviation might arise either because the bead-spring model is inherently unable to predict the MSD at intermediate times or because of error in the experimental data. To investigate further the ability of the bead-spring model to predict accurately trends at intermediate times, I best-fit the parameters h^*, N_S, and b to each strand individually. Figures 11 – 13 show that the individual best fits coincide with the experimental data nearly perfectly in each case.

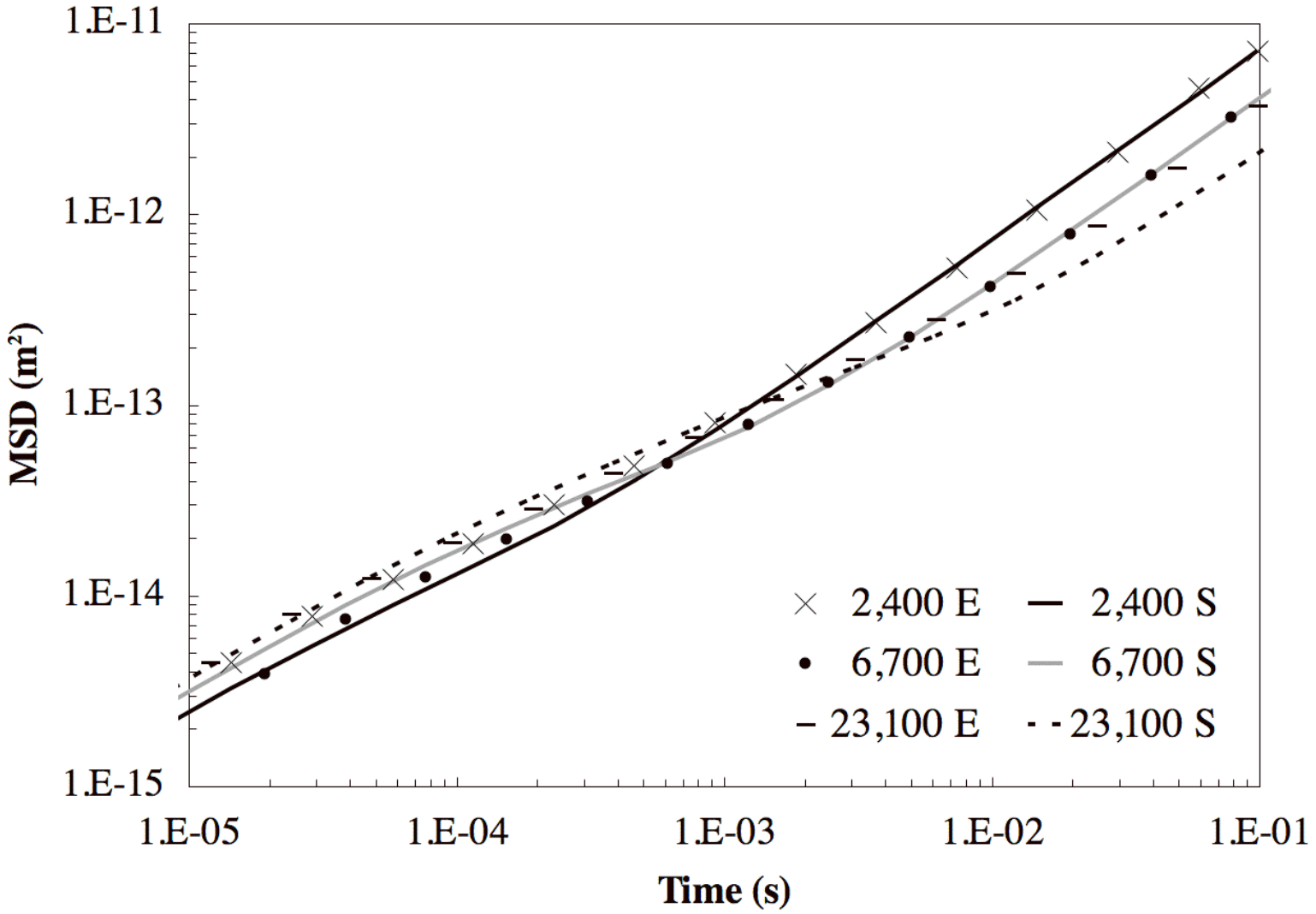

Figure 10. Comparison of the experimental observations (E) to selective best-fit (S) predictions for all three ss-DNA strands. Selective best-fit parameters are: $h^* = 0.12$, $b = 5.415 \times 10^{-8}$ m, and $N_S = 6$, 17, and 58 are computed by using only experimental data from the 2,400 and 6,700 base strands. Error is 1.530, 1.334, and 2.347 for the 2,400, 6,700, and 23,100 base strands respectively.

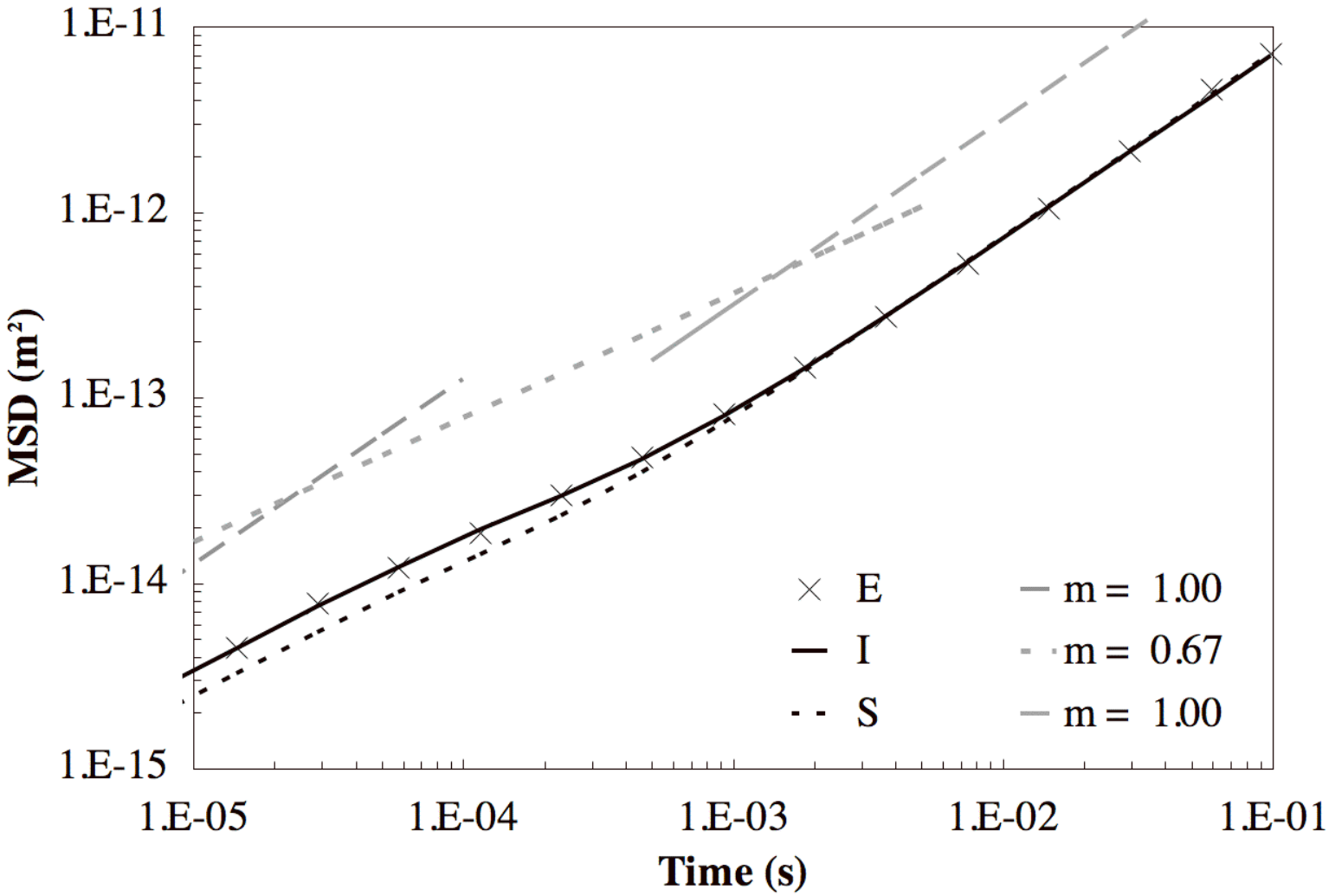

Figure 11. Comparison of experimental (E), individual best-fit (I), and selective best-fit (S) predictions for the 2,400 base strand. Individual best-fit parameters for the 2,400 base ss-DNA strand are: $h^* = 0.14$, $b = 7.125 \times 10^{-8}$ m, and $N_S = 6$ with the error = 0.453. Lines with $m = 0.67$ and $m = 1$ are shown for reference.

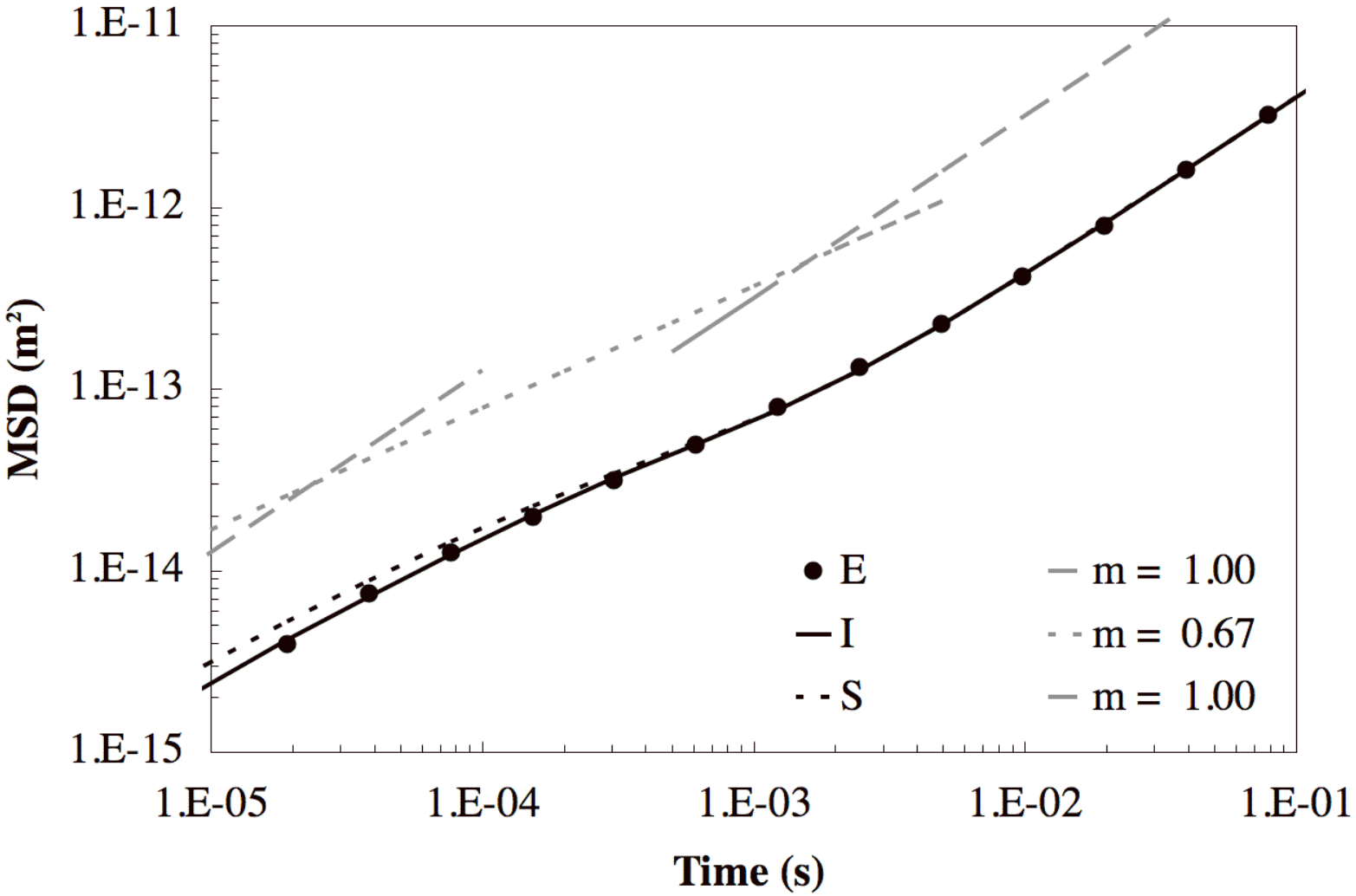

Figure 12. Same as Figure 11 except for 6,700 bases. Individual best-fit parameters for the 6,700 base ss-DNA strand are: $h^* = 0.11$, $b = 8.170 \times 10^{-8}$ m, and $N_S = 9$ with the error = 0.608.

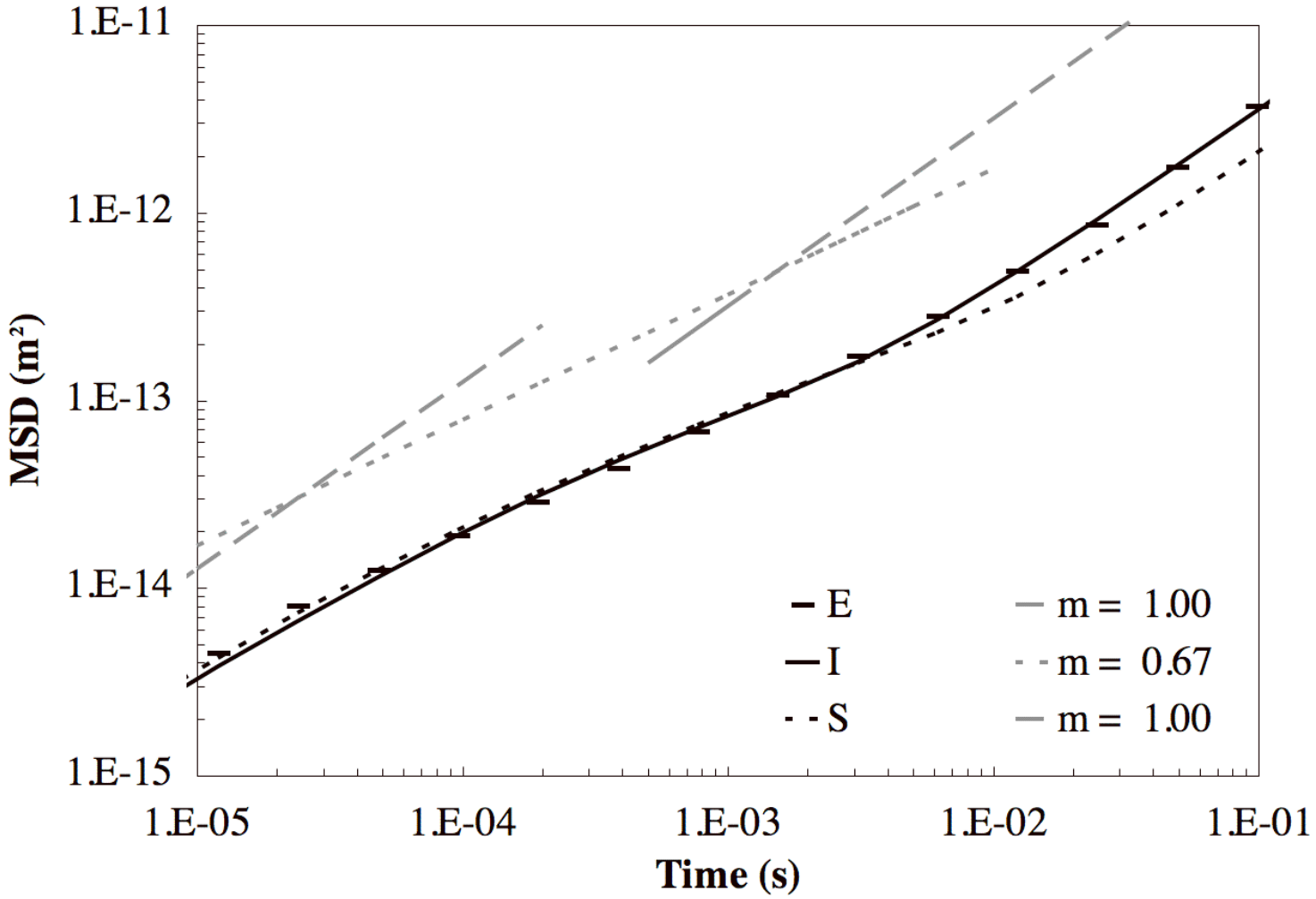

Figure 13. Same as Figure 11 except for 23,100 bases. Individual best-fit parameters for the 23,100 base ss-DNA strand are: $h^* = 0.12$, $b = 8.4550 \times 10^{-8}$ m, and $N_S = 14$ with the error = 0.906.

2.3.2. Hydrodynamic interaction behavior

Having demonstrated that the bead-spring model can, within the limits discussed above, predict ss-DNA behavior, in this section I examine whether the ss-DNA parameters are similar to those expected for synthetic polymers. I do so in two steps:

First, I compute the slopes of the MSD curves. I begin by dividing the time domain into three parts: short (time < ~10^{-4} s), intermediate (time ~ 10^{-4} - 10^{-2} s), and long (time > ~10^{-2} s). At the smallest times, the individual beads are relatively unaffected by the motion of the coil. This produces a power-law slope of unity in the log-log plot of mean square displacement versus time. At intermediate times I expect the chain to exhibit the influence of hydrodynamic interaction. Consequently, according to Zimm theory for a theta solvent at infinite dilution, the slope should be 2/3. At long times, with the coil expected to diffuse as a whole, the power-law slope should be unity again. These short-, intermediate-, and long-time behaviors are shown by lines of slopes m = 1, 2/3, and 1 on Figures 11 – 13. Shusterman et al. (2004) [14] reported slopes of 0.69 and 1 at intermediate and long times. For short times, because of scatter in the experimental data, they did not report any slope. My observations compare well with the experimentally observed slopes and are additionally able to predict the behavior at short times within the experimental error.

Second, at intermediate times, for the MSD power-law slope of 2/3 to be in accordance with Zimm theory for a modest number of beads, h^* should theoretically be 0.25 under theta conditions. However, viscoelastic predictions for polystyrene can be predicted very well with h^* as 0.15 [6]. My analysis, using global best-fit parameters, selective best-fit parameters, and individual best-fit parameters gives h^* that varies

between 0.11 and 0.14 indicating that hydrodynamic interaction in ss-DNA is similar to that in polystyrene.

2.3.3. Solvent condition

Since $h^* = 0.15$ is likely to indicate a good—rather than a theta—solvent condition, I carry out supplemental analysis to check the preliminary indication. I do so in two steps:

First, I plot the long-time diffusion coefficient against the molecular weight of the chains in Figure 14 and carry out a best-fit analysis. The molecular weight of each ss-DNA base is taken as 330 Daltons. If I consider all three strands, I obtain a slope of -0.45 and when I drop the suspect 23100 base strand chain, I get a slope of -0.56. For theta conditions, I expect a slope of -0.5 [30] which has been observed in measurements of ss-DNA center-of-mass diffusion [37]. If the system exhibited good-solvent behavior, a slope of -0.6 would be expected.

Second, since the present slope of diffusion coefficient versus number of bases for the 2400 and 6700 base strands does not give a very decisive answer, I check the 'universal ratios' [28]. While these scaling laws are strictly valid at high molecular weights, since experimental data has been shown to follow the theta-condition scaling for as low as 300 base ss-DNA strand [37], I believe this analysis can be carried out under the present conditions as well. One such 'universal ratio', the ratio of the radius of gyration, R_g, to the hydrodynamic radius, R_H, represents U_{RD} [28]:

$$U_{RD} = \frac{R_g}{R_H} = \frac{6\pi\eta_S D_G R_g}{k_B T} \tag{18}$$

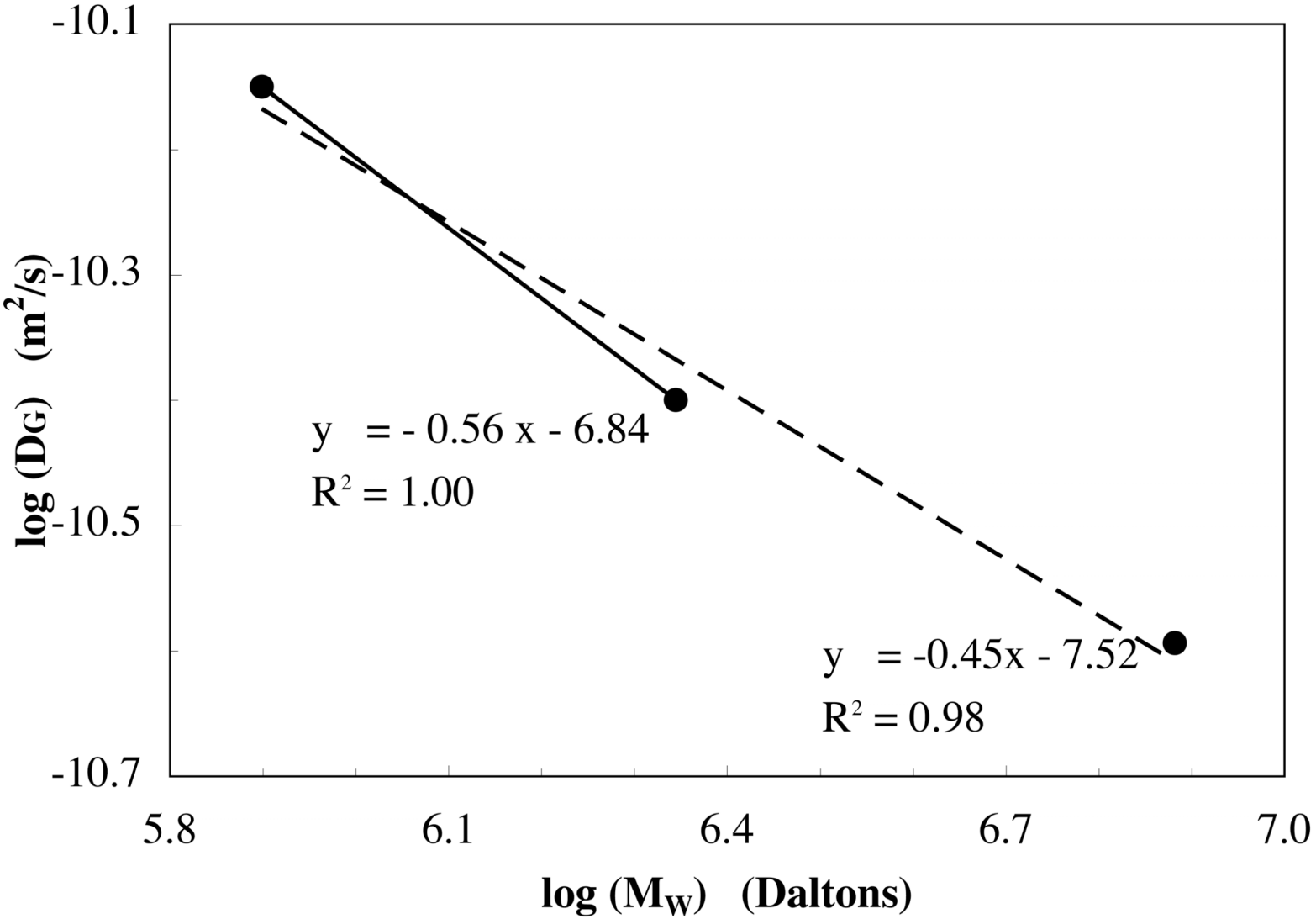

Figure 14. Log of the diffusion coefficient, D_G, plotted against log of the molecular weight, M_W, of the ss-DNA strand. Diffusion coefficient is extracted from the experimental data. The dashed line represents the linear best-fit using data from all three strands and the solid line represents the linear best-fit using only the 2,400 and 6,700 base strands.

where, assuming a random walk polymer and a freely jointed polymer, R_g and $\langle R^2 \rangle_0$ can be defined as [28]:

$$R_g = \sqrt{\frac{\langle R^2 \rangle_0}{6}} \tag{19}$$

$$\langle R^2 \rangle_0 = N_K b_K^2 \tag{20}$$

Another such parameter, $U_{\eta\tau}$, is defined as [28]:

$$U_{\eta\tau} = \frac{\sum_{i=1}^{N_S} \tau_i}{\tau_1} \tag{21}$$

For theta and good solvent conditions, U_{RD} is expected to be 1.33 and 1.56 respectively for asymptotically long chains [28]. Using the global best-fit, selective best-fit, and individual best-fit parameters, I summarize the U_{RD} values in Table 1. Since all these values are greater than 1.56, the computed U_{RD} values in Figure 15 indicate that the asymptotically large chain condition (i.e., large N_S conditions for bead-spring chains) is not reached. Since $R_g \propto \sqrt{N_K}$ and, at very large N_K, I expect $D_G \propto 1/\sqrt{N_K}$ [30], so that U_{RD} is expected to be independent of N_K. In Figure 16 I show U_{RD} computed using $R_g = b\sqrt{N_S/6}$ and D_G from equation 7. I note that while U_{RD} decreases as N_S rises and therefore chain length increases, even for N_S = 500 and therefore ss-DNA with 200,000 bases (assuming 400 bases/spring based on selective best-fit parameters fitting), the asymptote is not reached. Similarly, $U_{\eta\tau}$ is expected to be 1.645 for theta conditions and 2.39 for dominant HI without excluded volume effect [28]. My values for $U_{\eta\tau}$—summarized in Table 1—show the parameters consistent with solvent conditions to be between theta and good.

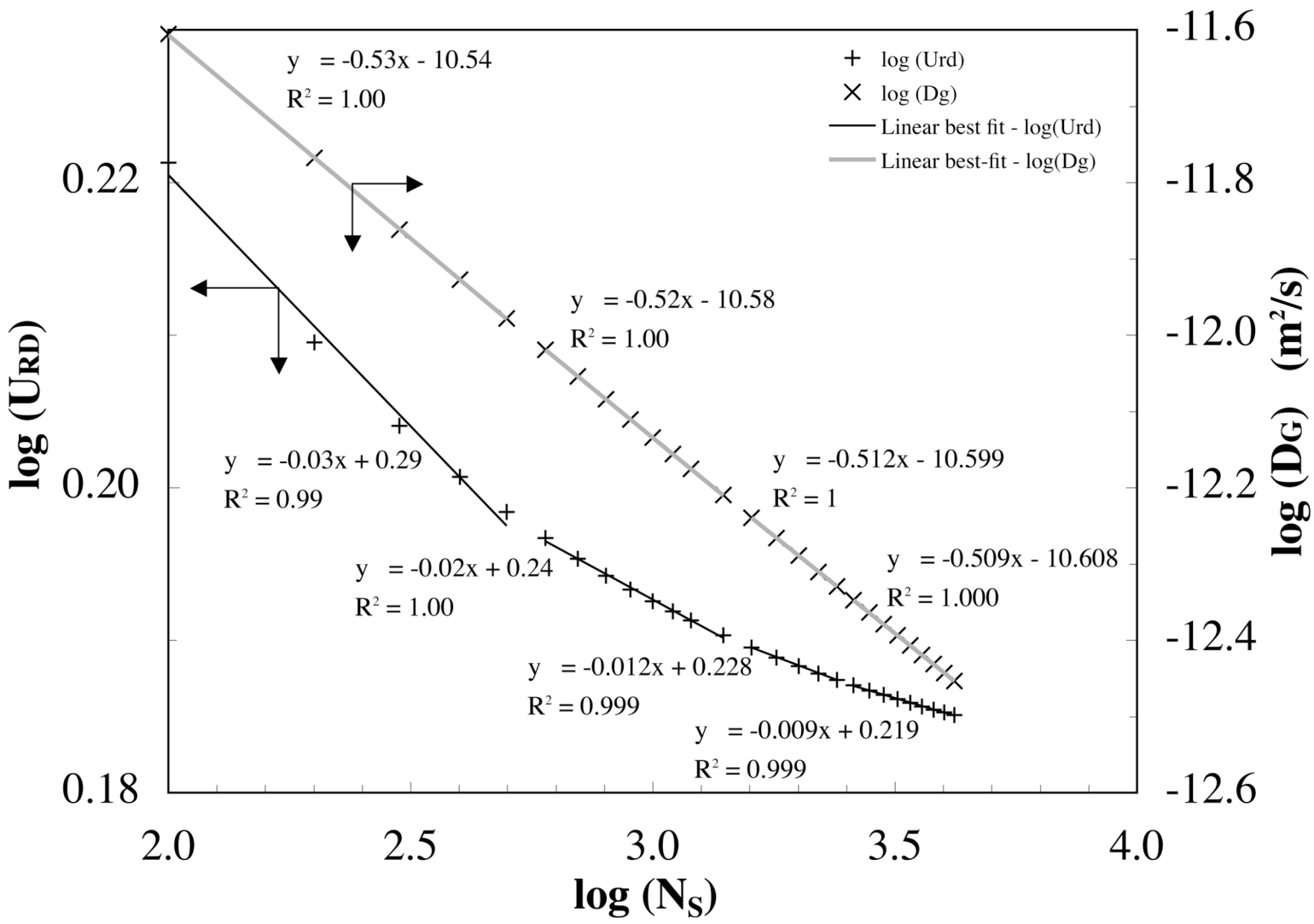

Figure 15. Log of the diffusion coefficient, D_G, and universal ratio, U_{RD}, against log of the number of springs, N_S, showing the exponent approaching the asymptotic values of -0.5 and 0 as the number of springs increase.

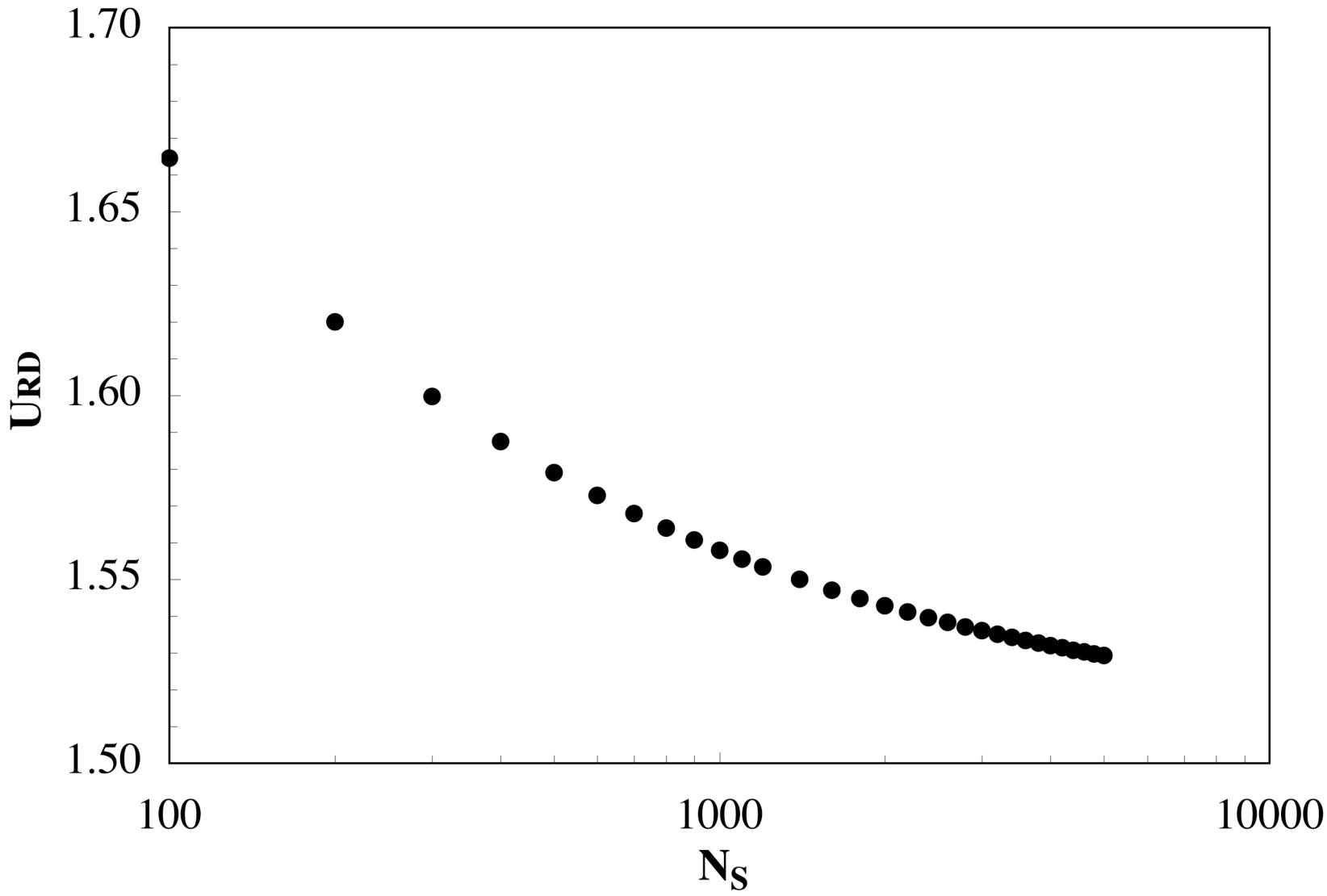

Figure 16. Universal ratio, U_{RD}, against the number of springs, N_S, showing universal ratio, U_{RD}, is reaching a plateau between the asymptotic values of 1.33 and 1.56 for theta and good solvent conditions for asymptotically long chains.

Table 1. Universal ratios, $U_{RD,}$ and $U_{\eta\tau}$, computed using the global best-fit (G), selective best-fit (S), and individual best-fit (I) parameters for the 2400, 6700, and 23100 base strands.

Condition	**Strand**	N_K	b_K (m)	R_g (m)	D_G (m^2/s)	U_{RD}	$U_{\eta\tau}$
Global	2400	89	1.284E-08	4.940E-08	1.216E-11	1.82	1.72
Global	6700	244	1.304E-08	8.315E-08	6.892E-12	1.74	1.88
Global	23100	851	1.290E-08	1.536E-07	3.532E-12	1.65	2.00
Selective	2400	74	1.543E-08	5.415E-08	1.210E-11	1.99	1.70
Selective	6700	203	1.566E-08	9.115E-08	6.680E-12	1.85	1.84
Selective	23100	708	1.550E-08	1.684E-07	3.342E-12	1.71	1.95
Individual	2400	43	2.672E-08	7.125E-08	8.428E-12	1.82	1.72
Individual	6700	169	1.888E-08	1.001E-07	6.672E-12	2.03	1.75
Individual	23100	1203	9.121E-09	1.292E-07	1.723E-12	0.68	1.82

2.3.4. Interpretation of spring length and number of springs

After demonstrating similarities between the hydrodynamic interaction for ss-DNA and polystyrene, I examine the significance of the spring length and the number of springs estimated from the fits of the model to ss-DNA data. These two parameters, taken together, largely control the coil size. In turn, the coil size affects the diffusion of the whole coil at large times.

The spring length in the bead-spring model represents the equilibrated end-to-end length of a chain segment, $\sqrt{\langle R^2 \rangle_0 / N_S}$. Each spring, in turn, can be expressed in terms of the number of Kuhn steps per spring and Kuhn length as $b = \sqrt{\langle R^2 \rangle_0 / N_S} = b_K \sqrt{N_{K,S}}$. The fully extended length of the polymer chain, L, can be expressed in terms of the number of springs, the number of Kuhn steps per spring, and Kuhn length as $L = b_K N_{K,S} N_S$. With the Kuhn length unknown, I can use the expression for the overall chain length in terms of the number of bases, n, and the length of each base, l, to obtain $L = n\ l = N_S\ N_{K,S}\ b_K$. For ss-DNA, l is known to be 4.75 x 10^{-10} m [38]. With b and N_S obtained from parameter optimization, I can derive an expression for the number of Kuhn steps per spring as $N_{K,S} = nl/b_K N_S$ and the Kuhn length as $b_K = N_S b^2 / nl$. Estimations of $N_{K,S}$ and b_K based on the different parameter fits are shown in Table 2. In order to get a representative value of the Kuhn length for the globally optimized parameters, I average the values shown in Table 1 to get b_K (global best-fit) = 1.293 x 10^{-8} m. A similar calculation for the selective best-fit parameters gives us b_K (selective best-fit) = 1.553 x 10^{-8} m. The persistence length, λ_P, corresponding to each of these two conditions is 6.465 x 10^{-9} m (global best-fit) and 7.765 x 10^{-9} m (selective best-fit)—not too far from the persistence

Table 2. Global best-fit (G), selective best-fit (S), and individual best-fit (I) parameters for three different ss-DNA strands: n = 2400, 6700, and 23100 bases with error associated with each optimization. Global best-fit (G) involves parameters optimized using all three strands, Selective best-fit (S) involves parameters optimized using 2400 and 6700 ss-DNA, and Individual best-fit (I) involves parameters optimized for each individual strand. Assuming the length of each base, l, is 4.75 x 10^{-10} m (Bockelmann et. al., 1998) and using the optimized parameters, I calculate the number of Kuhn steps per spring $N_{K,S}$, the total number of Kuhn steps, N_K, and the Kuhn length, b_K.

S. No.	Graph	Strands	Bases	Optimized			Calculated		Error	
			n	b (m)	N_S	h*	$N_{K,S}$	b_K (m)	I	G
1.	G	All	2400	4.940 x 10^{-8}	6	0.14	15	1.284 x 10^{-8}	1.764	1.729
2.	G	All	6700	4.940 x 10^{-8}	17	0.14	14	1.304 x 10^{-8}	1.081	1.729
3.	G	All	23100	4.940 x 10^{-8}	58	0.14	15	1.290 x 10^{-8}	2.166	1.729
1.	S	2400, 6700	2400	5.415 x 10^{-8}	6	0.12	12	1.543 x 10^{-8}	1.530	1.435
2.	S	2400, 6700	6700	5.415 x 10^{-8}	17	0.12	12	1.566 x 10^{-8}	1.334	1.435
3.	S	2400, 6700	23100	5.415 x 10^{-8}	58	0.12	12	1.550 x 10^{-8}	2.347	-
1.	I	2400	2400	7.125 x 10^{-8}	6	0.14	7	2.672 x 10^{-8}	0.453	
2.	I	6700	6700	8.170 x 10^{-8}	9	0.11	19	1.888 x 10^{-8}	0.608	
3.	I	23100	23100	8.455 x 10^{-8}	14	0.12	86	9.121 x 10^{-9}	0.906	

length measured as ~4 x 10^{-9} m using a 10^{-2} M Tris borate EDTA buffer [37]. The values of b_K and $R_g = N_K\sqrt{N_K/6}$ are tabulated in Table 2, along with the value of the long-time diffusion coefficient, D_G, from the experimental data. From these values, the value of the 'universal ratio' $U_{RD} = 6\pi\eta_S D_G R_g / k_B T$ is obtained and given in Table 1. These values are well above the asymptotic Zimm value of 1.479, which my simulations show in Figure 16 is are not yet reached even for the number of springs, N_S, as large as 500.

The ratio of the Kuhn length to the length of a backbone bond gives an estimate of the characteristic ratio, C_∞ [24]. Since each ss-DNA base contains four backbone bonds [39], therefore, I can take the averaged length of a backbone bond to be ~4.75 x 10^{-10} / 4 = 1.19 x 10^{-10} m. Using this information, C_∞ (global best-fit) = 109 and C_∞ (selective best-fit) = 131. While these values are large compared to C_∞ values of 10 or less for flexible uncharged synthetic polymers, ss-DNA is a polyelectrolyte whose Kuhn length for ss-DNA varies widely depending on the salt concentration. Additionally, large C_∞ values indicate swollen coils which is consistent with the rheological analysis.

The number of Kuhn steps per spring is computed to be $N_{K,S}$ (global best-fit) = 15 and $N_{K,S}$ (selective best-fit) = 12. Polystyrene has been successfully modeled with a spring corresponding to 5000 Daltons [6] with each Kuhn length corresponding to 742 Daltons [17] resulting in $N_{K,S} \sim 7$. Thus, my calculations for Kuhn steps per spring for ss-DNA are close to the value obtained for polystyrene.

A small number of springs for the global best-fit and selective best-fit parameters—even for strands with thousands of bases—indicates that there are relatively few relaxation modes present in ss-DNA. This observation is similar to what has been found for dilute polystyrene solutions [6].

Finally, I note that the experimental data for both the 2400 and 6700 base strands are very close to each other at intermediate times, and not in perfect agreement with the bead-spring model predictions. At short times, scatter in experimental data is clearly evident. This indicates the difficulty in obtaining high-precision experimental measurements at such short times and is perhaps one reason for the deviation between bead-spring model predictions and experimental observations.

Chapter 3

High frequency viscoelasticity

3.1. Microscopic polymer model

In order to study the local bond relaxation, I model the polymer chain as a series of beads connected by stiff springs. If the position vector of the i^{th} bead is denoted by $\underline{r}^i$, then the bond vector, $\underline{R}_S^i$, connecting the i^{th} and $(i+1)^{th}$ beads is:

$$\underline{R}_S^i = \underline{r}^{i+1} - \underline{r}^i \tag{22}$$

with the instantaneous bond length

$$\ell^i = \left|\underline{R}_S^i\right| = \sqrt{\sum_{k=1}^{3}\left(r_k^{i+1} - r_k^i\right)^2} \tag{23}$$

and

$$\underline{u}^i = \frac{\underline{R}_S^i}{\ell^i} \tag{24}$$

The i^{th} bending angle formed made by the two adjacent bonds defined by beads i, $i+1$, and $i+2$ can be estimated by taking the vector products of the bonds connecting the beads:

$$\cos\theta_i = \frac{\left(\underline{r}^{i+2} - \underline{r}^{i+1}\right) \bullet \left(\underline{r}^i - \underline{r}^{i+1}\right)}{\ell^{i+1}\ \ell^i} \tag{25}$$

The torsional angle, ϕ, formed by the two next-nearest neighbor bonds defined by the four adjacent beads i, j, k, and l is computed using [40]:

$$\phi = sign(\phi)\cos^{-1}(\underline{m} \bullet \underline{n}) \tag{26}$$

where

$$\underline{m} = \frac{\underline{r}^{ij} \times \underline{r}^{kj}}{\left|\underline{r}^{ij}\right| \left|\underline{r}^{kj}\right|} \tag{27}$$

$$\underline{n} = \frac{\underline{r}^{kj} \times \underline{r}^{kl}}{\left|\underline{r}^{kj}\right| \left|\underline{r}^{kl}\right|} \tag{28}$$

$$sign(\phi) = sign \;\; of \;\; \left[\underline{r}^{ij} \bullet \left(\underline{r}^{kj} \times \underline{r}^{kl}\right)\right] \tag{29}$$

In the IUPAC notation [41], in the cis conformation, $\phi = 0$ and all beads lie in a single plane with beads i and l on the same side of the line that passes through beads j and k. If one looks along the line connecting bead k towards bead j, if the bond connecting beads k and l must be rotated counterclockwise about the bond connecting k and j to reach the cis conformation via the smallest rotation angle, then, the sign of ϕ is negative. This definition can be translated into notation more commonly used for polymers, where $\phi = 0$ corresponds to the trans conformation [40] using:

$$\phi(polymer) = \phi(IUPAC) \;\pm\; \pi \tag{30}$$

The notation used in computing the spring vectors, bending angles, and the IUPAC notation of computing torsional angles is illustrated in Figure 17.

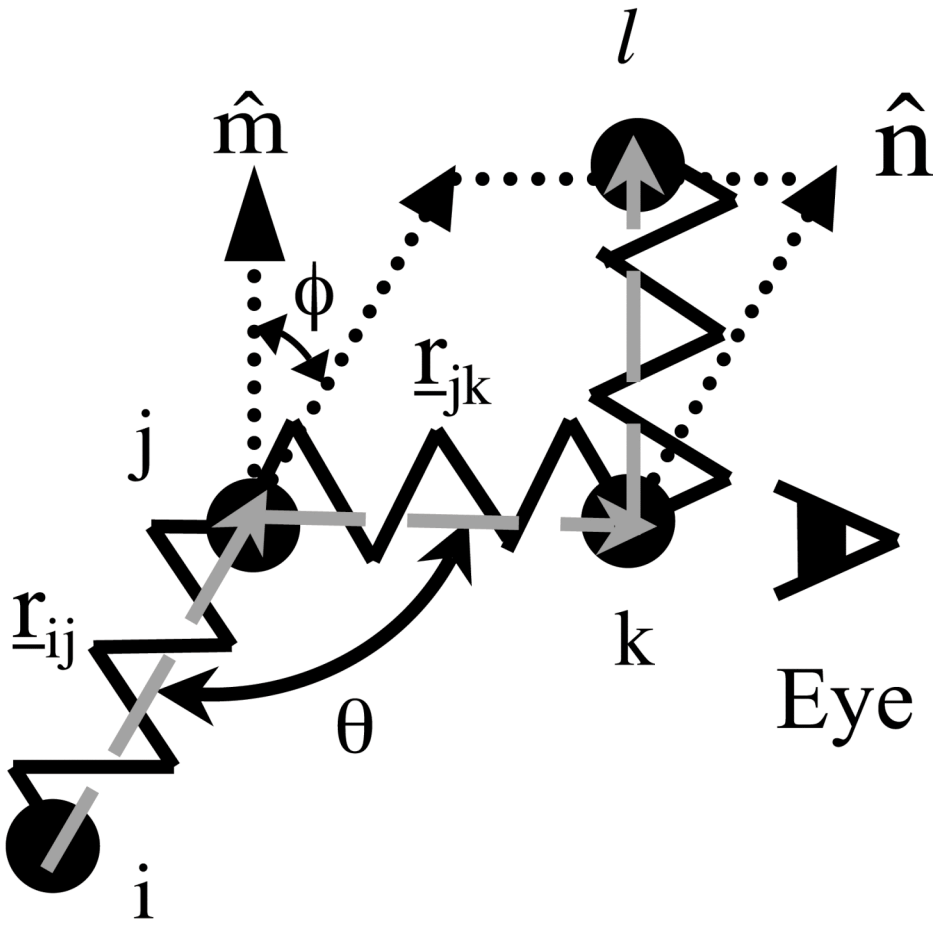

Figure 17. Illustration of beads (i, j, k, and l), spring vectors ($\underline{r}_{ij}, \underline{r}_{jk}, \underline{r}_{kl}$), bending angle, θ, and torsional angle, ϕ, all of which make up the microscopic polymer model. Adapted and reproduced with permission from Bekker et al. (1995).

3.1.1. Potential energies

Since n-Butane is the smallest chain that exhibits all bending and torsional conformations of a polymer chain, I use the Rychaert-Bellemans potential [42, 43], which was originally developed for n-Butane to describe the torsional potential energy of my model chain. The distance between adjacent C-C bonds is maintained near 1.53 $\overset{0}{\text{A}}$ by using a stiff Fraenkel stretching potential:

$$V_S^i\left(\ell^i\right) = \frac{\gamma_S}{2}\left(\ell^i - \ell_0\right)^2 \tag{31}$$

where γ_S is the stretching constant, ℓ^i is the bond length of the i^{th} bond, and ℓ_0 is the equilibrium bond length. Similarly, the angles between adjacent bonds are maintained near $109^0\,47'$ by use of the bending potential:

$$V_B^i\left(\theta_i\right) = \frac{\gamma_\theta}{2}\left(\cos\theta_i - \cos\theta_0\right)^2 \tag{32}$$

where γ_θ is the bending constant, θ_i is the angle formed by the i^{th} and $(i+1)^{th}$ bonds, and θ_0 is the equilibrium bond angle which is $109^0\,47'$. To control the bond rotation about a central bond, I use the torsional potential [42-44]:

$$V_T^i\left(\phi_i\right) = \gamma_\phi \sum_{n=0}^{5} a_n \cos^n \phi_i \tag{33}$$

where γ_ϕ is the torsional constant, ϕ_i is the torsional angle formed by the i^{th}, $(i+1)^{th}$, and $(i+2)^{th}$ bonds, and the a_n's are constants. This torsional potential yields four energy states: trans, gauche$^+$, gauche$^-$, and cis. The barrier to rotation between trans and gauche$^\pm$ states peaks at $\phi = \pm 60^0$. The potentials at various rotational angles are designated as $V_T\,(\phi = 0^0)$ for the trans state—the lowest energy state, $V_{GT}\,(\phi = \pm 60^0)$ for the local maxima between trans and gauche, $V_G\,(\phi = \pm 120^0)$ for the gauche$^\pm$ states—local energy minima, and $V_C\,(\phi$

$= \pm 180^0$) for the cis state—the maximum energy state. From the shape of the rotational potential, I can extract two additional relationships: $\partial V_T^i(\phi_i)/\partial\phi_i\big|_{\phi=\pm 60^0} = 0$ and $\partial V_T^i(\phi_i)/\partial\phi_i\big|_{\phi=\pm 120^0} = 0$. These six conditions enable me to relate the six rotational parameters to the known state potentials:

$$\left.\begin{aligned} a_0 &= \frac{V_C + 8(V_{GT} + V_G)}{18\gamma_\phi} \\ a_1 &= \frac{14\left(V_{GT} - V_G\right)}{9\gamma_\phi} - \frac{V_C}{14\gamma_\phi} \\ a_2 &= -\frac{4\left[V_C - (V_{GT} + V_G)\right]}{9\gamma_\phi} \\ a_3 &= \frac{\left[8V_C - 99\left(V_{GT} - V_G\right)\right]}{18\gamma_\phi} \\ a_4 &= -2a_2 \\ a_5 &= \frac{8\left[-V_C + \left(V_{GT} - V_G\right)\right]}{9\gamma_\phi} \end{aligned}\right\} \qquad (34)$$

In my simulations, the polymer is modeled as a phantom chain with no excluded volume interactions between atoms and with hydrodynamic interactions neglected. All friction is assumed to be concentrated at the atoms which are represented by beads that act as drag centers. Unlike Helfand et al. [44] who simulated cyclic chains (rings) to make all bonds equivalent, in my simulations of linear polymers, the ends of the polymer chain are not connected. I use Helfand et al.'s [44] stretching, γ_S/m= 2.5 x 10^{27} s^{-2}, and bending, γ_θ/m= 1.3 x 10^7 J/kg, constants, which are softened relative to physically realistic values to enable larger time steps to be taken during explicit numerical integration. The value of the torsional parameter remains unchanged at γ_ϕ/m = 6.6344 x 10^5 J/kg. All parameter values are summarized in Table 3.

Table 3. List of parameters used with the microscopic polymer model (Helfand et. al, 1980).

S. No.	Property	Symbol	Value	Unit
1.	Frictional coefficient / mass	b	10^{14}	s^{-1}
2.	Bead mass	m	0.014	kg/mol
3.	Bead frictional coefficient	ζ	1.4×10^{12}	kg/mol-s
4.	Equilibrium spring length	ℓ_0	1.53×10^{-10}	m
5.	Equilibrium bending angle	θ_0	109^0 47'	degrees
6.	Torsional angle for trans-state	ϕ_T	0^0	degrees
7.	Torsional angle for energy barrier	ϕ_{GT}	$\pm 60^0$	degrees
8.	Torsional angle for gauche-state	ϕ_G	$\pm 120^0$	degrees
9.	Torsional angle for cis-state	ϕ_C	$\pm 180^0$	degrees
10.	Stretching force coefficient / mass	γ_S/m	2.5×10^{27}	s^{-2}
11.	Bending force coefficient / mass	γ_θ/m	1.3×10^7	J/kg
12.	Rotational force coefficient / mass	γ_ϕ/m	6.634×10^5	J/kg
13.	Rotational force parameter *	a_0	1	
14.	Rotational force parameter *	a_1	1.3108	
15.	Rotational force parameter *	a_2	- 1.4135	
16.	Rotational force parameter *	a_3	- 0.3358	
17.	Rotational force parameter *	a_4	2.8271	
18.	Rotational force parameter *	a_5	- 3.3885	
19.	Temperature	T	372	K
20.	Torsional potential for trans-state	E_T	0 = 0.000 k_BT	J/mol
21.	Torsional potential for gauche-state	E_G	2,933 = 0.948 k_BT	J/mol
22.	Torsional potential for barrier	E_{GT}	12,360 = 3.996 k_BT	J/mol
23.	Torsional potential for cis-state	E_C	44,833 = 14.495 k_BT	J/mol

* Values of the rotational force parameters (a_0, a_1, …, a_5) correspond to the gauche/trans barrier height being 100% of its base value.

3.1.2. Force calculations

With the polymer chain immersed in solvent, the random motion of solvent molecules leads to Brownian forces acting on the chain, which can be represented by the form [44, 45]:

$$\underline{F}_R^i = \sqrt{\frac{6\zeta k_B T}{\Delta t}}\,\underline{u} \tag{35}$$

where ζ is the bead frictional constant, k_B is the Boltzmann constant, T is the absolute temperature, Δt is the time step, and $\underline{u}$ is a vector each component of which has a uniform random distribution between -1 and 1. The temperature is set at 372 K for all the simulations in this work.

To convert the stretching potential to a stretching force acting on the i^{th} bead, I use the gradient of the stretching potential:

$$\underline{F}_S^i = -\frac{\partial}{\partial \underline{r}^i}\sum_{p=1}^{N_S}\frac{\gamma_S}{2}\left(\ell^p - \ell_0\right)^2 \tag{36}$$

Next, I describe the derivation of the forces acting on the beads from the bending and torsional potentials. While some of the needed equations are available in literature [40, 46], I briefly summarize them below for ease of reference and consistency in notation.

The bending force is computed by taking the derivative of the bending potential with respect to the position of the bead on which the force is computed:

$$\underline{F}_B^i = -\frac{\partial V_B}{\partial \underline{r}^i} = -\frac{\partial}{\partial \underline{r}^i}\left[\sum_{p=1}^{p=N_S-1}\frac{\gamma_\theta}{2}\left(\cos\theta_p - \cos\theta_0\right)^2\right] \tag{37}$$

Since each bending angle is enclosed between two adjacent bonds, the contribution to the j^{th} component of the bending force on the i^{th} bead, r_j^i, can have up to three contributions:

$$\frac{\partial V_B}{\partial r_j^i} = \gamma_\theta \sum_{p=i-2}^{i} \left(\cos\theta_p - \cos\theta_0\right) \frac{\partial \cos\theta_p}{\partial r_j^i} \tag{38}$$

where

$$\frac{\partial \cos\theta_i}{\partial r_j^{i+2}} = -\frac{1}{\ell^{i+1}} \left[\frac{\left(r_j^{i+1} - r_j^i\right)}{\ell^i} + \frac{\left(r_j^{i+2} - r_j^{i+1}\right)}{\ell^{i+1}} \cos\theta_i \right] \tag{39}$$

$$\frac{\partial \cos\theta_i}{\partial r_j^{i}} = \frac{1}{\ell^{i}} \left[\frac{\left(r_j^{i+2} - r_j^{i+1}\right)}{\ell^{i+1}} + \frac{\left(r_j^{i+1} - r_j^{i}\right)}{\ell^{i}} \cos\theta_i \right] \tag{40}$$

$$\frac{\partial \cos\theta_i}{\partial r_j^{i+1}} = -\left[\frac{\partial \cos\theta_i}{\partial r_j^{i}} + \frac{\partial \cos\theta_i}{\partial r_j^{i+2}} \right] \tag{41}$$

For bead number 1, only $\partial\cos\theta_1 / \partial r_j^1$ is relevant. For bead number 2, $\partial\cos\theta_1 / \partial r_j^2$ and $\partial\cos\theta_2 / \partial r_j^2$ are required. For bead number N_S, $\partial\cos\theta_{N_{S-2}} / \partial r_j^{N_S}$ and $\partial\cos\theta_{N_{S-1}} / \partial r_j^{N_S}$ are needed, and finally, for bead number $N_S + 1$, only $\partial\cos\theta_{N_{S-1}} / \partial r_j^{N_{S+1}}$ needs to be computed. For all other beads, three derivatives are needed.

Similarly, the corresponding relationships for the j^{th} component of the force on the i^{th} bead from the torsional potential is:

$$\underline{F}_i^T = -\frac{\partial V_T}{\partial \underline{r}^i} = -\frac{\partial}{\partial \underline{r}^i} \left[\sum_{p=1}^{p=N_S-2} \gamma_\phi \sum_{n=0}^{5} a_n \cos^n \phi_p \right] \tag{42}$$

For a set of four beads, p, q, r, s (in order) that form a torsional angle, the derivative of the angle with respect to each bead's coordinates is as follows [40]:

$$\frac{\partial \cos\phi}{\partial r_j^p} = a_{pqr} \left(\cos\phi \frac{\partial \theta_{pqr}}{\partial r_j^r} - \frac{\partial \theta_{qrs}}{\partial r_j^q} \right) \tag{43}$$

$$\frac{\partial \cos\phi}{\partial r_j^s} = a_{srq}\left(\cos\phi \frac{\partial \theta_{qrs}}{\partial r_j^q} - \frac{\partial \theta_{pqr}}{\partial r_j^r}\right) \tag{44}$$

$$\frac{\partial \cos\phi}{\partial r_j^q} = c_{pqr} \frac{\partial \cos\phi}{\partial r_j^p} - b_{srq} \frac{\partial \cos\phi}{\partial r_j^s} \tag{45}$$

$$\frac{\partial \cos\phi}{\partial r_j^r} = c_{srq} \frac{\partial \cos\phi}{\partial r_j^s} - b_{pqr} \frac{\partial \cos\phi}{\partial r_j^p} \tag{46}$$

with

$$\frac{\partial \theta_{pqr}}{\partial r_j^r} = -\frac{1}{\sin\theta_{pqr}} \frac{\partial \cos\theta_{pqr}}{\partial r_j^r} \equiv -\frac{1}{\sin\theta_i} \frac{\partial \cos\theta_i}{\partial r_j^{i+2}} \tag{47}$$

where $a_{pqr} = r_{qr}/r_{pq}\sin\theta_{pqr}$, $b_{pqr} = r_{pq}\cos\theta_{pqr}/r_{qr}$, $c_{pqr} = b_{pqr} - 1$, and θ_{pqr} denotes the bending angle formed by beads *p*, *q*, and *r*.

Neglecting inertial forces, to conserve momentum the frictional force must be set equal to the sum of all the potential forces and the Brownian random force yielding [44]:

$$\zeta \frac{d\underline{r}^i}{dt} = \underline{F}_S^i + \underline{F}_B^i + \underline{F}_T^i + \underline{F}_R^i \tag{48}$$

3.1.3. Code validation

To validate the code, I compute the change in the total potential energy of the system over a small time step and compare it to the work done on the system in this time:

$$V_S\big|_{t+\Delta t} - V_S\big|_t = \sum_{i=1}^{i=N_S+1} \underline{F}_S^i \bullet \Delta\underline{r}^i \tag{49}$$

$$V_B\big|_{t+\Delta t} - V_B\big|_t = \sum_{i=1}^{i=N_S+1} \underline{F}_B^i \bullet \Delta\underline{r}^i \tag{50}$$

$$V_T\big|_{t+\Delta t} - V_T\big|_t = \sum_{i=1}^{i=N_S+1} \underline{F}_T^i \bullet \Delta\underline{r}^i \tag{51}$$

where Δt is the time step and Δr is the distance moved by the i^{th} bead in time Δt. That is, I use the formulas for the forces derived analytically from the potentials to evaluate the right side of each of the above equations and compare this with the change in potential over a single time step calculated directly from the expression for each potential. This procedure validates not only that the formulas for the forces are correctly derived and written into the computer code but also determines the time step that is small enough to accurately calculate the change in potential. To ensure that the model is able to replicate the system accurately, I require that the spring length and bending angle remain close to the ideal values. In order to do so, I use 'realistic' values of the parameters [44], i.e., γ_S/m = 1.8 x 10^{28} s^{-2} and γ_θ/m = 4.2 x 10^7 J/kg where I take the mass of the polymer bead, m, to be 0.014 kg/mol. Since I are using an explicit integration scheme, I am forced in the above check to use very small time steps ($\Delta t \sim 10^{-21}$ s) to keep the changes in the potential small over a single time step.

3.1.4. Time step determination

Ideally, I would like to select a value of time step that is small enough to ensure the force calculations match the change in potentials. However, to do so, I are forced to use a very small time step as noted above. Even with current computing power, simulating for as long as a nanosecond with a time step of 10^{-21} s would take an enormous amount of computational time. Since I am only concerned with tracking the relaxation of chain configurations and only need to pick a time step small enough for these properties to be accurate—even if the forces and potentials are not exact for individual atoms. Using

the time step of Δt = 5 x 10^{-15} s chosen by Helfand and coworkers [44] as an upper limit using the softened potentials, as shown in Figure 18, I find no change in autocorrelation functions from the results obtained using a much smaller value Δt = 10^{-16} s. Hence, to compute the autocorrelation functions, I use a time step of 5 x 10^{-15} s in my simulations.

3.2. Theory

3.2.1. Coil expansion

A freely jointed chain (or bead-rod) model can be used to represent the coarse-grained equilibrium distribution of configurations of a realistic chain with bending and torsional potentials if the freely jointed chain has the same mean square end-to-end distance, $\langle R^2 \rangle_0$, as the realistic chain, i.e., $\langle R^2 \rangle_0 = N_K b_K^2$ where N_K is the number of effective "Kuhn" steps and b_K is the Kuhn step length of the freely jointed chain [19, 30]. The 'characteristic ratio' of a polymer is defined as the ratio of $\langle R^2 \rangle_0$ of the actual polymer to that of an ideal chain in which each bond is freely jointed to neighboring bonds, for which $\langle R^2 \rangle_0 = N_S l_0^2$, where N_S is the number of rod-like bonds and l_0 is the average bond length [19]. Thus, the characteristic ratio can be used a measure of the coil expansion that results from the bending and torsional forces.

The contribution of the bending potential to the characteristic ratio is [25]:

$$C_\infty^B = \frac{1 + \langle \cos\theta_C \rangle}{1 - \langle \cos\theta_C \rangle} \tag{52}$$

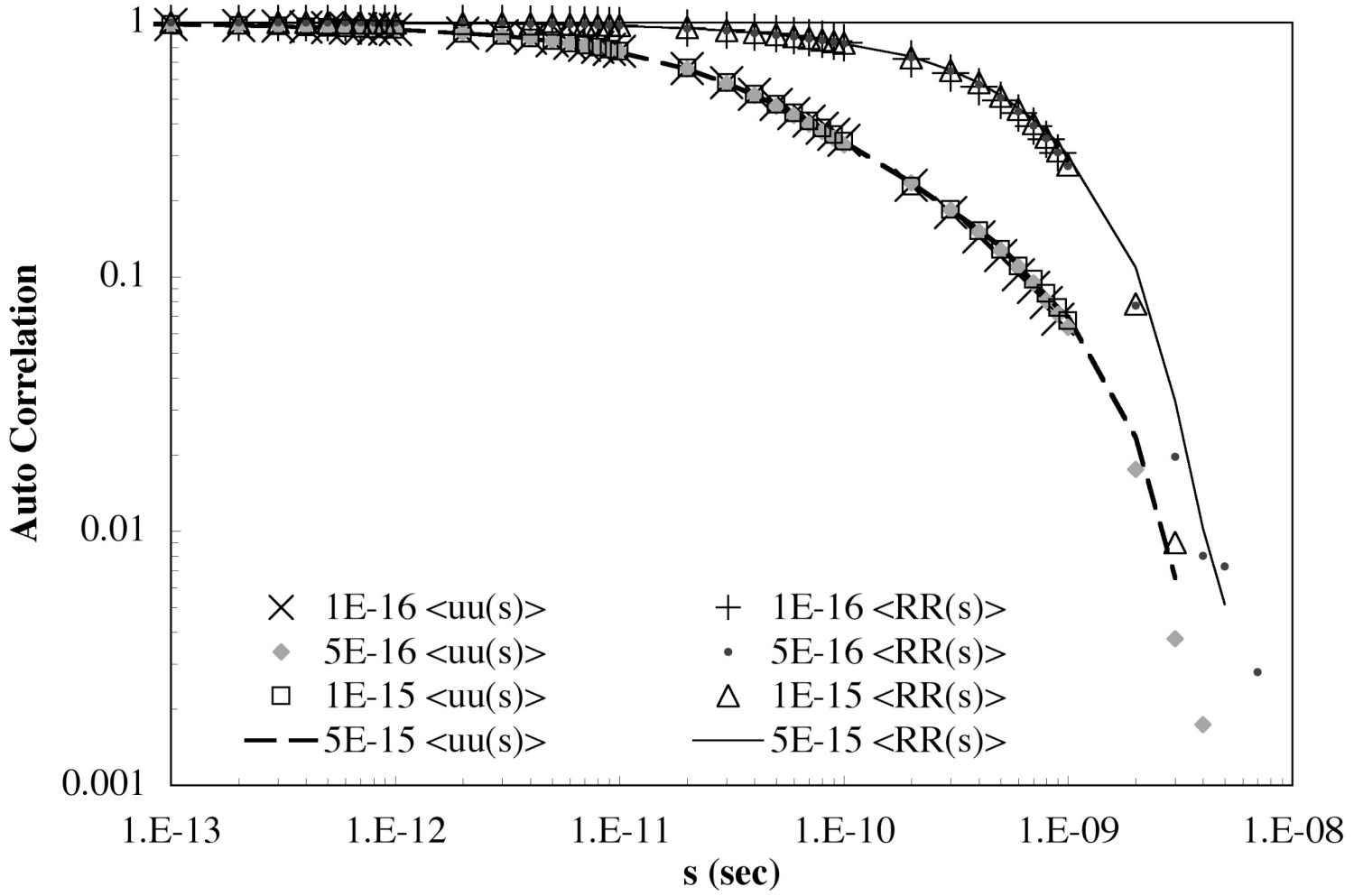

Figure 18. Determination of suitable time step for the system with $N_S = 25$. Figure shows calculation of end-to-end vector autocorrelation function, <RR(s)> and unit spring vector autocorrelation function, <uu(s)>, using time steps, Δt, of 10^{-16} s, 5 x 10^{-16} s, 10^{-15} s, and 5 x 10^{-15} s.

where $\theta_C \equiv \pi - \theta$ is the complement of the mean bending angle as defined in Section 3.1. Thus, the mean square end-to-end distance of a chain with a bending potential becomes $\langle R^2 \rangle_0 = C_\infty^B N_S l_0^2$. For tetrahedral bonding, $\langle \cos\theta_C \rangle = \cos\theta_C = 1/3$, yielding $C_\infty^B = 2$. Similarly, the contribution of the torsional force to the characteristic ratio is [25]:

$$C_\infty^T = \frac{1 + \langle \cos\phi \rangle}{1 - \langle \cos\phi \rangle} \tag{53}$$

where $\langle \cos\phi \rangle$ is the average of the cosine of the torsional angle. Thus, the mean square end-to-end distance with bending and rotational forces becomes $\langle R^2 \rangle_0 = C_\infty^T C_\infty^B N_S l_0^2$.

3.2.2. Probability distribution functions

While the ideal length between two carbon bonds is 1.53 $\overset{0}{\text{A}}$, if I use a realistic spring constant to keep the length fixed, the time step would have to be exceedingly small. As is clear from the distribution shown in Figure 19, using a spring constant softened by a factor of 10, the bond length, l, is still within $\pm$10% of the ideal length, l_0, about 80% of the time and is within $\pm$20% of the ideal length almost 100% of the time.

Similarly, even with my bending potential's coefficient, γ_θ / m, reduced to one-fourth of its realistic value, Figure 20 shows the bending angles being within $\pm 10^0$ of their ideal value at 109^0 47' about 70% of the time and within $\pm 20^0$ of the ideal value almost 100% of the time. This distribution is created with simulations carried out using a 40-spring chain for 10^9 time steps and data being recorded at 30,000 equally spaced points in time.

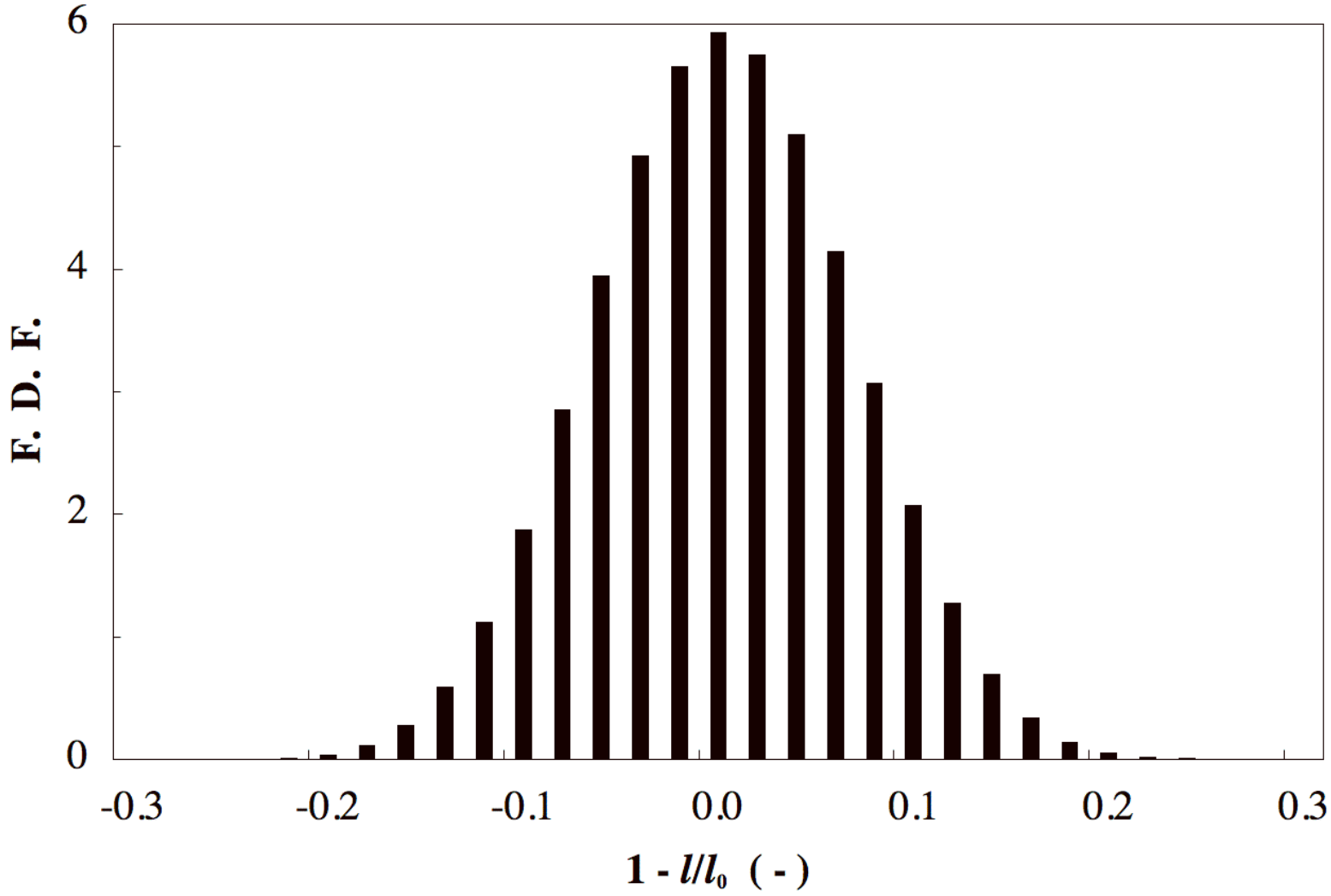

Figure 19. Frequency distribution function (F. D. F.) of the spring length as a fractional deviation from the ideal length obtained through simulation using 40 Fraenkel springs.

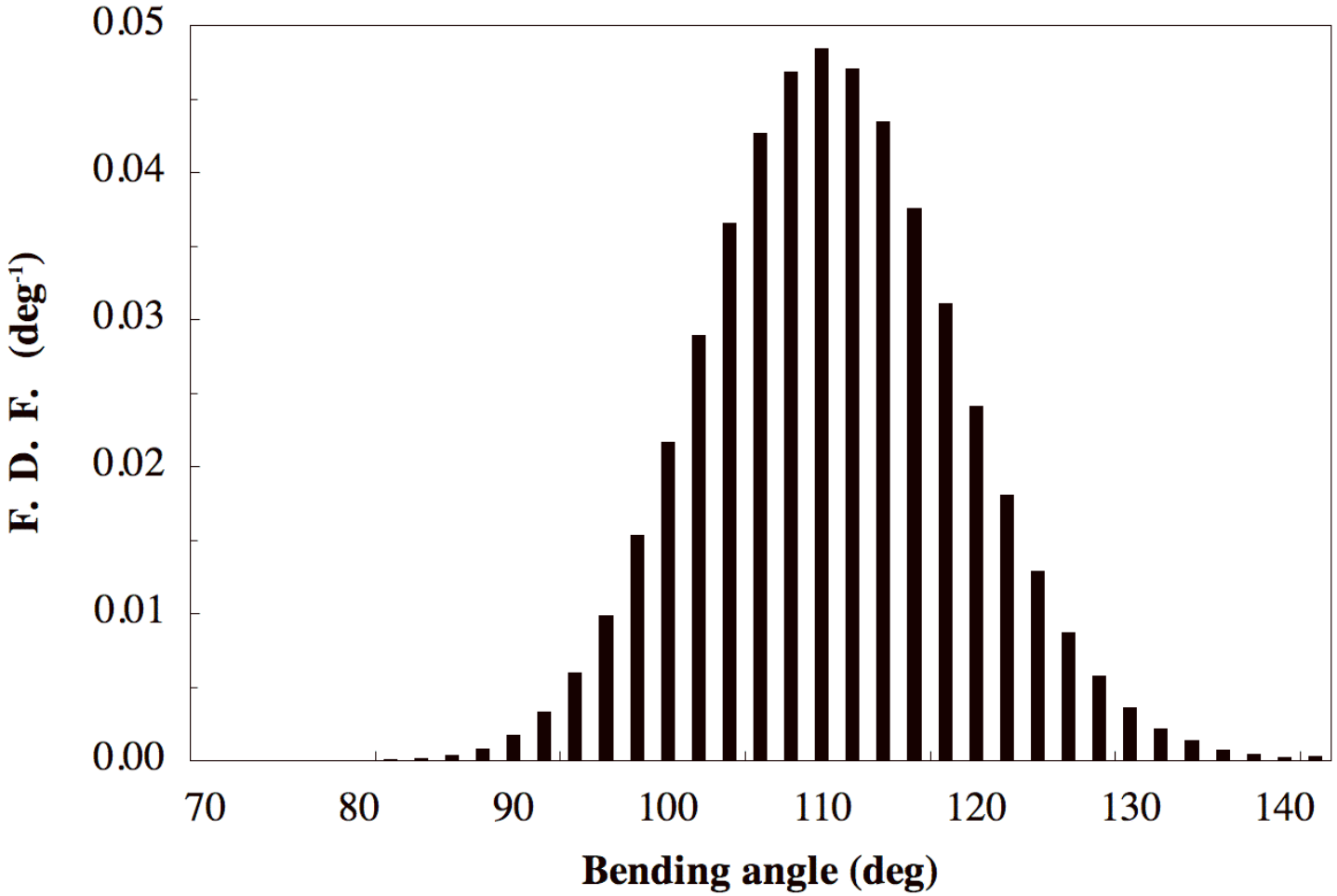

Figure 20. Frequency distribution function (F. D. F.) of the bending angle as a fractional deviation from the ideal bending angle obtained through simulation using 40 Fraenkel springs.

The theoretical probability distribution for the torsional angle can be computed from the Boltzmann distribution as:

$$p(\phi) = \frac{\exp\left(-\frac{V(\phi)}{RT}\right)}{\int_{\phi=-\pi}^{\phi=\pi} \exp\left(-\frac{V(\phi)}{RT}\right) d\phi} \tag{54}$$

where $V(\phi)$ is the torsional potential function. Figure 21 compares the theoretical torsional angle probability distributions for the barrier heights V_{GT} = 0, 12.36, and 24.72 kJ/mol for N_S = 40. Since the barrier height for butane is 12.36 kJ/mol [42-44], these values correspond to 0%, 100%, and 200% of the "base" barrier height for butane. The corresponding characteristic ratios are $C_\infty^T = 2.9355$, $C_\infty^T = 2.4101$, and $C_\infty^T = 2.1461$ when the barrier heights are 0%, 100%, and 200% of the "base" height. The probability of finding an angle in each of the energy states gauche$^-$, trans, and gauche$^+$ can be defined as: $p_{G^-} = \int_{\phi=-\pi}^{\phi=-\pi/3} p(\phi) d\phi$, $p_T = \int_{\phi=-\pi/3}^{\phi=\pi/3} p(\phi) d\phi$, and $p_{G^+} = \int_{\phi=\pi/3}^{\phi=\pi} p(\phi) d\phi$. My simulations of a linear chain with N_S = 25 yields p_T = 0.601, which is within 1% of the reported value [44], showing that my simulation exhibits correct statistical behavior.

3.3. Results

The results presented in this section are obtained from simulations that are run for 10^{10} time steps with bead coordinates recorded 100% of the time for the first 10^4 steps, 10% of the time at regular intervals for time steps between 10^4 – 10^5, 1% of the time for time steps between 10^5 – 10^6 and so on, to conserve data storage while covering a very large dynamic range. The bead coordinates are then used to compute autocorrelation

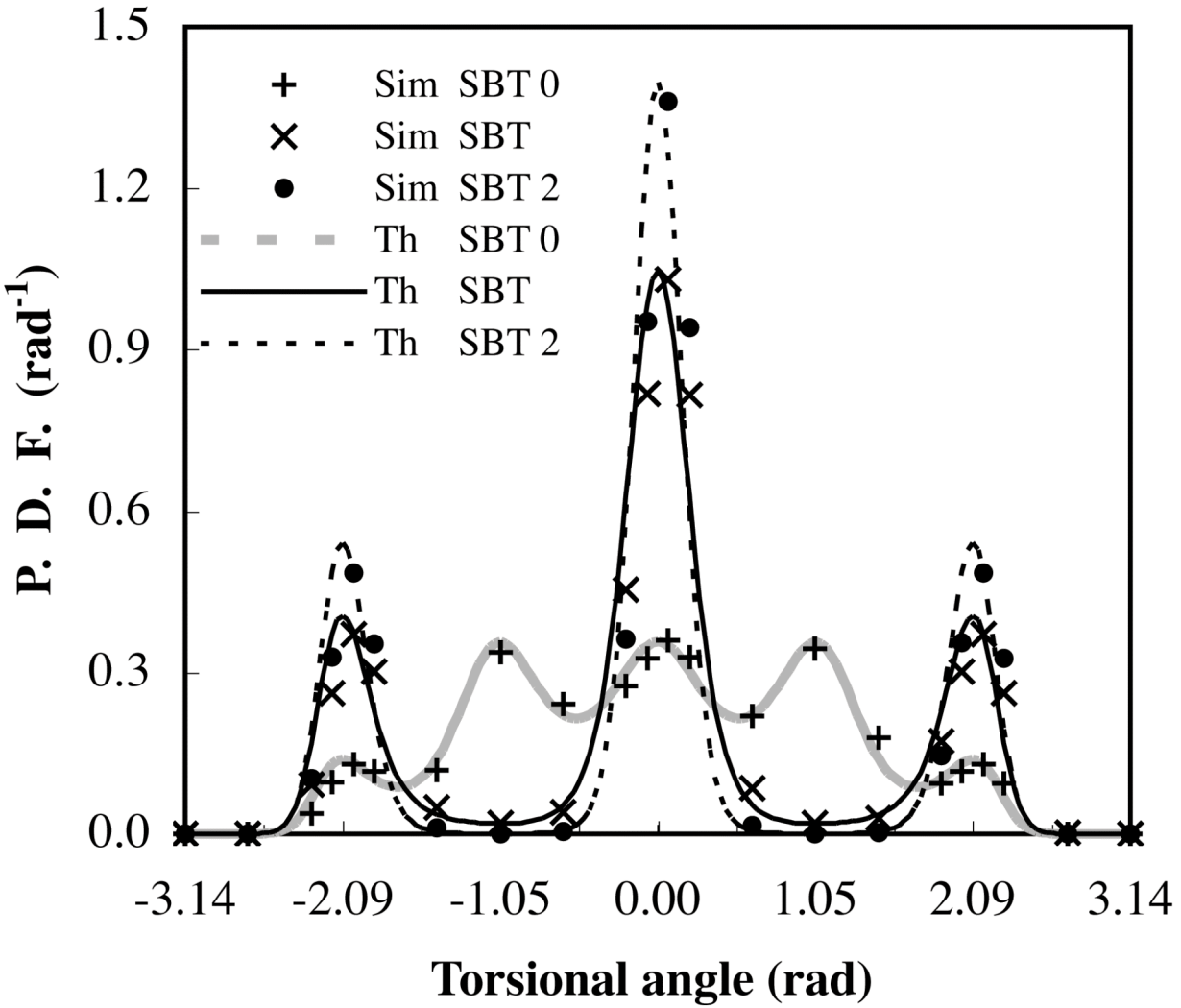

Figure 21. Theoretical (Th) and simulated (Sim) probability distribution function (P. D. F.) of the torsional angle for the trans-gauche barrier heights being 0%, 100%, and 200% of the base value. Each distribution is obtained from a simulation with $N_S = 40$ generating 30,000 points equally spaced in time.

functions.

In order to study the behavior of the coil as a whole, I compute the end-to-end vector autocorrelation:

$$\left\langle RR(s)\right\rangle\Big|_{\text{Sim}} \equiv \frac{\int_{t=0}^{t=D-s} \underline{R}(t+s)\bullet\underline{R}(t)\ dt}{\int_{t=0}^{t=D-s} \underline{R}(t)\bullet\underline{R}(t)\ dt} \tag{55}$$

where $\underline{R}(t)=\underline{r}^{N_S+1}(t)-\underline{r}^{1}(t)$, D is total simulation duration, and s is the autocorrelation time interval.

To analyze behavior at the level of individual Fraenkel springs, I compute the unit spring vector autocorrelation:

$$\left\langle uu(s)\right\rangle\Big|_{\text{Sim}} \equiv \frac{\int_{t=0}^{t=D-s} \sum_{i=1}^{N_S} \underline{u}^{i}(t+s)\bullet\underline{u}^{i}(t)\ dt}{\int_{t=0}^{t=D-s} \sum_{i=1}^{N_S} \underline{u}^{i}(t)\bullet\underline{u}^{i}(t)\ dt} \tag{56}$$

I note that the spring (or bond) orientational autocorrelation function closely mimics the behavior of the mechanical stress relaxation function, since bond orientational order is typically proportional to stress via the well-known stress-optic law.

To test the accuracy of my code, I compare the autocorrelation functions with only the stretching force acting on Hookean chains to theoretical predictions. The spring force acting on the infinitely extensible Hookean springs in the Rouse model is described by [28]:

$$\underline{F}_S^i = H\,\underline{R}_S^i \tag{57}$$

where

$$H = 2k_BT\beta_S^2 \tag{58}$$

$$\beta_S^2 = \frac{3N_S}{2\left\langle R^2\right\rangle_0} = \frac{3}{2\left\langle R^2\right\rangle_{0,S}} = \frac{3}{2C_\infty^T C_\infty^B l_0^2} \tag{59}$$

using which I can calculate the autocorrelation function for the individual Hookean springs as:

$$\left\langle R_S R_S(s)\right\rangle\Big|_{\text{Sim}} \equiv \frac{\int_{t=0}^{t=D-s}\sum_{i=1}^{N_S}\underline{R}_S^i(t+s)\bullet\underline{R}_S^i(t)\ dt}{\int_{t=0}^{t=D-s}\sum_{i=1}^{N_S}\underline{R}_S^i(t)\bullet\underline{R}_S^i(t)\ dt} \tag{60}$$

3.3.1. Theoretical autocorrelation functions (Rouse model)

For the Rouse model (with Hookean springs and no bending or torsional barriers), the dynamics can be resolved into independent modes. The end-to-end vector, $\underline{R}$, autocorrelation of the whole chain can be compared to the predictions of the Rouse model, yielding [19, 31, 47]:

$$\left\langle RR(s)\right\rangle\Big|_{\text{Th}} \approx \frac{1}{\alpha}\sum_{p=1,3,5\ldots}^{N_S}\frac{1}{p^2}\exp\left(-\frac{s}{\tau_p}\right) \tag{61}$$

where

$$\tau_p = \frac{\zeta}{8k_BT\beta_S^2\sin^2\left[p\pi/2(N_S+1)\right]} \tag{62}$$

with $\alpha = \sum_{p=1,3,5\ldots}^{N_S} 1/p^2$ and I set the mean square end-to-end distance of each spring equal to $3/2\beta_S^2 = \left\langle R^2\right\rangle_{0,S} = C_\infty^T C_\infty^B l_0^2$ so that it matches that of a chain with stretching, bending, and torsional potentials.

Similarly, autocorrelation functions of the unit Frankel spring vectors and Hookean spring vectors can be compared to theoretical predictions using [23, 31, 47]:

$$\left\langle uu(s)\right\rangle\Big|_{\text{Th}} \approx \frac{1}{N_S}\sum_{p=1,2,3\ldots}^{N_S}\exp\left(-\frac{s}{\tau_p}\right) \tag{63}$$

and

$$\left\langle R_S R_S(s)\right\rangle\Big|_{\text{Th}} = \frac{1}{N_S}\sum_{p=1,2,3\ldots}^{N_S} \exp\left(-\frac{s}{\tau_p}\right) \tag{64}$$

respectively with equation 63 being an approximation valid at large s.

I observe in Figure 22 that for Rouse chains (i.e., Hookean springs and no bending and torsional potentials) my simulation autocorrelation functions – $\left\langle RR(s)\right\rangle$ and $\left\langle R_S R_S(s)\right\rangle$ – are in perfect agreement with the theoretical predictions for chains with forty springs, N_S = 40, and I also observe the -0.5 power-law region clearly appearing in the decay of $\left\langle R_S R_S(s)\right\rangle$ which establishes the accuracy of my simulation code.

3.3.2. Stiff spring potential

Now, moving towards locally more resolved models, I first introduce the bond stretching force using the stiff Fraenkel spring potential. As is the case for Hookean springs, I observe excellent agreement of the predicted end-to-end vector autocorrelation function with that of the Rouse theory as can be seen in Figure 23.

While for Hookean springs there is nearly perfect agreement between simulations and theory for both the end-to-end vector and the spring vector autocorrelation functions, I observe modest differences between simulations and Rouse predictions of the spring vector autocorrelation function at times in the neighborhood of 10^{-12} to 10^{-11} s in Figure 24 on introducing Fraenkel springs. The modest discrepancy at short times is expected since this range of times corresponds to the rotational times of just one or a few bonds—too few to act as an effective Hookean spring. At longer times, $t > 10^{-11}$ s, the response is dominated by the collective motion of five to ten or more bonds, which is a

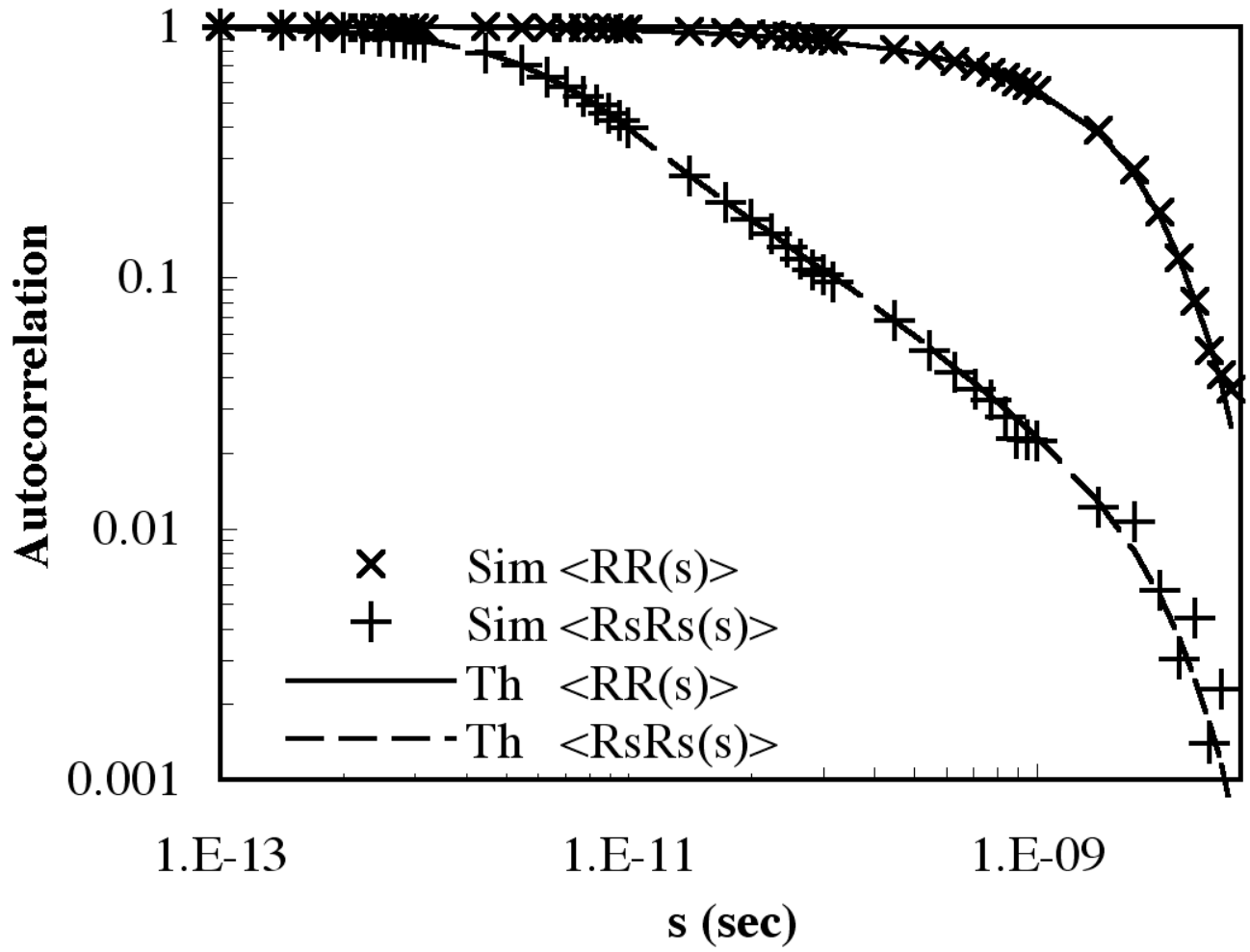

Figure 22. Comparison of simulated (Sim) and theoretical Rouse (Th) autocorrelation functions, <RR(s)> and $\langle R_S R_S(s) \rangle$ for $N_S = 40$ using Hookean springs.

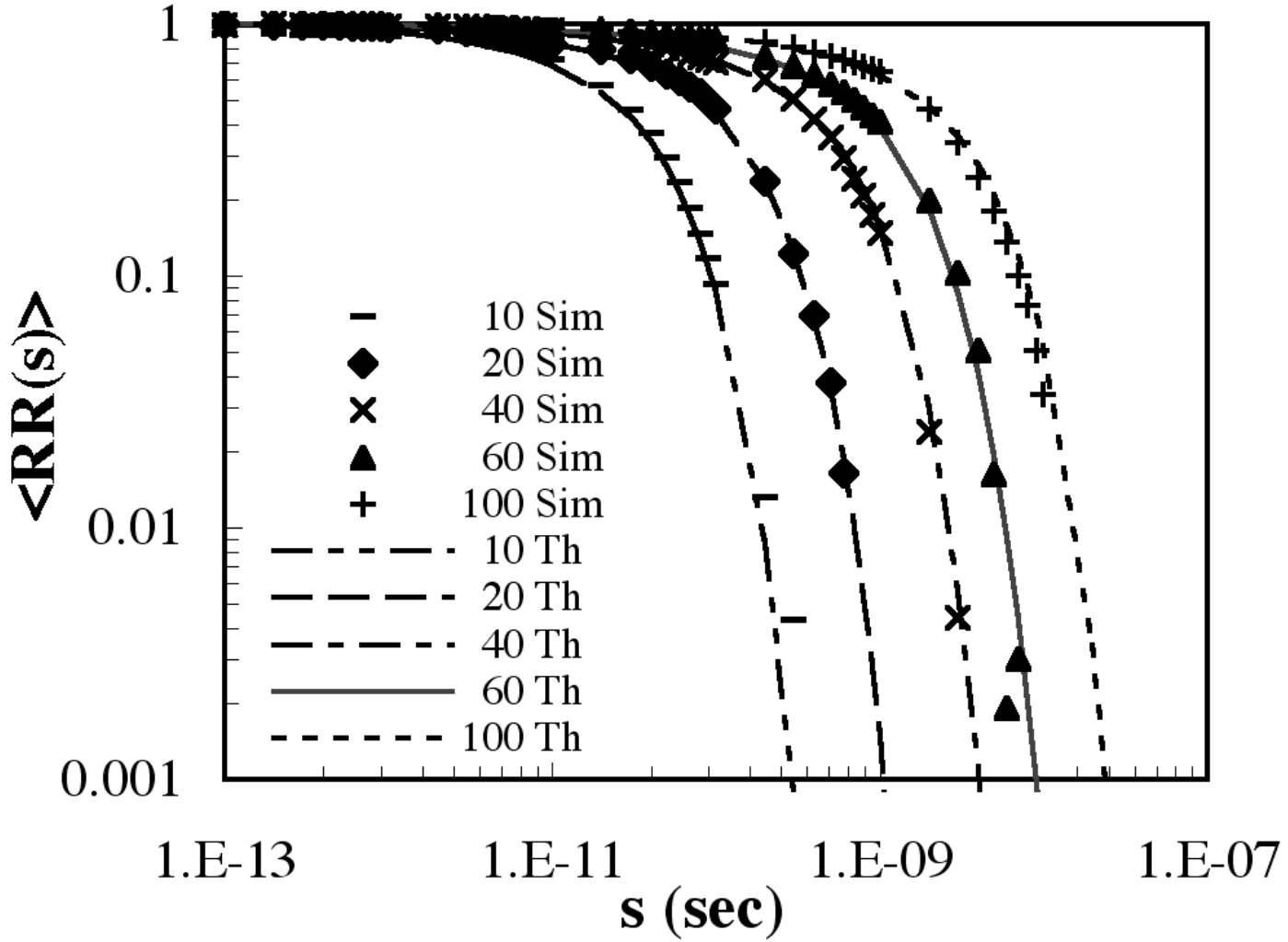

Figure 23. Comparison of simulated (Sim) and theoretical Rouse (Th) autocorrelation function <RR(s)> for N_S = 10, 20, 40, 60, and 100 using Fraenkel springs with only Fraenkel stretching potential and no bending or torsional potentials.

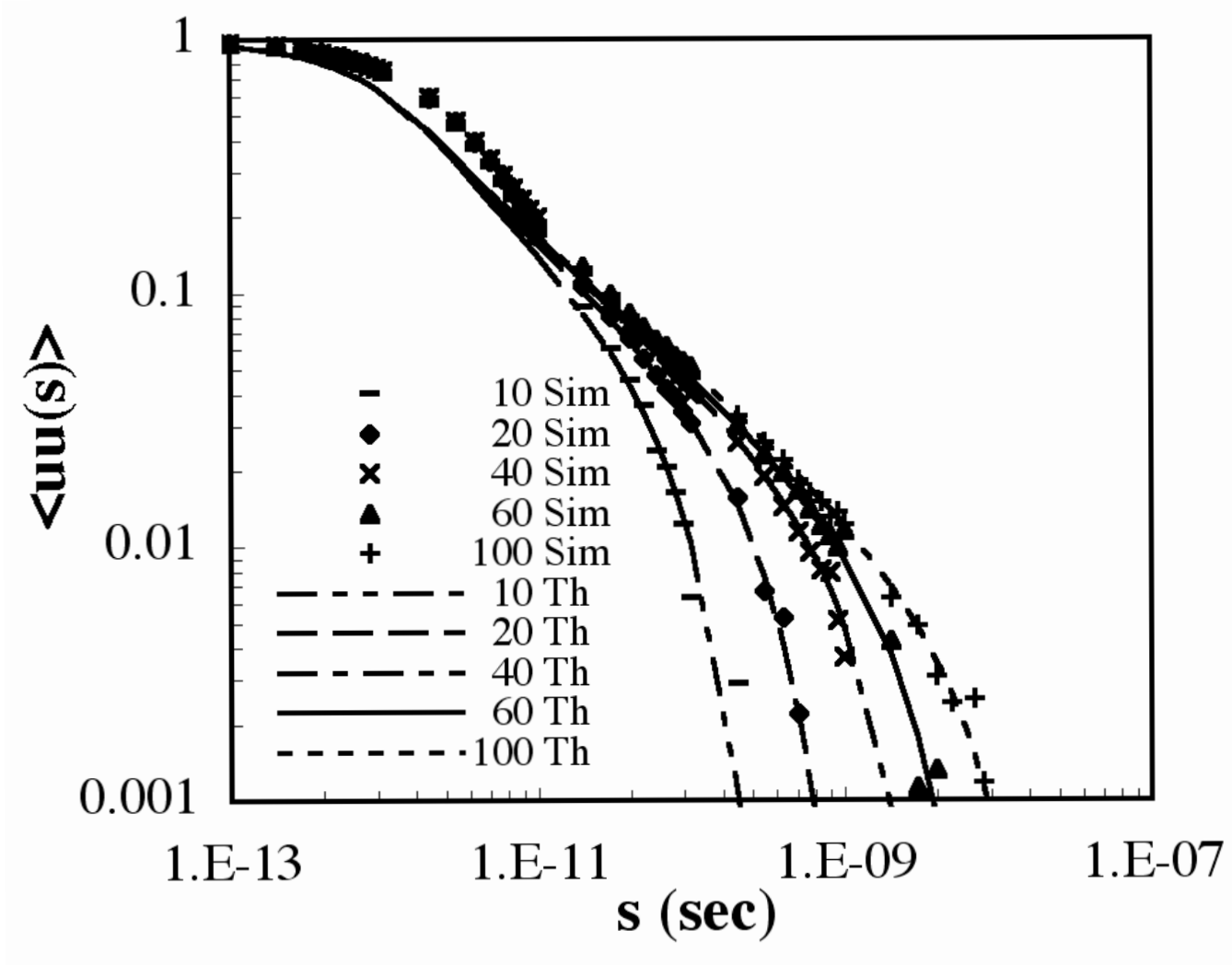

Figure 24. Same as Figure 23 except for unit spring vector autocorrelation function, <uu(s)>.

sufficient number to act collectively as an effective Hookean spring. Hence, for $t > 10^{-11}$ s, there is good agreement between Rouse theory and simulations of chains with Fraenkel springs and no bending or torsional potentials.

3.3.3. Bending angle potential

Second, I add the bending force. Theoretically, the tetrahedral bonding angle is 109^0 47' ($\theta_C = 70^0$ 13') implying that $\cos\theta_C = 0.3333$. Since I am using a softened coefficient for the bending potential, the distribution of bending angles is broadened in Figure 20 relative to the "true" distribution. If I take into account this distribution in bending angles, from the simulation results, I obtain $\langle \cos\theta_C \rangle = 0.3539$ which is within ~6% of the theoretical value for a fixed bending angle of 109^0 47'. As is the case with stretching force only, when stretching and bending forces are both included, the simulated end-to-end vector autocorrelation function agrees increasingly well with the Rouse theory as the number of springs increases until nearly perfect agreement is obtained when N_S reaches 60 springs as can be seen in Figure 25. Note that the relaxation of the end-to-end vector is dominated by the terminal relaxation process which can be deduced from the $1/p^2$ weighting of the modes in equation 61.

Figure 26 shows the bond vector autocorrelation function for N_S = 10, 20, 60, and 100 springs. At short and intermediate times, the bond vector decays more slowly than in the Rouse predictions, although agreement is recovered in the terminal region which is expected since the simulated end-to-end vector relaxation $\langle RR(s) \rangle$ matches the Rouse predictions quite well as can be seen in Figure 25. Thus, unlike the effect of the fixed

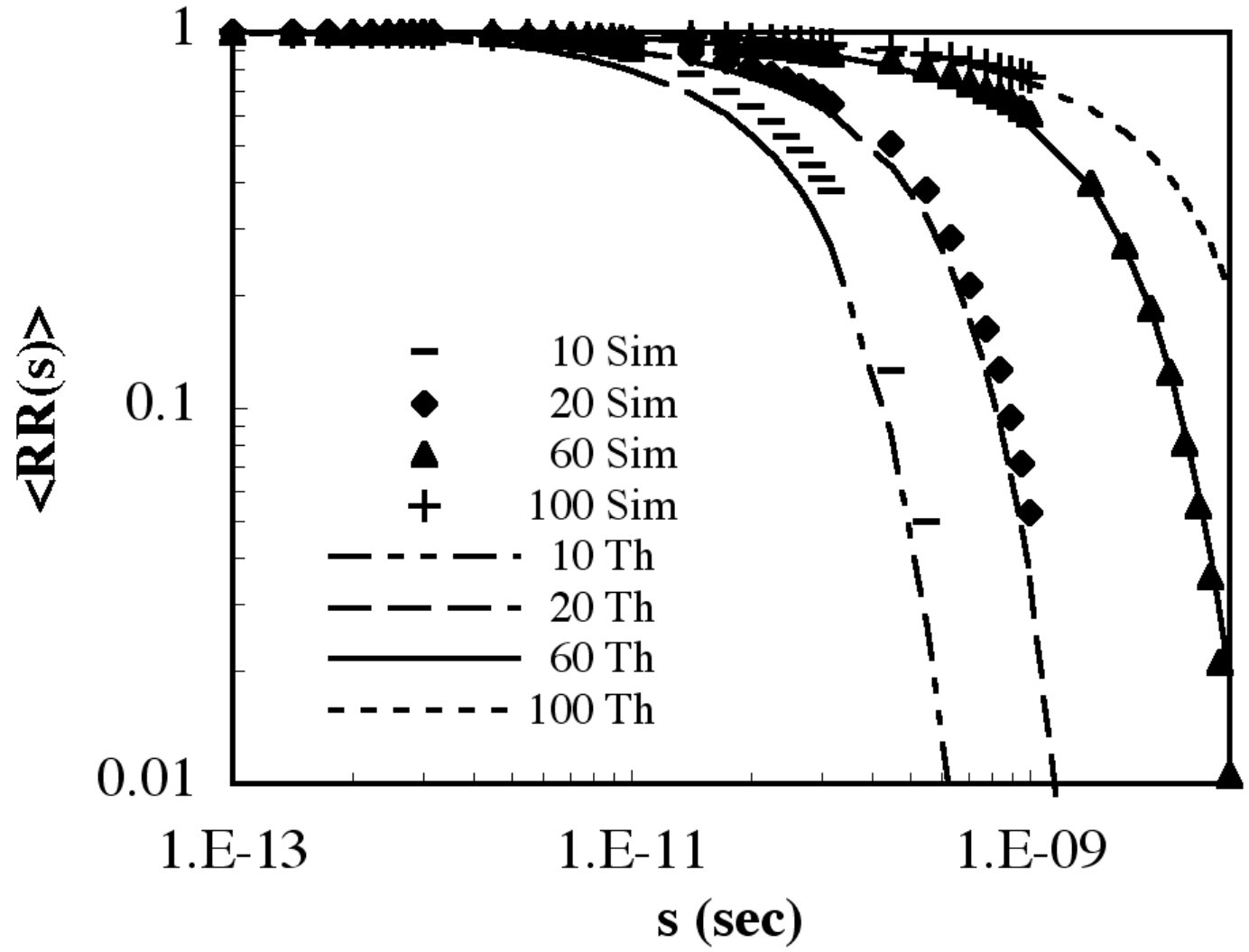

Figure 25. Comparison of simulated (Sim) and theoretical Rouse (Th) autocorrelation function, <RR(s)> for N_S = 10, 20, 60, and 100 using Fraenkel springs with Fraenkel stretching and bending forces.

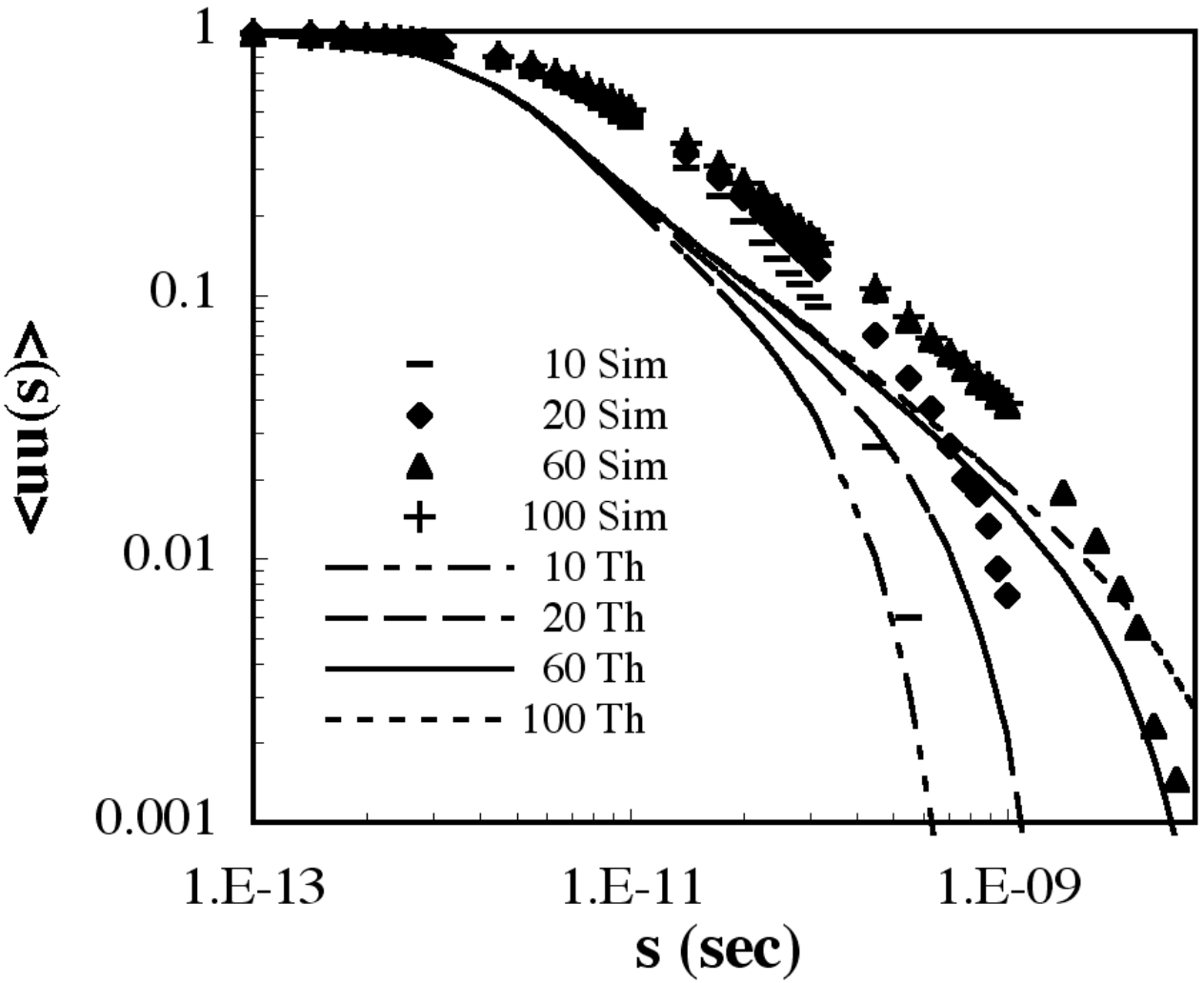

Figure 26. Same as Figure 25 except for unit spring vector autocorrelation function <uu(s)>.

bond length which only influences the short time relaxation, the bending angle potential influences the relaxation—even for chains of 100 bonds—out nearly to the terminal time. What is particularly interesting is that when $N_S \geq 60$, $\langle uu(s) \rangle$ recovers the power-law time regime with slope similar to that of the Rouse theory, but displaced to longer times. Eventually, at long times, the dynamics of the coil as a whole overshadow such local effects and hence the coil relaxation matches the Rouse prediction.

3.3.4. Torsional potential

I now examine the effect of the torsional potential by running the simulations at 0%, 100%, and 200% of the "base" barrier height of 12.36 kJ/kg between the trans and gauche states. When the barrier height is 0%, so that only the cis barrier exists, small deviations between the theoretical and simulated function $\langle RR(s) \rangle$ are apparent even for N_S = 60 in Figure 27. Thus, the torsional forces, even with no trans-gauche barrier, increase the coil stiffness which affects relaxation of the chain even on long length scales. This difference between theory and simulation increases with the rise in gauche/trans barrier height as is seen in Figure 28 with at a barrier height of 100%. While the effects are evident only for chains up to 60 springs in length for smaller barrier heights, I see in Figure 29 deviations creep in for even 100 springs at a barrier height of 200%. Additionally, as the barrier height increases, the average value of the cosine of the torsional angle, $\langle \cos\phi \rangle$, decreases from 0.4918 (for 0% barrier height) to 0.3643 (for 200% barrier height) as is clear from the probability distribution function in Figure 21. This reduces the torsional characteristic ratio, C_∞^T, from 2.94 to 2.15 showing that the coil

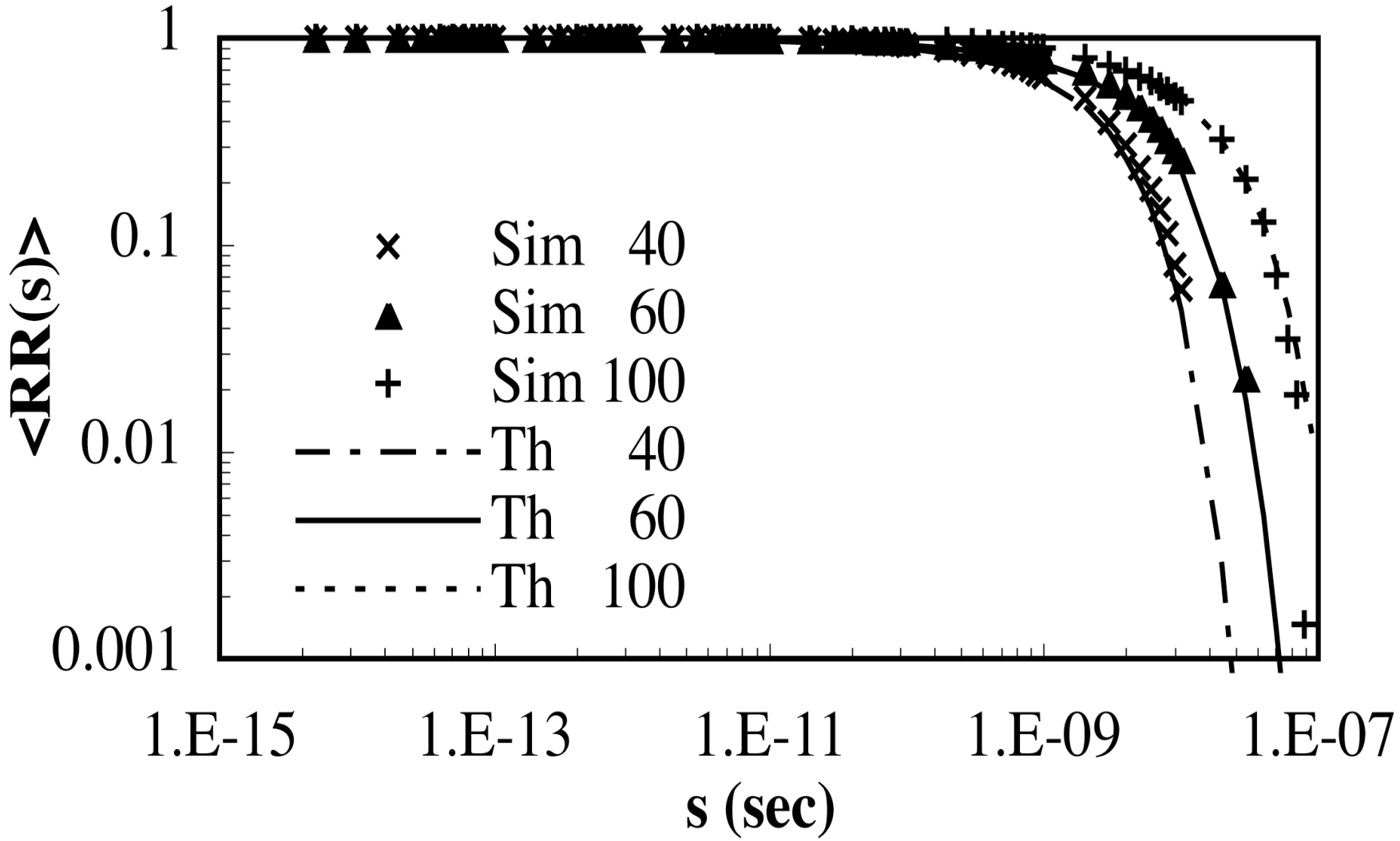

Figure 27. Comparison of simulated (Sim) and theoretical Rouse (Th) autocorrelation function, <RR(s)> for N_S = 40, 60, and 100 using Fraenkel springs with Fraenkel stretching, bending, and torsional forces with trans/gauche barrier height being 0% of the base height.

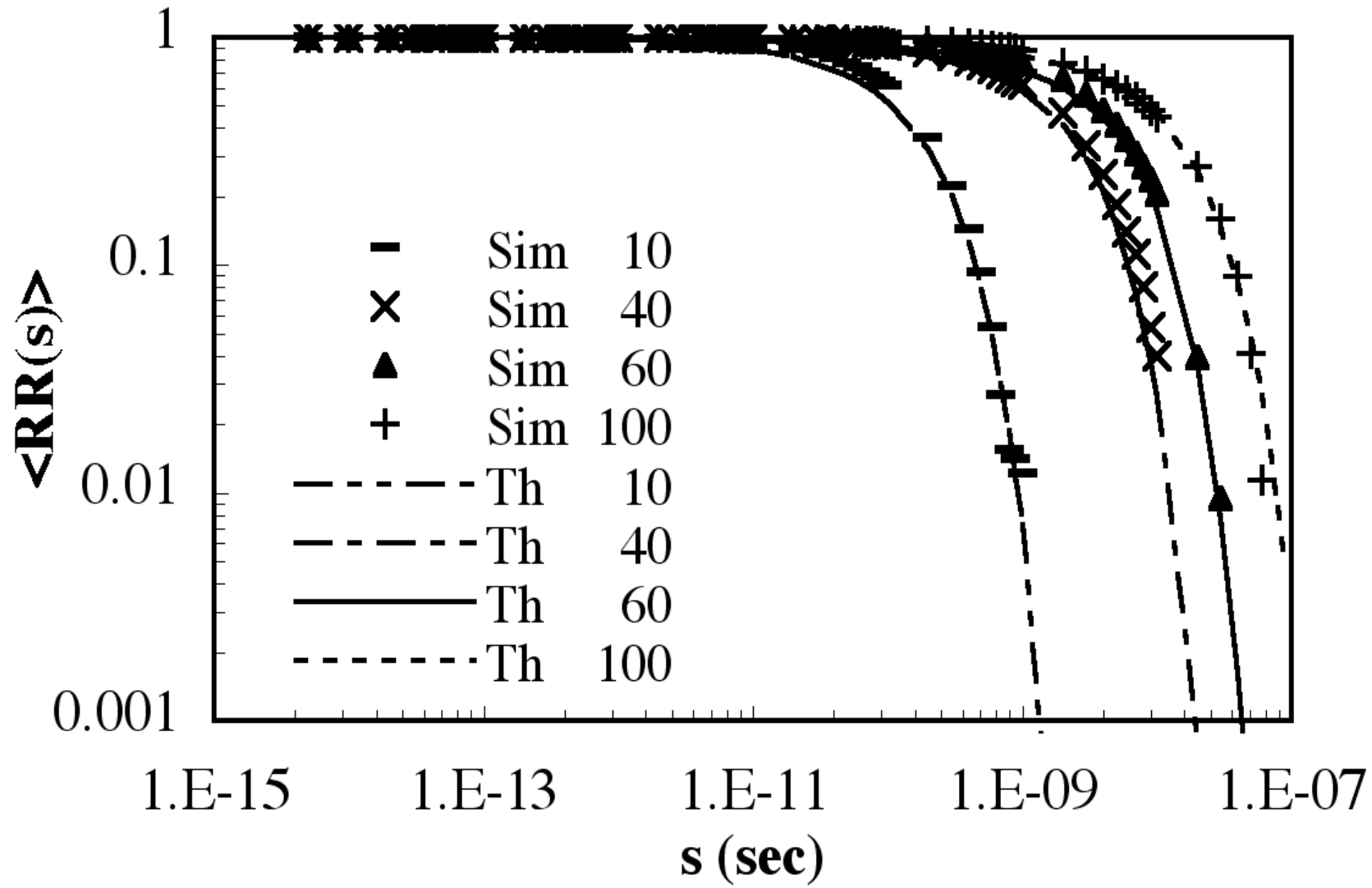

Figure 28. Comparison of simulated (Sim) and theoretical Rouse (Th) end-to-end vector autocorrelation function, <RR(s)> for N_S = 10, 40, 60, and 100 using Fraenkel springs with Fraenkel stretching, bending, and torsional forces with trans/gauche barrier being 100% of the base height.

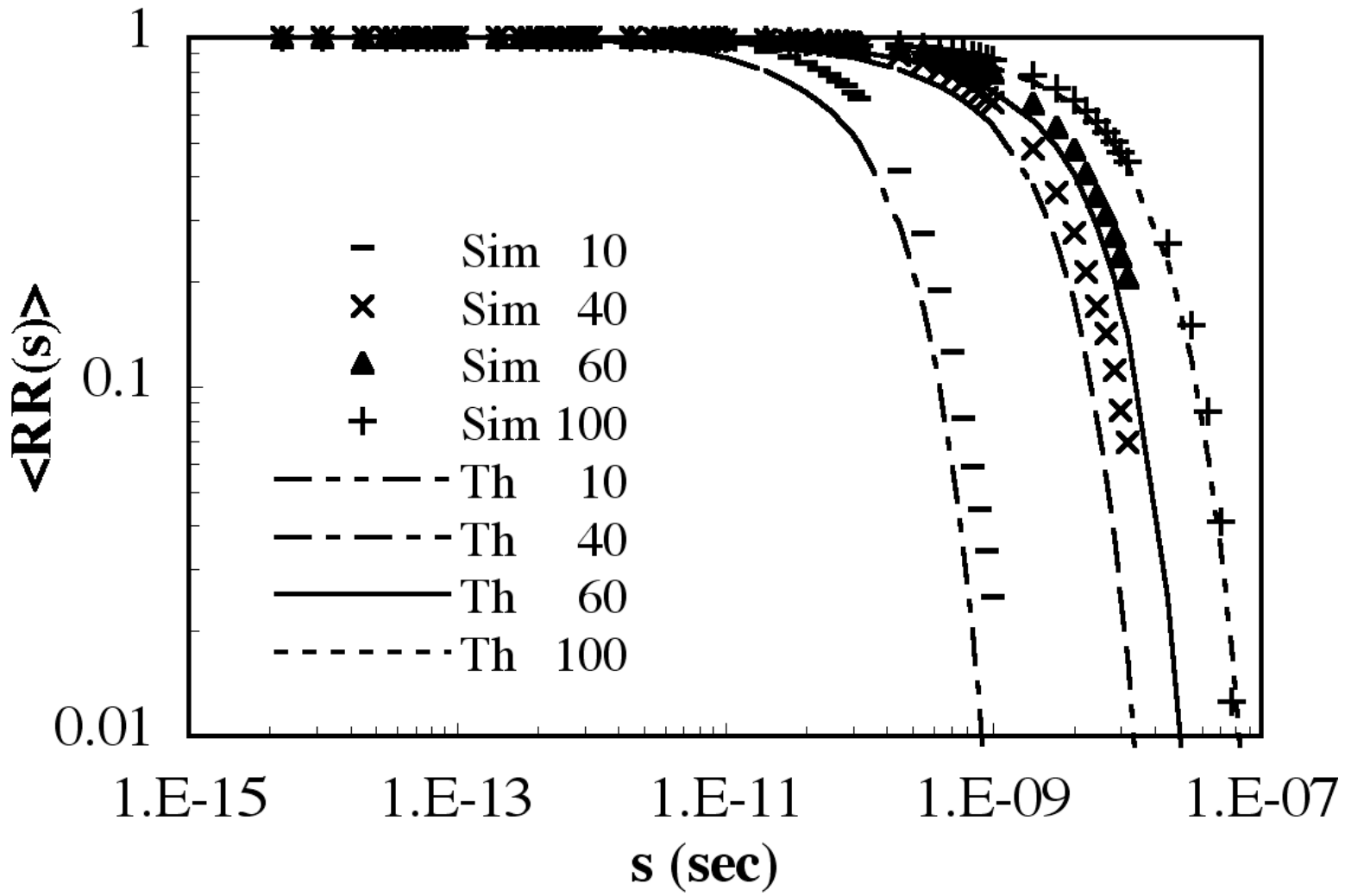

Figure 29. Comparison of simulated (Sim) and theoretical Rouse (Th) end-to-end vector autocorrelation function <RR(s)> for N_S = 10, 40, 60, and 100 using Fraenkel springs with Fraenkel stretching, bending, and torsional forces with trans/gauche barrier being 200% of the base height.

shrinks slightly leading to faster terminal relaxations. Figure 30 shows this more clearly when N_S = 60 with trends from simulations and the Rouse theory, since I include C_∞^T in my calculation of the Rouse relaxation time spectrum as shown in equations 61 and 62.

Next, I identify the effect of changing the torsional barrier height on the unit spring vector autocorrelation function. As is seen from Figure 31, as soon as the cis barrier is introduced (with trans/gauche barrier absent), the power law region completely disappears from the unit spring vector autocorrelation functions, even for N_S = 60. The polymer relaxes much slower than predicted by the Rouse model at both short and intermediate times and there is a rapid decay at long times. Thus, relaxation resembles that of a single spring (i.e., a single exponential decay) more closely than that of a Rouse bead-spring chain. When the trans/gauche barrier is introduced at 100% of the base height in Figure 32, I observe emergence of the power law region as the number of springs increases to 60 or higher but greatly shifted to longer times relative to the Rouse predictions. Still, for short chains (N_S < 40), the short and intermediate time behavior deviates noticeably from Rouse behavior. When the trans/gauche barrier is increased to 200% of the base height, Figure 33 shows that even when a chain has 100 springs, the power law region is not recovered. As is observed for the autocorrelation function for the end-to-end vector for N_S = 60, Figure 34 shows the Rouse theoretical unit spring vector autocorrelation function relaxes marginally faster with increasing barrier height because of the slight coil size contraction discussed above. All the same, simulations show that as the barrier height increases, relaxation is increasingly suppressed at short and intermediate times.

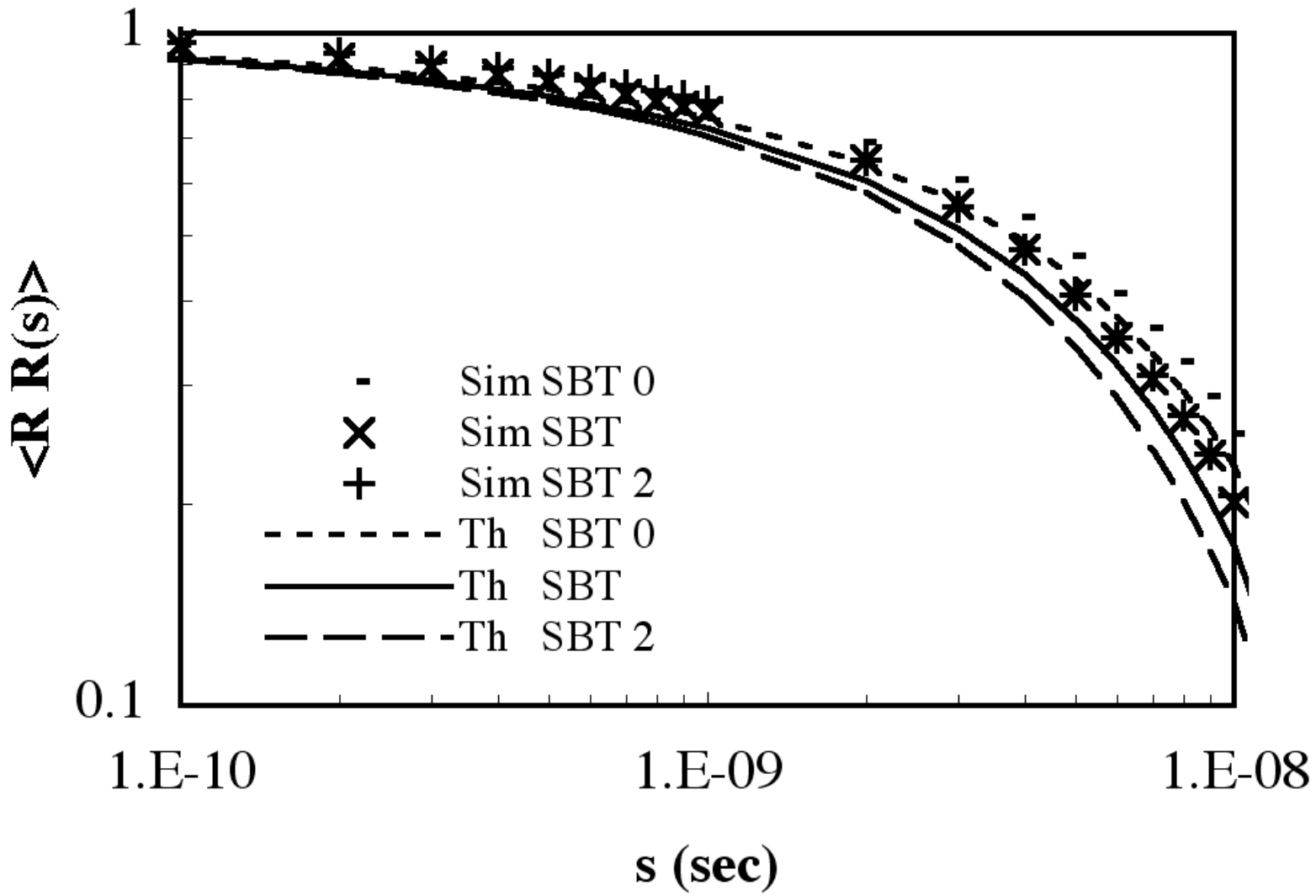

Figure 30. Comparison of simulated (Sim) and theoretical Rouse (Th) end-to-end vector autocorrelation function <RR(s)> for $N_S = 60$ for barrier heights between the gauche/trans states being 0%, 100%, and 200% of the base values.

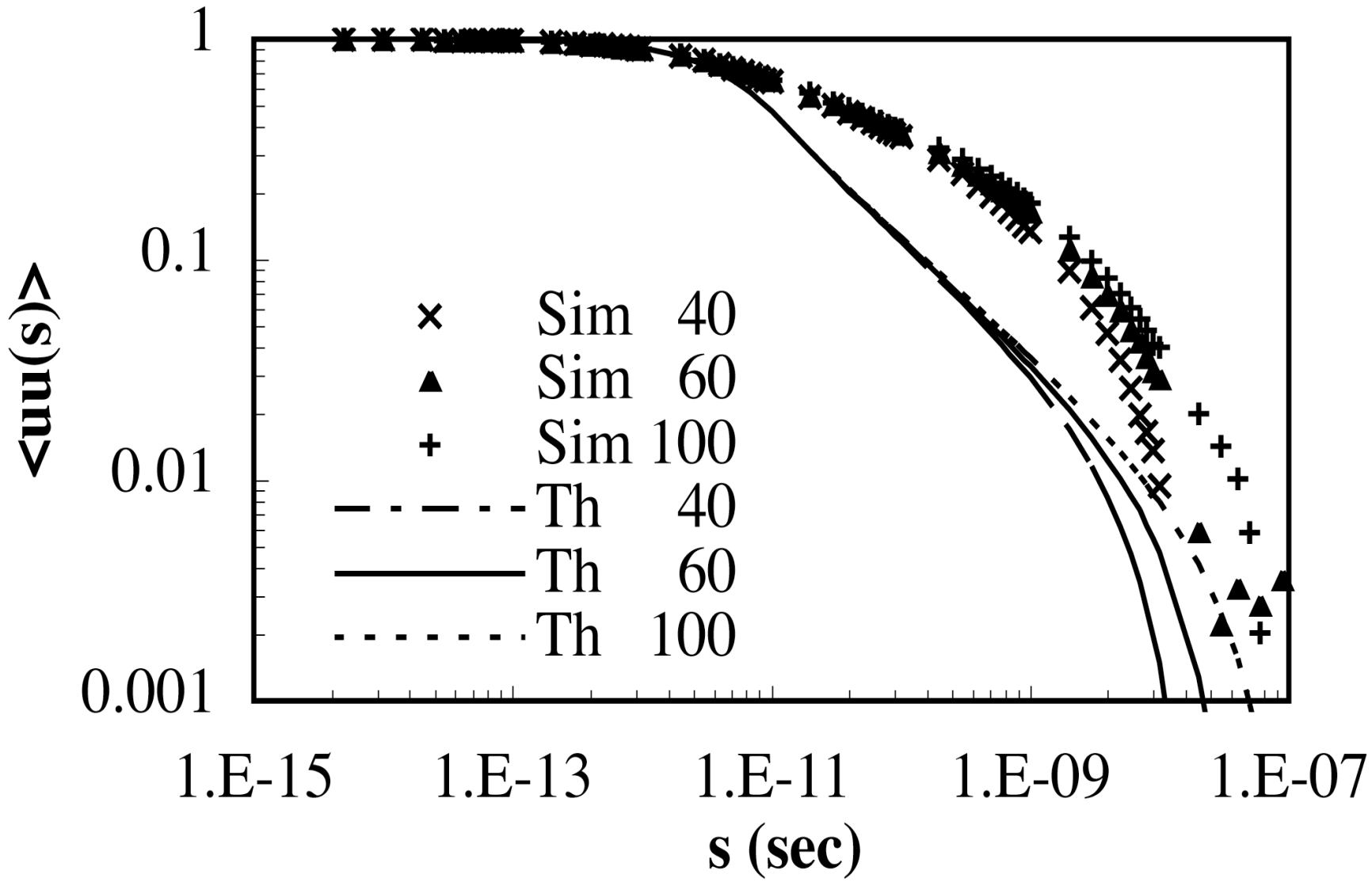

Figure 31. Same as Figure 27, except for unit spring vector autocorrelation function, <uu(s)>.

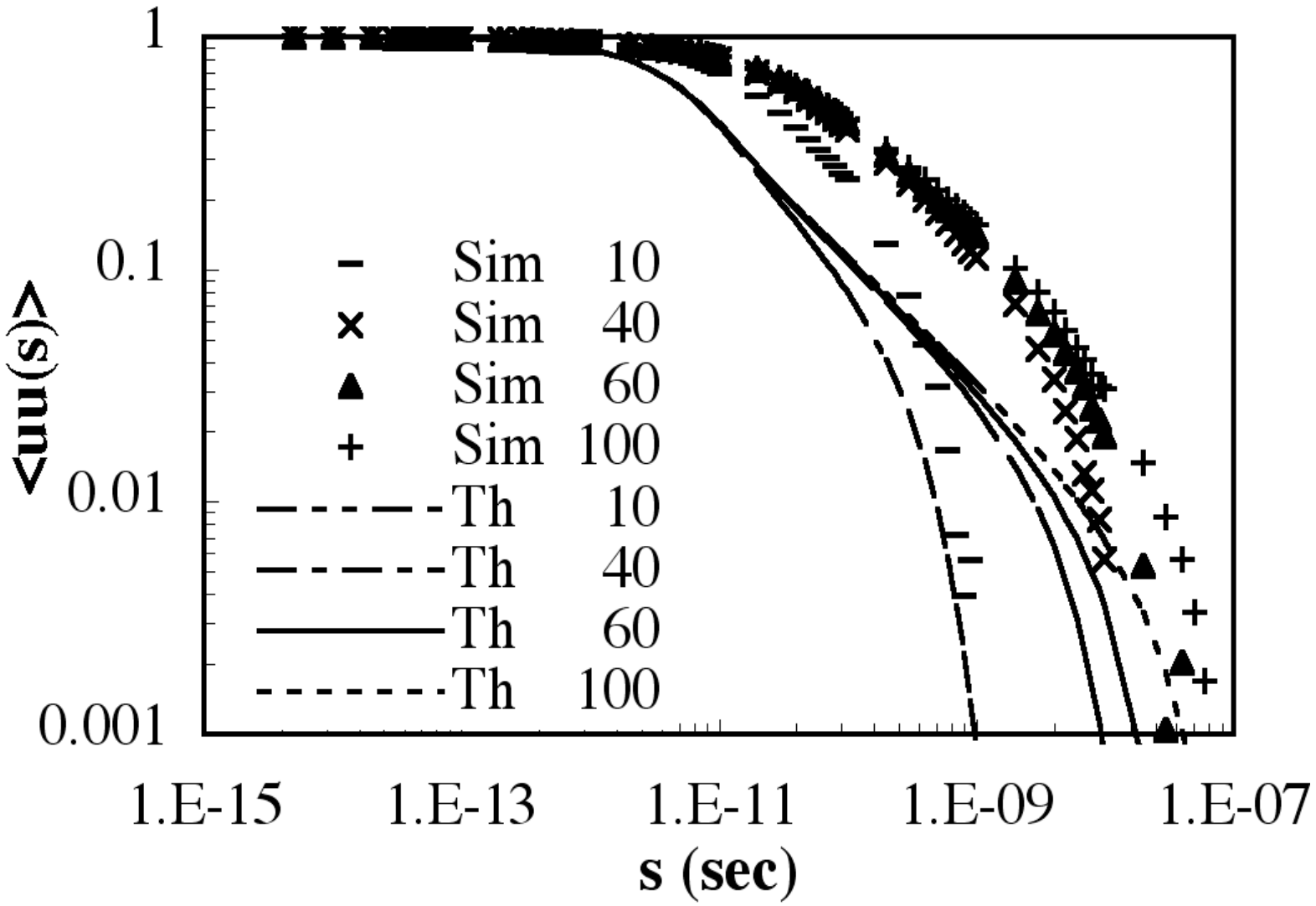

Figure 32. Same as Figure 28, except for unit spring vector autocorrelation function, <uu(s)>.

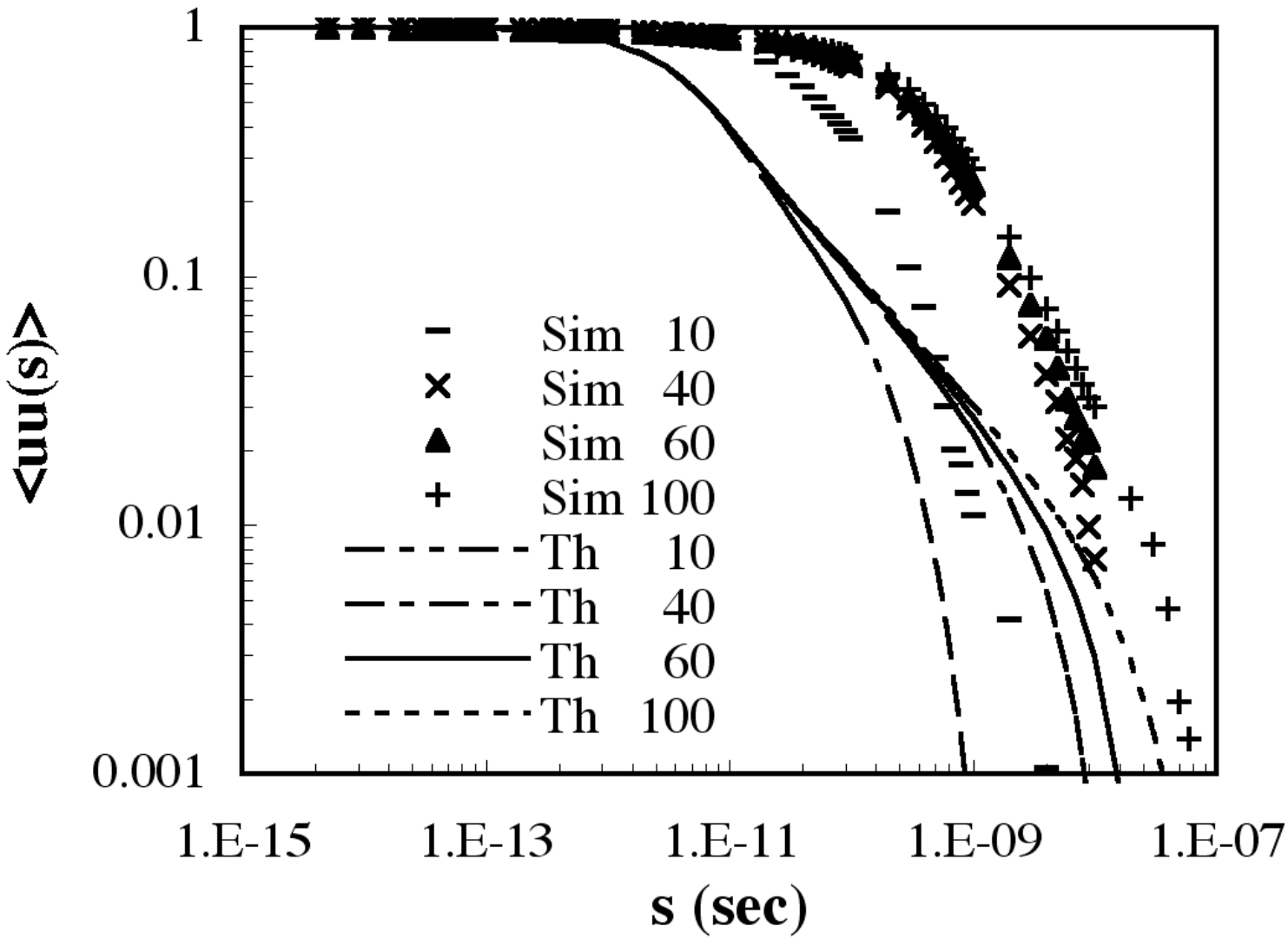

Figure 33. Same as Figure 29, except for unit spring vector autocorrelation function, <uu(s)>.

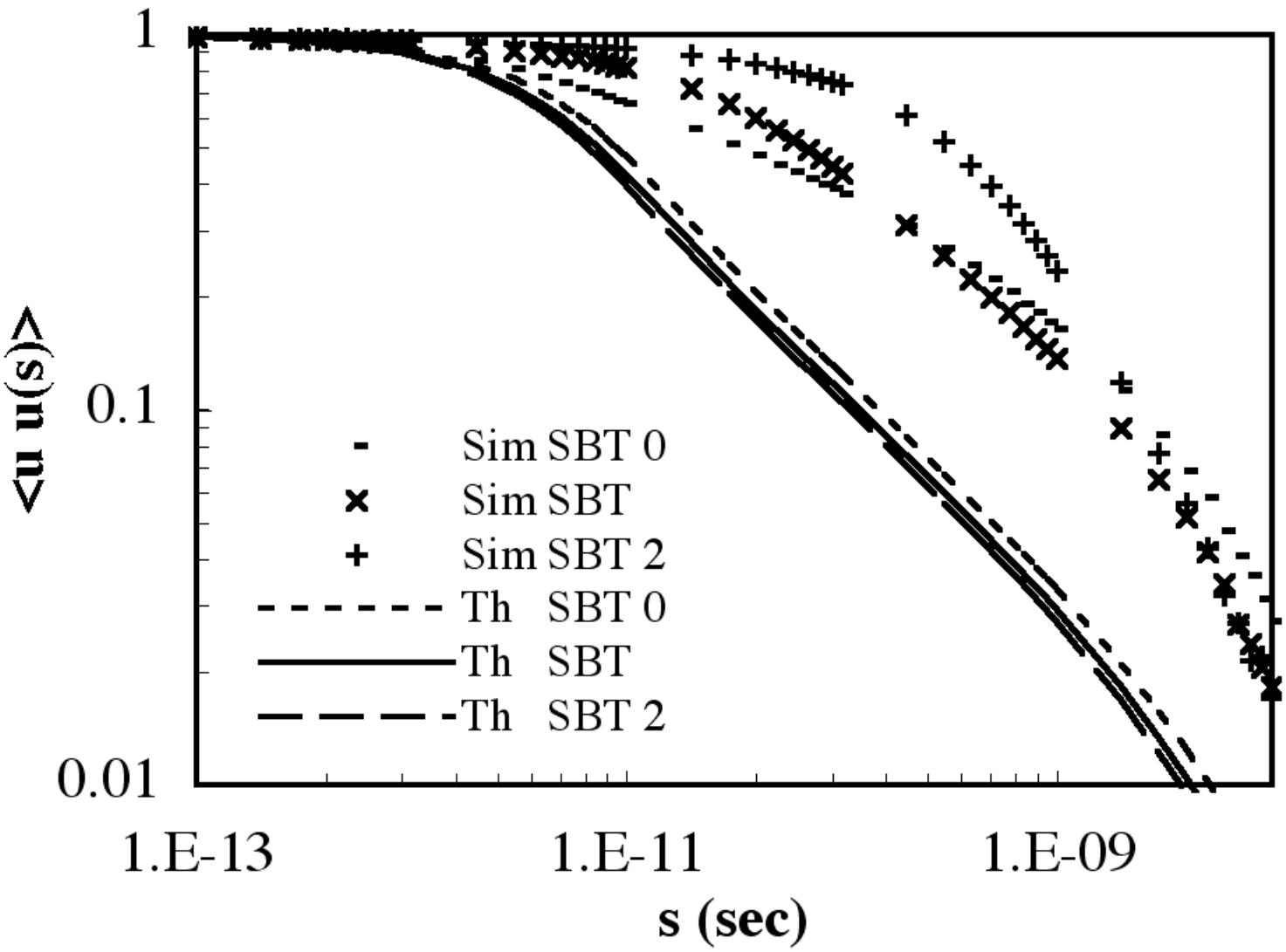

Figure 34. Same as Figure 30 except for unit spring vector autocorrelation function <uu(s)>.

3.4. Discussion

I have found that the inclusion of bending and torsional potentials into a polymer chain model drastically alters the modes of polymer relaxation relative to the Rouse model. Even rather slow modes that involve coordinated motions of tens of bonds are affected, while the terminal relaxation time is left nearly unchanged. I also find that the suppression of internal modes becomes more severe as the torsional barrier separating trans and gauche states increases.

The suppression of internal modes is evidently a consequence both of the loss of configurational states produced by addition of bond angle constraints and of the slowing down of torsional transitions. This shifts the time scale of local modes towards the terminal time scale governing the relaxation of the molecule as a whole. The terminal mode is unshifted because it is governed mostly by pure rotational diffusion of the molecule as a whole. Even if internal degrees of freedom were to be completely rigidified by imposing very high barriers to bond rotation, the chain as a whole could still rotate as a rigid object in the solvent and so relax its end-to-end vector in a time comparable to that of a completely limp coil of the same radius.

Changing the bond stretching potential from Hookean to a stiff Fraenkel spring has little effect on the relaxation spectrum except at short times. However, incorporation of a bending potential significantly slows the bond relaxation on both short and intermediate time scales. Presumably, the imposition of a strongly preferred bending angle makes complete relaxation, i.e., complete exploration of orientation space, of a given bond much more dependent on motion of other more-distant bonds than is the case in the absence of a bending potential. Inclusion of a cis-torsional barrier further limits

bond reorientation, and additional imposition of a trans-gauche barrier not only shrinks the available conformational space but also slows even local sampling of that space.

3.4.1. Effect of coarse graining

Now, I examine the extent to which the behavior described above can be understood through standard coarse-graining approximations. Starting from a "realistic" polymer model with bending and torsional potentials, one can construct an "equivalent" coarse-grained (CG) freely jointed chain model that possesses the same mean square end-to-end vector, $\left\langle R^2 \right\rangle_0$, as the realistic chain and the same fully extended length, *L*, via the relationships:

$$\left\langle R^2 \right\rangle_0 = C_\infty n l^2 \tag{65}$$

$$L = 0.82 n l = N_K b_K \tag{66}$$

where N_K is the number of bonds ("Kuhn steps") and b_K (the "Kuhn length") is the length of a bond in the "equivalent" freely jointed chain model which has the same mean square end-to-end vector and same contour length as the realistic chain. The factor of 0.82 arises from the zig-zag configuration of the "fully extended length" of the chain, which results from the tetrahedral bending angle. The above formulas allow us to obtain $N_K = 0.82^2 n / C_\infty$ and $b_K = C_\infty l / 0.82$.

When bending and torsional potentials are absent, $C_\infty = 1$, while imposition of a bending potential yields $C_\infty = C_\infty^B = 2$, and bending plus torsional potentials produces $C_\infty = C_\infty^B C_\infty^T$ = 5.8710, 4.8200, and 4.2923 for 0%, 100%, and 200% trans-gauche barrier heights. So, I can construct an "equivalent" freely jointed chain model for a chain with N_S

springs and a bending potential and torsional potential by using a model with only a stiff spring Fraenkel spring potential and no bending potential, whose contour length and mean-square end-to-end length match those of the chain with bending and torsional potential. This requires that the "equivalent" freely jointed chain model must have a reduced number of bonds, namely $N_K = 0.82^2 n/C_\infty$ and a longer bond length, namely $b_K = C_\infty l/0.82$, i.e., longer but fewer "CG" bonds. In addition, since the "equivalent" freely jointed chain has fewer beads than the original "realistic" chain, to reproduce the same total frictional drag, $\zeta_T|_0$, the drag coefficient on each bead in the CG chain needs to be increased so that the product of the number of beads and the bead drag coefficient remains the same as in the original chain, i.e., $\zeta_T|_{CG} = \zeta_T|_0 \Rightarrow \zeta|_{CG} = \zeta|_0 \left(N_S+1\right)\big|_0 / \left(N_S+1\right)\big|_{CG}$. Equivalently, I can simply multiply the time axis of the CG simulation by the ratio $\left(N_S+1\right)\big|_0 / \left(N_S+1\right)\big|_{CG}$ where $\left(N_S+1\right)\big|_{CG}$ is the number of beads in the CG chain and $\left(N_S+1\right)\big|_0$ is the number of beads in the original chain.

In Figure 35, I compare the autocorrelation functions using a 60-bond chain with bending potential to those for an equivalent coarse-grained chain using only stiff Fraenkel springs, i.e., 20 CG bonds $\left(N_K = 0.82^2 n/C_\infty = 0.336 N_S = 20\right)$ with each bond being 3.7317 $\overset{0}{\text{A}}$ long. For reference, I also show the theoretical Rouse predictions. Figure 35 shows that $\langle RR(s)\rangle$ of the coarse-grained simulation with 20 freely jointed bonds perfectly matches that of the fine-grained simulations of chains with 60 bonds that have a bending potential. This implies that a coarse-grained model that uses only stiff springs is

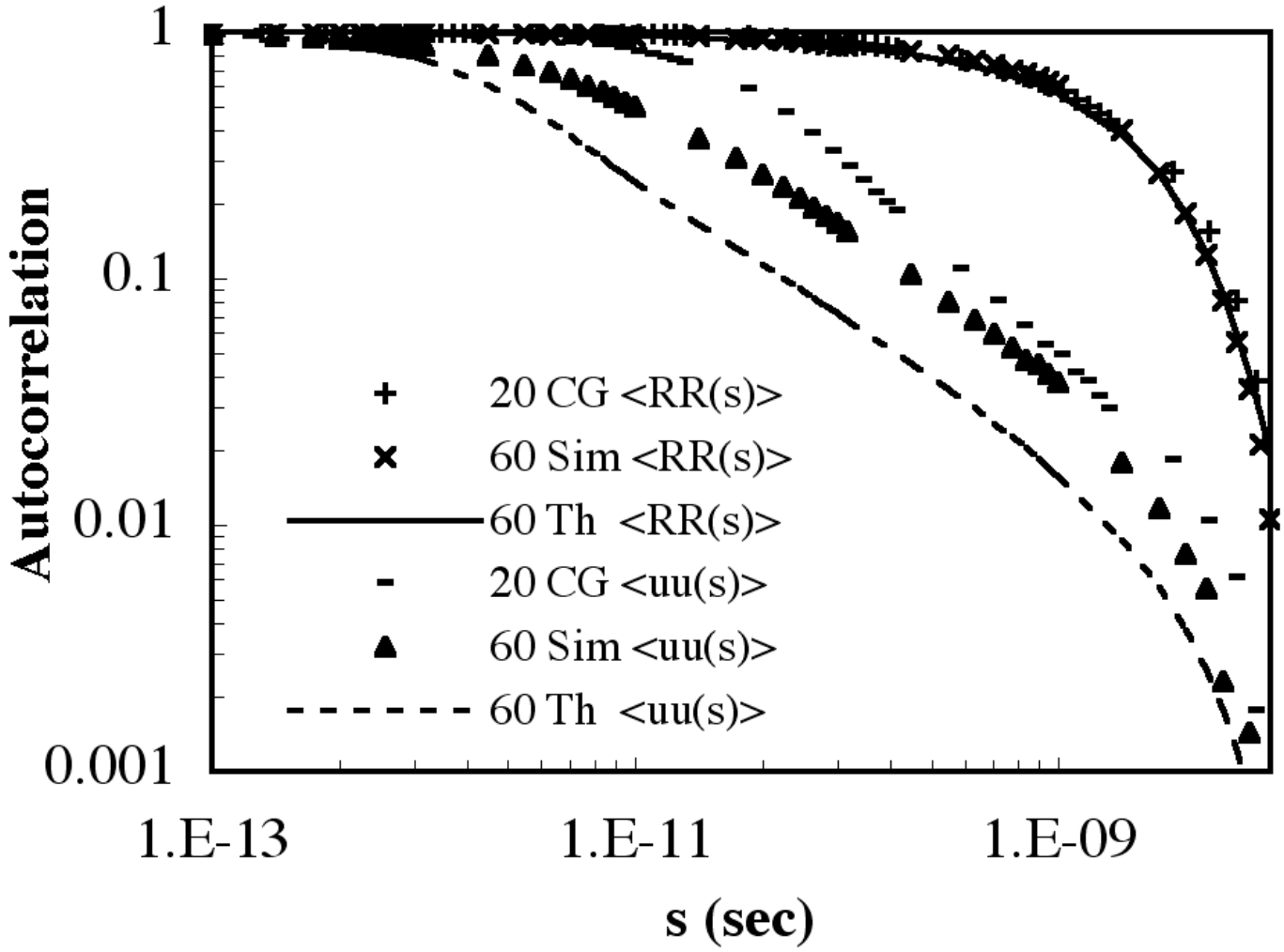

Figure 35. Comparison of simulated (Sim) and theoretical Rouse (Th) autocorrelation functions <RR(s)> and <uu(s)> using Fraenkel springs with stretching and bending potential with N_S = 60. These results have been compared with N_S = 20 and b = 3.73 x 10^{-10} m, i.e., coarse-grained (CG) bonds with only stretching potential acting on them.

able to capture the end-to-end vector relaxation of a "fine-grained" chain with a bending potential. However, for the autocorrelation function of individual springs, $\langle uu(s) \rangle$, the CG model shows a slower relaxation on intermediate time scales than does the simulations using 60 realistic bonds. Thus, except in the terminal region, the coarse-grained model is unable to capture the intermediate-scale dynamics of chains with a bending potential.

Similarly, a coarse-grained chain "equivalent" to a 60-bond chain with both bending and torsional potentials has N_K = 6 or 7 bonds of length b_K = 10.9544 $\overset{0}{\text{A}}$ when the trans-gauche barrier height is 0%, N_K = 8 or 9 and b_K = 8.9934 $\overset{0}{\text{A}}$ when the trans-gauche barrier height is 100%, and N_K = 9 or 10 and b_K = 8.0088 $\overset{0}{\text{A}}$ when the trans-gauche barrier height is 200%. Figures 36 – 38 show that with increasing barrier height (0%, 100%, and 200%), the difference between simulation results and CG predictions narrows significantly. Introduction of just the 'cis' torsional barrier (0% trans/gauche barrier, seen in Figure 36) further reduces the available degrees of freedom relative to the chain with only bending potential. Figures 37 and 38 show the available degrees of freedom are further reduced as the trans/gauche barrier is added at 100% and then increased to 200%. I find that the CG predictions match the "fine simulations" better with increasing barrier height.

3.4.2. Torsional bond relaxation rate

Fixman [13] carried out a simulation of a simplified polymer model with 90^0 bending angle and three torsional barriers which showed suppression of fast and

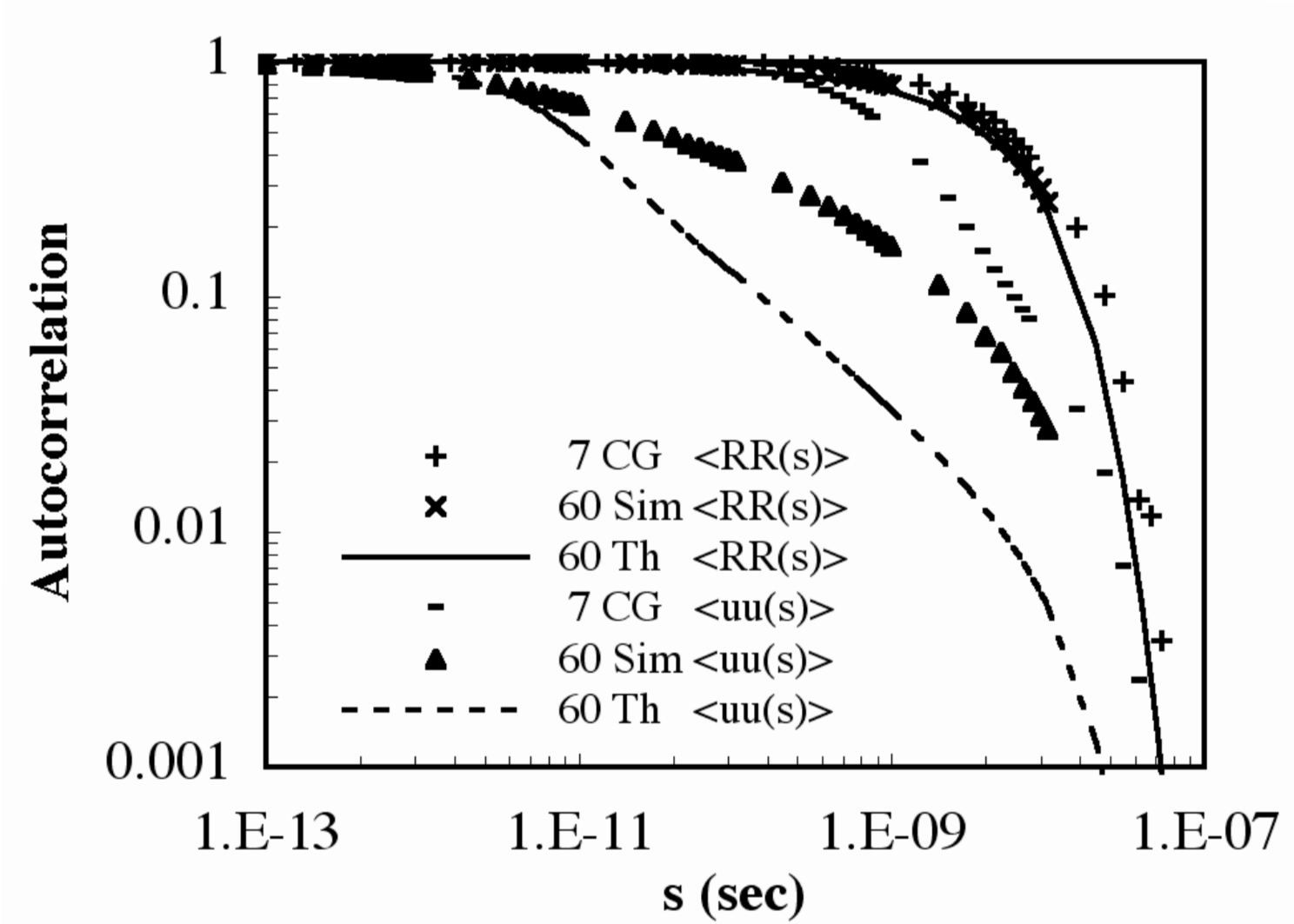

Figure 36. Comparison of simulated (Sim) and theoretical Rouse (Th) autocorrelation functions <RR(s)> and <uu(s)> using Fraenkel springs with stretching, bending, and torsional potentials with 0% gauche/trans barrier height with N_S = 60. These results have been compared with N_S = 7 and b = 10.9544 x 10^{-10} m, i.e., coarse-grained (CG) bonds with only stretching potential acting on them.

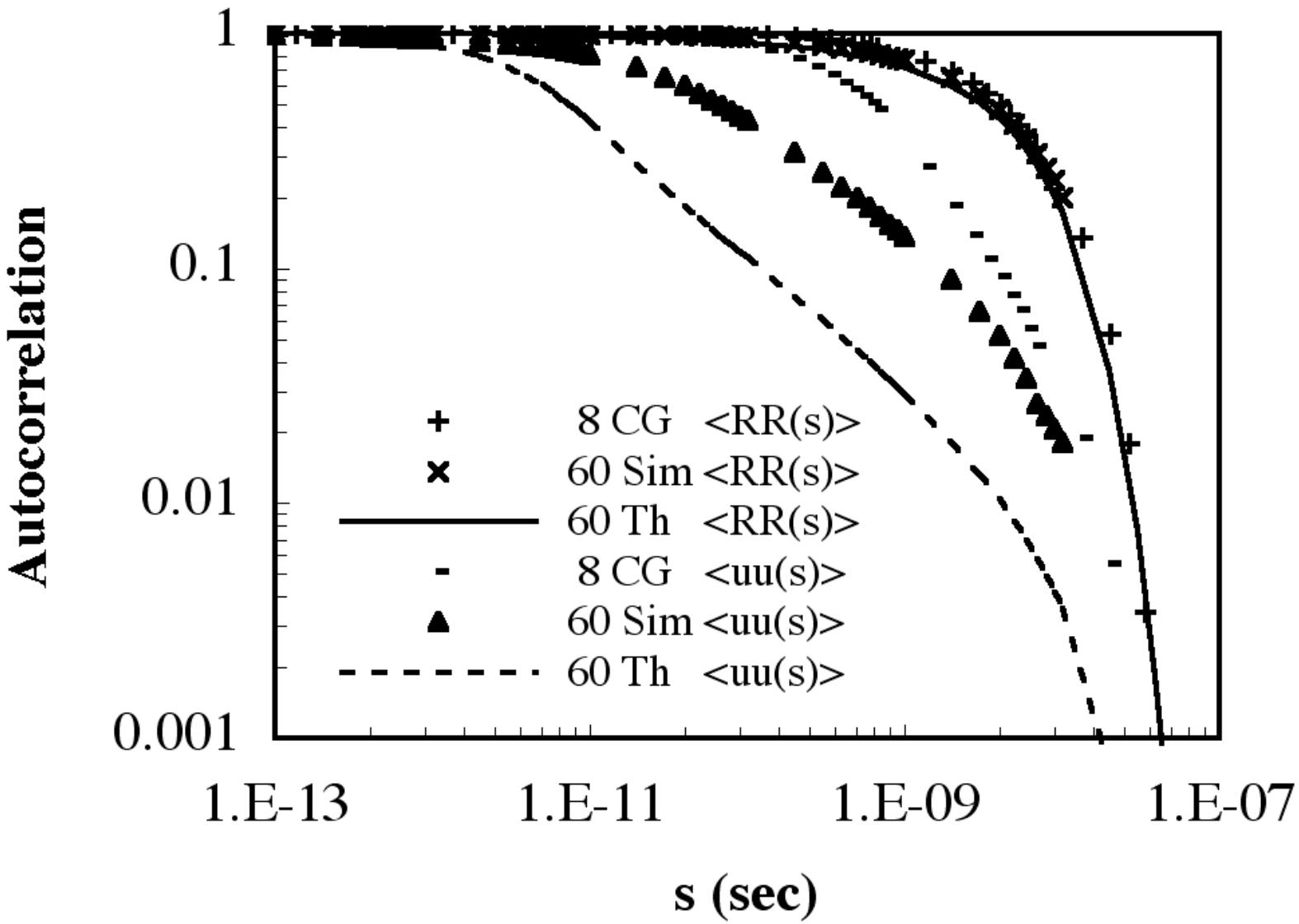

Figure 37. Same as Figure 36 except for 100% gauche/trans barrier height with N_S = 60. These results have been compared with N_S = 8 and b = 8.9934 x 10^{-10} m, i.e., coarse-grained (CG) bonds with only stretching potential acting on them.

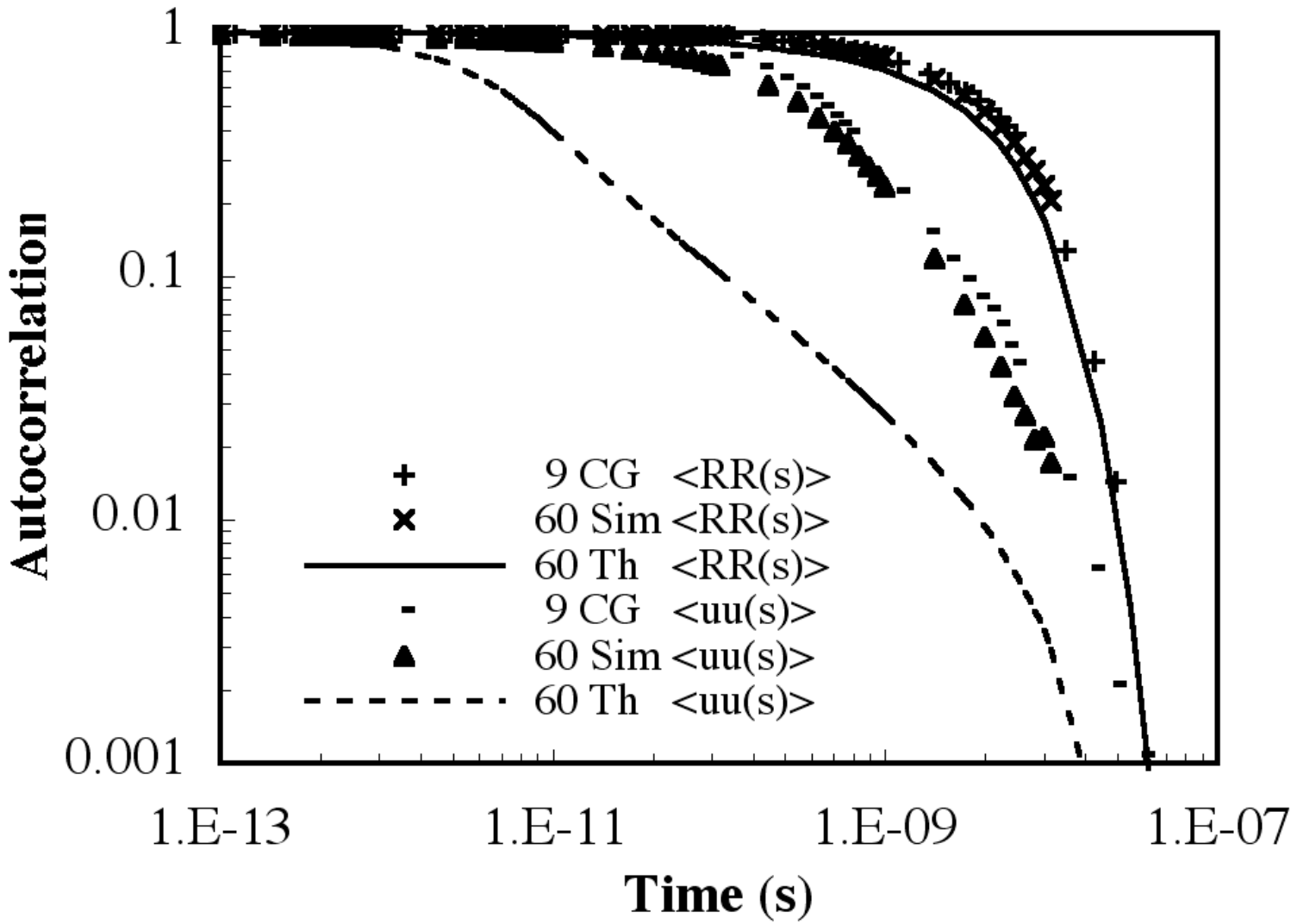

Figure 38. Same as Figure 36 except for 200% gauche/trans barrier height with N_S = 60. These results have been compared with N_S = 9 and b = 8.0088 x 10^{-10} m, i.e., coarse-grained (CG) bonds with only stretching potential acting on them.

intermediate time scale relaxation processes. I apply his approach to my more realistic simulations by fitting the normal mode relaxation rates for different models—stretching force only, stretching and bending forces, and stretching, bending, and torsional forces with different trans/gauche barrier heights—to a single exponential having a pre-factor c_F^k and relaxation rate ν_F^k for each mode k. I find, as expected, that a single exponential provides a very good fit to each of the normal mode relaxation functions. The normal mode relations are computed as follows:

$$\left\langle q_k q_k(s)\right\rangle \equiv \frac{\int_{t=0}^{t=D-s} \underline{q}_k(t) \bullet \underline{q}_k(t+s)\ dt}{\int_{t=0}^{t=D-s} \underline{q}_k(t) \bullet \underline{q}_k(t)\ dt} = c_F^k\ \exp\left(-\nu_F^k s\right) \tag{67}$$

where

$$\underline{q}_k = \sum_{i=1}^{i=N_S} Q_{ki} \underline{R}_S^i \tag{68}$$

$$Q_{ki} = \sqrt{\frac{2}{N_S+1}} \sin\left(\frac{\pi\ k\ i}{N_S+1}\right) \tag{69}$$

The modal relaxation rates are given in Figure 39 which also show a pattern similar to Fixman's [13] observations who simulated a polymer chain with 90^0 bending angle.

Next, I compare in Figure 40 the amplitude of the above modes computed for a chain in dilute solution with the mode amplitudes for chains in the melt state [48] using:

$$\left\langle X_k X_k(s)\right\rangle \equiv \int_{t=0}^{t=D-s} \overline{X_k}(t) \bullet \overline{X_k}(t+s)\ dt = c_K^k\ \exp\left(-\nu_K^k s\right) \tag{70}$$

where

$$\overline{X_k}(t) = \frac{1}{N_S+1} \sum_{i=1}^{i=N_S+1} \cos\left(\frac{\pi\ k\ (i-0.5)}{N_S+1}\right) \underline{r}_i(t) \tag{71}$$

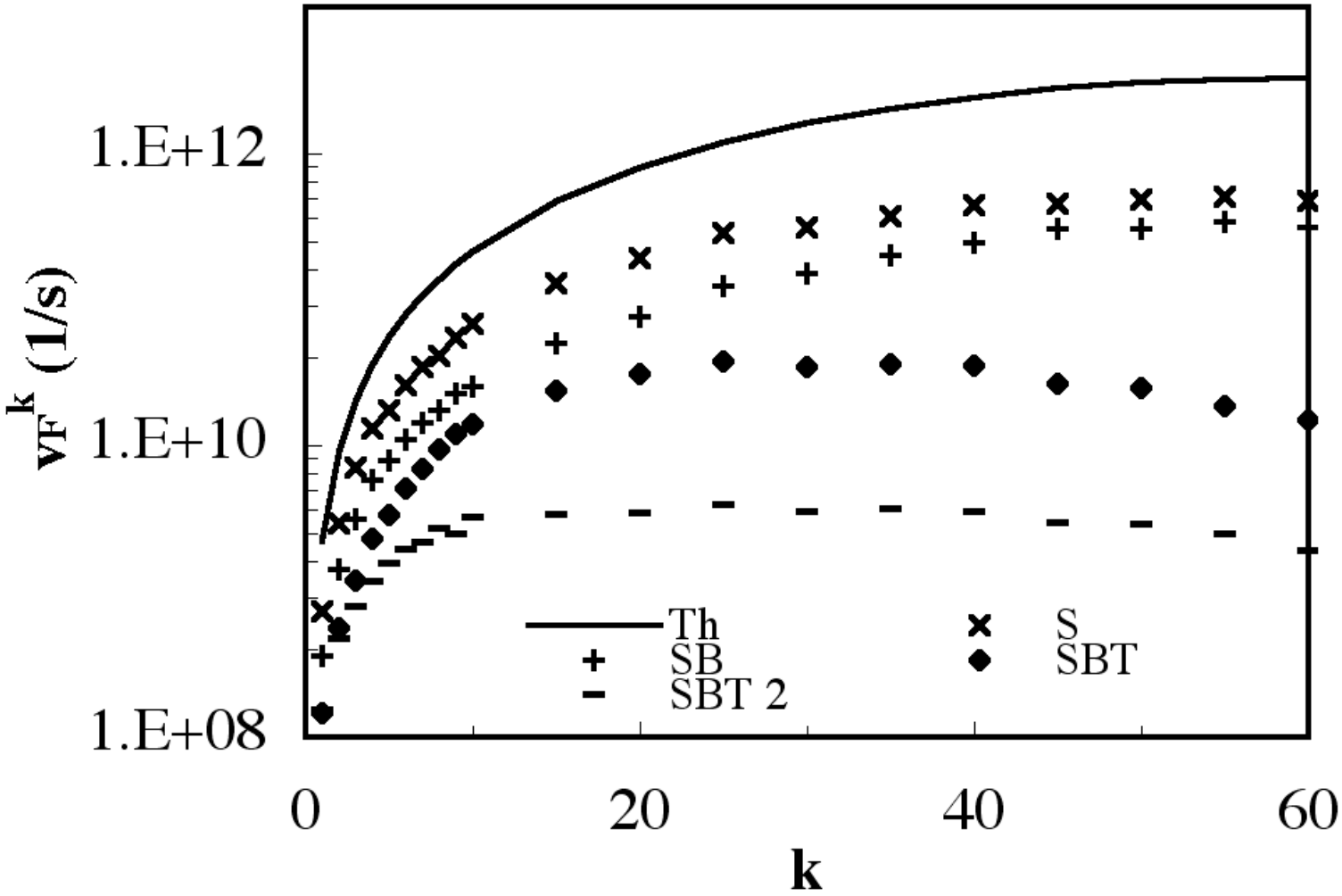

Figure 39. Bond relaxation rate using Fixman's correlation for 60 springs with just the stretching potential (S), stretching and bending potentials (SB), and stretching, bending, and torsional potentials with gauche/trans barrier heights of 100% (SBT) and 200% (SBT 2) of the base barrier height.

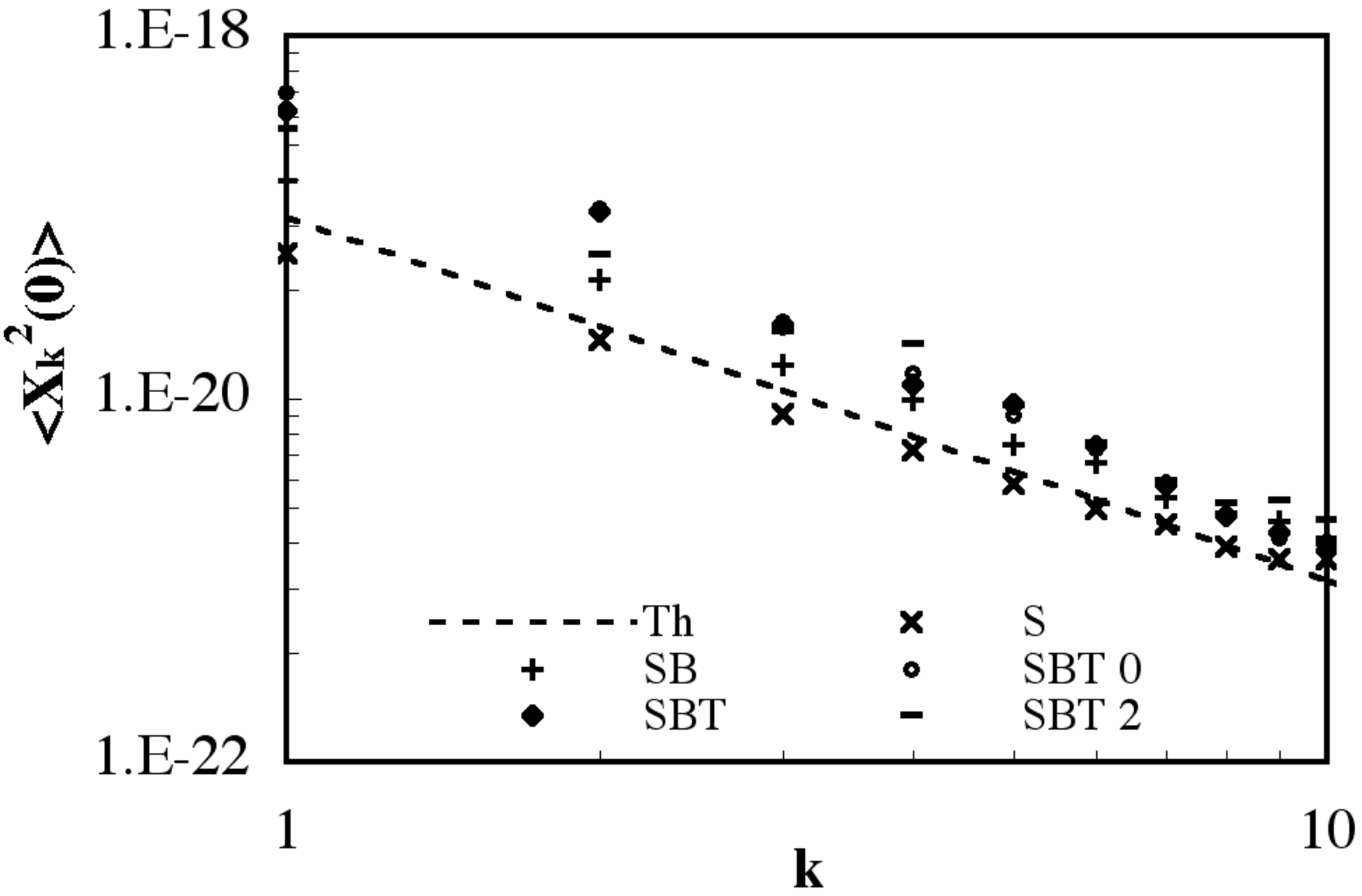

Figure 40. Amplitude of the bond relaxation for 60 springs with just the stretching force (S), stretching and bending forces (SB), and stretching, bending, and torsional forces with gauche/trans barrier heights of 0% (SBT 0), 100% (SBT), and 200% (SBT 2) of the base barrier height. Dashed line indicates the m = -2 scaling expected from Rouse theory (Th).

To check my calculations, I compare my results of $\left\langle \left(\underline{X}_1(0)\right)^2 \right\rangle$ to the theoretical [48] scaling $\left\langle \left(\underline{X}_1(0)\right)^2 \right\rangle \approx \left\langle R^2 \right\rangle_0 / 2\pi^2$, where $\underline{R}$ is the end-to-end vector of the chain, and find my results are in good agreement. My calculations indicate that the amplitude of relaxation decays in the range of k^{-1} to k^{-2}—close to k^{-2} expected from the Rouse theory [48, 49]—but in contrast to melts where decay rate changes from k^{-2} for slower relaxation modes to k^{-3} for faster modes [48].

3.4.3. Structure function

The dynamics of polymers in dilute solution can be probed not only by linear viscoelastic measurements but also by measurements of dynamic scattering functions such as those obtained by neutron spin echo experiments [50]. These experiments have shown that in dilute solution the dynamic structure factor closely follows the standard dilute solution theory of Zimm [5]. The Zimm theory, while being based on a coarse-grained bead-spring chain just like the Rouse theory, differs from the Rouse theory by its additional inclusion of hydrodynamic interactions. Hence, based on my simulations, one might have expected to see in the experiments large deviations from the Zimm theory in the dynamic structure factor at large values of the scattering wave number, q. However, such deviations were not seen [50]. To investigate further, I calculate the scattering function in the dilute region using [51]:

$$S\left(\underline{q}, s\right) = \frac{1}{N_S} \sum_{i,j=1}^{i,j=N_S} \exp\left[i\underline{q} \bullet \left\{ \underline{R}_i^S\left(t+s\right) - \underline{R}_i^S\left(t\right) \right\} \right] \tag{72}$$

which can be simplified for the case of a single chain in dilute solution as [52]:

$$S(\underline{q},s)=\begin{cases}1+4\pi\int_{r=0}^{r=\infty}r^2g(r,s)\dfrac{\sin(qr)}{qr}dr\approx 1+4\pi\sum_{r=0}^{\infty}r^2g(r,s)\dfrac{\sin(qr)}{qr}\Delta r, & s=0\\ 4\pi\int_{r=0}^{r=\infty}r^2g(r,s)\dfrac{\sin(qr)}{qr}dr\approx \quad 4\pi\sum_{r=0}^{\infty}r^2g(r,s)\dfrac{\sin(qr)}{qr}\Delta r, & s\neq 0\end{cases} \tag{73}$$

Here, *g(r, s)* is the radial distribution function of the spring length which is computed as [52, 53]:

$$g(r,s)=\begin{cases}\dfrac{\sum_{t=0}^{t=D}\sum_{i=1}^{i=N_S}\sum_{j=1,i\neq j}^{j=N_S}\delta\left[\underline{r}+\underline{r}_i(t)-\underline{r}_j(t)\right]}{4\pi r^2N_SDdr}, & s=0\\ \dfrac{\sum_{t=0}^{t=D-s}\sum_{i=1}^{i=N_S}\sum_{j=1}^{j=N_S}\delta\left[\underline{r}+\underline{r}_i(t+s)-\underline{r}_j(t)\right]}{4\pi r^2N_S(D-s)dr}, & s\neq 0\end{cases} \tag{74}$$

where

$$\delta[\underline{x}]=\begin{cases}1 & if\ \ |\underline{x}|\in[r,\ r+\Delta r)\\ 0 & otherwise\end{cases} \tag{75}$$

δ is a probability distribution function that measures if a pair of beads is present in the spherical shell contained between radii r and $r+\Delta r$ where Δr is an infinitesimal increment in the spherical radius. Theoretically, $\Delta r\to 0$ but for simulation one needs a finite value, so, I have taken a very small value $\Delta r=0.02b$ where b is the ideal spring length, 1.53 $\overset{0}{\text{A}}$.

The scattering function, $S(q,t)$, is plotted against time made dimensionless using the wave number, q, and center-of-mass diffusivity $D_G=k_BT/\zeta_T$ where $\zeta_T=(N_S+1)\zeta$ is the drag coefficient of the whole chain. Figure 41 has my analysis on experimental data of melts [48] and Figure 42 has data for 60-spring chain with and without the bending and torsional potentials at a small and large value of q—which is related to the inverse of the chain's radius of gyration. In dimensionless form, when q is increased from 5x10^8 m^{-1}

to 3 x 10^9 m^{-1} with only the stretching force present, the data for all values of q collapses nearly perfectly on the same curve that is close to a single exponential decay. When bending and torsional forces are added, I observe that the relaxation of the scattering function at the smallest q value in this analysis, i.e., 5 x 10^8 m^{-1}, is the same as the relaxation with only stretching force present. However, at larger q values, I do see some speed-up in relaxation when bending and torsional forces are present. The similarity of these results plotted on this dimensionless time scale and the near-exponential decay imply that the scattering function is reflecting primarily the center-of-mass diffusion whose rate scales as q^2. This is precisely the behavior recorded by Ewen and Richter [50] in Figure 43 in neuton spin echo experiments for short chains in dilute solutions which are comparable to the chain lengths simulated here. For longer chains, at larger q, the scattering function decays more rapidly which reflects sub-diffusive motion of portions of the polymer coil and is in agreement with the Zimm theory. This is what is seen in Figure 41 when analysis is carried out for melts showing a nearly perfect collapse on a single exponential curve when dimensionless time scales as $\sim q^3$. However, for shorter chains, this sub-diffusive behavior is not observable and only scaling similar to that shown in Figure 42 is seen which indicates that the scattering function is not sensitive to the rotational restrictions on bond orientation that show up in the bond vector autocorrelation function and the mechanical stress. This is not surprising since the scattering function tracks only relative motion of mass centers which are able to diffuse collectively in space even if the bonds connecting them suffer significant restrictions on their orientational rearrangements. Hence, there is no contradiction between the dramatic

changes that bending and torsional potentials induce in orientational dynamics and the rather minor effect that they have on the decay of the scattering function.

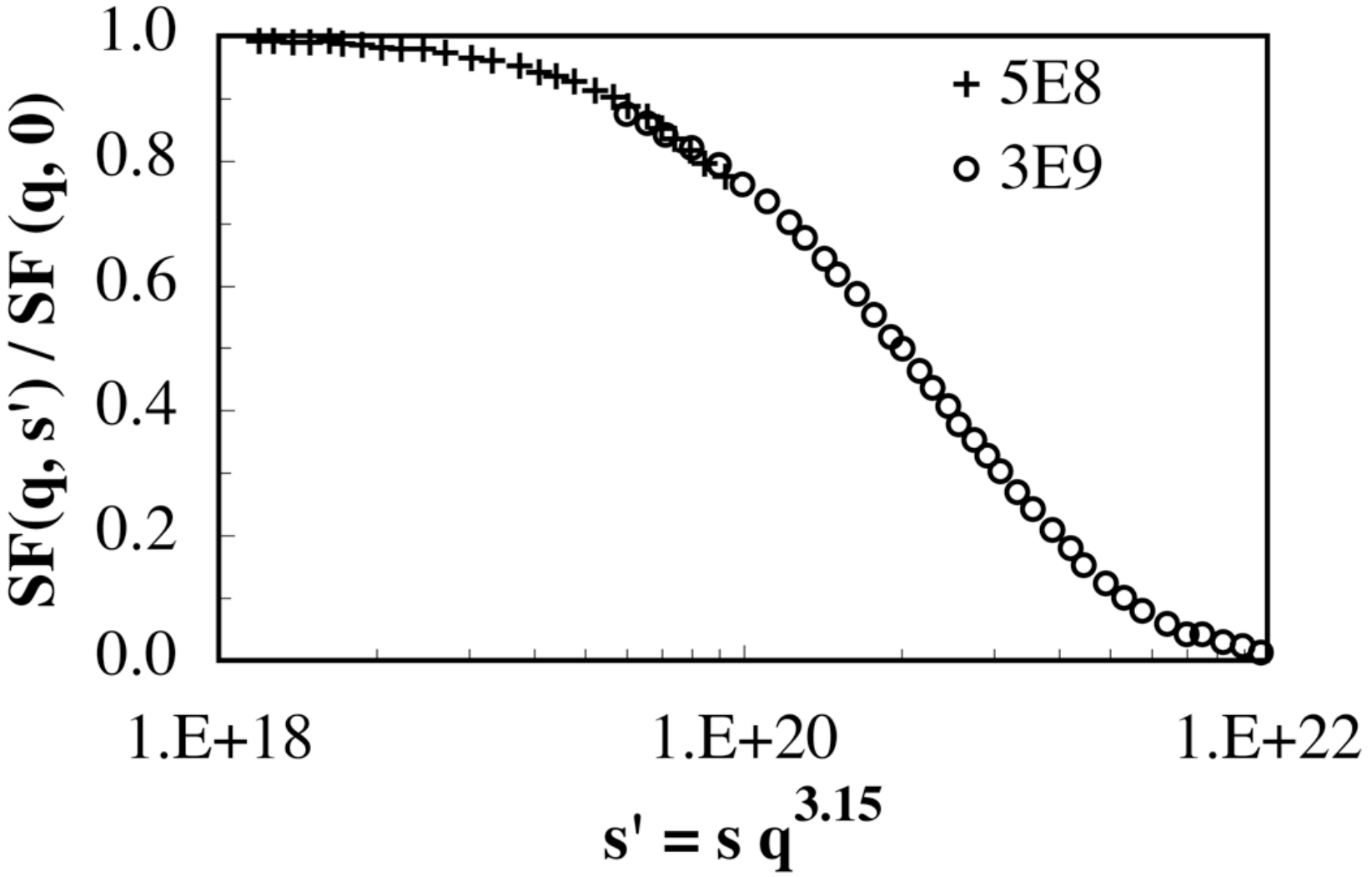

Figure 41. Scaling of structure function calculation of melts using single-chain coherent intermediate scattering function for the CRC1 model at 353 K (Kruhev et al., 2002).

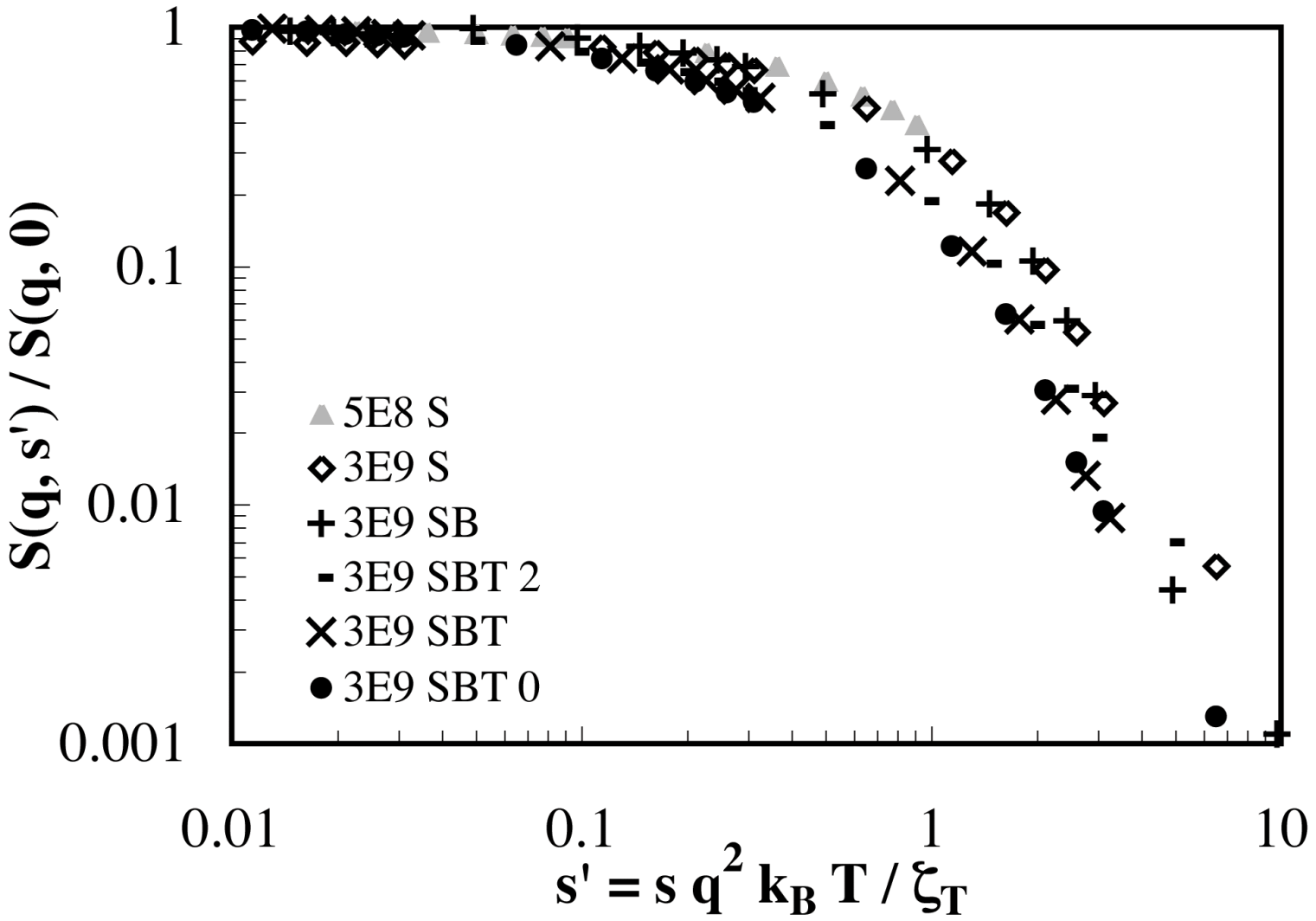

Figure 42. Structure factor calculations for dilute polymer chains when N_S = 60 with just the stretching force (S), stretching and bending forces (SB), and stretching, bending, and torsional forces with the gauche/trans barrier height at 0% (SBT 0), 100% (SBT), and 200% (SBT 2) of the base barrier height when the wave number, q, is 5×10^8 m^{-1} and $q = 3 \times 10^9$ m^{-1}.

Chapter 4

Conclusions

To explain the absence of high frequency relaxation modes in linear viscoelasticity of dilute solutions observed in conventional polymers such as polystyrene, I first test if this is also applicable on another stiff polymer which is expected to behave like an ordinary polymer—single-strand DNA. Then, I use a locally realistic "microscopic" model to analyze the local relaxation of small number of bonds.

To study single-strand DNA, I use the normal mode analysis using the bead-spring model and compare my results using global best-fit, selective best-fit, and individual best-fit parameters to linear viscoelastic measurements of chain end diffusivity for ss-DNA molecules of three different lengths. I find the hydrodynamic behavior of ss-DNA exhibits behavior similar to that of polystyrene in a good solvent in that the experimental MSD versus time has slopes of 0.69 and 1 at the intermediate and longest times, respectively, which are in agreement with the predictions of the Zimm theory. The root mean square error between predictions and experimental data is minimized for $h^* \sim 0.14$ (global best-fit) or $h^* \sim 0.12$ (selective best-fit) while h^* is optimized for individual strands when h^* is between 0.11 and 0.14. These values are close to the value $h^* = 0.15$

observed for viscoelastic properties of polystyrene, indicating that ss-DNA exhibits good solvent hydrodynamic behavior similar to that of polystyrene in Aroclor. This observation is supported by C_∞ values indicating a swollen coil and the diffusion coefficient follow the good solvent scaling laws. Since the optimum number of springs for the strands containing 2400, 6700, and 23100 bases are 6, 17, and 58 respectively, relatively few viscoelastic modes exist in ss-DNA molecules even for strands having thousands of bases. Finally, difficulty in performing high-precision measurements at intermediate and short times may have led to some inaccuracies in experimental data. The smallest coils diffuse fastest at long times for both experimental and simulated results. At intermediate times, this trend reverses for the simulated results. But for the experimental results, this reversal is absent and instead the data seems to merge onto a common curve. This deviation could possibly be a limitation of the model although the model is able to accurately predict the entire MSD trend for all chains when fits are made to each chain independently. On the other hand, experimental data is uncertain for the longest 23100-bases strand and there is significant scatter at short times.

Thus, my proposed method of using the bead-spring model combined with a normal-mode analysis to predict the viscoelastic properties of ss-DNA predicts similarities in the best-fit model parameters of ss-DNA and polystyrene. Although the effective Kuhn length of ss-DNA is much longer than that of polystyrene, these two flexible molecules have similar hydrodynamic behavior in some respects. What is remarkable is how the linear viscoelasticity of ss-DNA can be predicted very accurately for the entire frequency domain with very few springs indicating an absence of high frequency modes in dilute solutions—very similar to observations made on ordinary flexibible polymers.

Next, using a locally realistic "microscopic" bead-spring model with stretching, bending, and realistic torsional potentials, I show that local relaxations of small numbers of bonds—corresponding to normal modes with large mode number—are slowed greatly by the bending and torsional potentials, pushing the relaxation times for local modes towards the terminal region for short chains. This effect is more pronounced when the gauche/trans torsional barrier height is increased with large deviations from Rouse model predictions being observed for all but the slowest mode for chains containing up to 60 bonds.

I tested a standard coarse-graining method that replaces the locally realistic chain constrained by bending and torsional potentials by a coarse-grained freely-jointed chain. The length of each coarse-grained bond and the number of fine-grained bonds replaced by each CG bond are chosen to achieve a match of the CG model to the fine-grained model in the equilibrium coil size and in the fully stretched length of the chain. I find that the CG model is typically not able to capture accurately the dynamics of the fine-grained model except at long times. Thus, coarse-graining a polymer to a freely-jointed (bead-rod) chain might not always be a very successful strategy for reducing polymer degrees of freedom while preserving accuracy. In fact, data for polystyrene and polyisoprene in dilute solution show that the simple bead-spring model, with around 100 bonds subsumed into a single spring, might be a more successful coarse-grained model for describing linear viscoelasticity than is the bead-rod model.

My results help explain why the viscoelasticity of dilute polymer solutions shows less evidence of local motion in dilute solutions than is observed in melts of the same polymers. The reason apparently lies in the greater slowdown, in dilute solutions relative

to the melt, of local motions caused by bending and torsional barriers to bond motion. In both dilute solutions and melts, slow small-*k* modes involving collective motion of many bonds are controlled entirely by diffusive resistance to motion which is proportional to solvent viscosity and not influenced by bending and torsional barrier heights. These slow modes therefore follow Rouse theory, which includes only viscous diffusional resistance to bead motion and ignores rotational barriers. However, in dilute solutions, local, large-*k* modes, which according to the Rouse theory should be very fast, are slowed down so much by bending and torsional barriers that their relaxation rates are similar to those of collective small-*k* modes, and hence are not distinguishable from the low-*k* modes in the viscoelastic spectrum. Thus, the viscoelastic spectrum resembles that of a bead-spring model with a limited number of springs.

For a melt, there is no solvent to set the diffusive time scale of the slow modes, and so this time scale must be set self-consistently by the collective motions of the chains in a "micro-environment." This effective viscosity of the micro-environment (which sets the monomeric friction coefficient used in the Rouse theory for melts) is typically high enough that the relaxation rate of small-*k* collective modes is slower than that of the local, high-*k* modes, and so these high-*k* modes are distinguished from the low-*k* modes in the viscoelastic spectrum for melts. In effect, the "viscosity" governing local bond rotations is smaller than that of the micro-environment controlling larger scale motions so that even when slowed by rotational barriers, the local motions remain faster than the longer-range relaxations in the melt. Thus, local dynamics are readily distinguished for melts at short times in the viscoelastic spectrum. For dilute solutions, these dynamics occur nearly

simultaneously with more global motions and hence are not readily discernable in the viscoelastic spectrum.

Bibliography

1. Arrighi, V., Ganazzoli, F., Zhang, C., and Gagliardi, S., New interpretation of local dynamics of poly(dimethyl siloxane) observed by quasielastic neutron scattering, *Physical Review Letters*, **90**, 5 (2003) 058301-1 - 058301-4.

2. Fukuzawa, K., Itoh, S., and Mitsuya, Y., Fiber wobbling shear force measurement of nanotribology of confined lubricant molecules, *IEEE transactions on magnetics*, **39**, 5 (2003) 2453 - 2455.

3. Tsujita, Y., Gas sorption and permation of glassy polymers with microvoids, *Progress in polymer science*, **28**, 9 (2003) 1377 - 1401.

4. Rouse, P. R., A theory of the linear viscoelastic properties of dilute solutions of coiling polymers, *Journal of chemical physics*, **21**, 7 (1953) 1272 - 1280.

5. Zimm, B. H., Dynamics of polymer molecules in dilute solution: viscoelasticity, flow birefrigence and dielectric loss, *Journal of chemical physics*, **24**, 2 (1956) 269 - 278.

6. Amelar, S., Eastman, C. E., Morris, R. L., Smeltzly, M. A., Lodge, T. P., and Meerwall, E. D. V., Dynamics properties of low and moderate molecular weight polystyrenes at infinite dilution, *Macromolecules*, **24**, (1991) 3505 - 3516.

7. Lodge, A. S., and Wu, Y.-J., Exact relaxation times and dynamic functions for dilute polymer solutions from the bead/spring model of rouse and zimm, Society of Rheology's Winter meeting, Salt Lake City, (1971).

8. Lodge, T. P., Miller, J. W., and Schrag, J. L., Infinite-dilution oscillatory flow birefringence properties of polystyrene and poly(a-methylstyrene) solutions, *Journal of polymer science: polymer physics edition*, **20**, (1982) 1409 - 1425.

9. Peterson, S. C., Echeverria, I., Hahn, S. F., Strand, D. A., and Schrag, J. L., Apparent relaxation-time spectrum cutoff in dilute polymer solutions: an effect of solvent dynamics, *Journal of polymer science: Part B: Polymer physics*, **39**, (2001) 2860 - 2873.

10. Tsunashima, Y., Polymer chain dynamics in diulte solution under Couette flow. II. High molecular weight poly(a-methylstyrene) in good solvent, *Journal of chemical physics*, **114**, 20 (2001) 9163 - 9169.

11. Fixman, M., Brownian dynamics of chain polymers, *Faraday Discuss. Chem. Soc.*, **83**, (1987) 199 - 211.

12. Fixman, M., Simulation of polymer dynamics. I. General theory, *Journal of chemical physics*, **69**, 4 (1978) 1527 - 1537.

13. Fixman, M., Simulation of polymer dynamics. II. Relaxation rates and dynamic viscosity, *Journal of chemical physics*, **69**, 4 (1978) 1538 - 1545.

14. Shusterman, R., Alon, S., Gavrinyov, T., and Krichevsky, O., Monomer dynamics in double- and single-stranded DNA polymers, *Physical Review Letters*, **92**, 4 (2004) 048303: 1 - 4.

15. Li, L., Larson, R. G., and Sridar, T., Brownian dynamics simulations of dilute polystyrene solutions, *Journal of rheology*, **44**, 2 (2000) 291 - 322.

16. Shusterman, R., Alon, S., Gavrinyov, T., and Krichevsky, O., Erratum: Monomer dynamics in double- and single-stranded DNA polymers, *Physical Review Letters*, **98**, 2 (2007) 029901.

17. Larson, R. G., An explanation for the high-frequency elastic response of dilute polymer solutions, *Macromolecules*, **37**, (2004) 5110-5114.

18. Peters, E. A. J. F., Polymers in flow: modeling and simulation, Institution, Delft, Netherlands (2000).

19. Larson, R. G., Principles for coarse-graining polymer molecules in simulations of polymer fluid mechanics, *Molecular Physics*, **102**, 4 (2004) 341 - 351.

20. Kramer, H. A., The behavior of macromolecules in inhomogeneous flow, *Journal of chemical physics*, **14**, 7 (1946) 415 - 424.

21. Kuhn, W., The shape of fibrous molecules in solution, *Kolloidzschr*, **68**, (1934) 2.

22. Kuhn, W., and Grun, F., Relationships between elastic constants and stretching double refraction of highly elastic substances, *Kolloid Zeitschrift*, **101**, 3 (1942) 241 - 332.

23. Kuhn, W., and Grun, F., Statistical behavior of the single chain molecule and its relation to the statistical behavior of assemblies consisting of many chain molecules, *Journal of polymer science*, **1**, 3 (1946) 183 - 199.

24. Flory, P. J., Statistical mechanics of chain molecules, Wiley, New York (1969).

25. Flory, P. J., Statistical mechanics of chain molecules, Oxford University Press, New York (1988) 16 - 26.

26. Treloar, L. R. G., The elasticity and related properties of rubbers, *Reports on Progress in Physics*, **36**, 7 (1973) 755 - 826.

27. Ottinger, H. C., Stochastic processes in polymeric liquids, Springer, Berlin (1996).

28. Larson, R. G., The rheology of dilute solutions of flexible polymers: progress and problems, *Journal of rheology*, **49**, 1 (2004) 1 - 70.

29. Kim, S., and Karrila, S. J., Microhydrodynamics: Principles and selected applications, Butterworth-Heinemann, MA (1991).

30. Larson, R. G., The structure and rheology of complex fluids, Oxford University Press, New York (1999).

31. Doi, M., and Edwards, S. F., The theory of polymer dynamics, Calrendon Press, Oxford (1986).

32. Teraoka, I., Polymer Solutions: An introduction to physical properties, John Wiley & Sons, New York, NY (2002) 235.

33. Press, W. H., Numerical recipes in fortran 77: the art of scientific computing, 2nd, **1**, Cambridge university press, New York (1996).

34. Ferry, J. D., Viscoelastic properties of polymers, 3rd, Wiley, New York (1980).

35. Johnson, R. M., Schrag, J. L., and Ferry, J. D., Infinite-dilution viscoelastic properties of polystyrene in theta-solvents and good solvents, *Polymer Journal (Tokyo, Japan)*, **1**, (1970) 742 - 749.

36. Krichevsky, O., Comments on experimental data measured by Shusterman et al. (2004) Personal communication., Receipent, Comments on experimental data measured by Shusterman et al. (2004) Personal communication. (Personal communciation).

37. Tinland, B., Pluen, A., Sturm, J., and Weill, G., Persistence length of single-stranded DNA, *Macromolecules*, **30**, (1997) 5763-5765.

38. Bockelmann, U., Ezzevaz-Roulet, B., and Heslot, F., DNA strand separation studied by single molecule force measurements, *Physical Review E*, **58**, 2 (1998) 2386 - 2394.

39. Zhang, Y., Zhou, H., and Ou-Yang, Z.-C., Stretching single-stranded DNA: interplay of electrostatic, base-pairing, and base-pair stacking interactions, *Biophysical journal*, **81**, (2001) 1133 - 1143.

40. Bekker, H., Berendsen, H. J. C., and Gunsteren, W. F. v., Force and virial of torsional-angle-dependent potentials, *Journal of computational chemistry*, **16**, 5 (1995) 527 - 533.

41. IUPAC-IUB, Commission on Biochemical Nomenclature, *Biochemistry*, **9**, (1970) 3471.

42. Ryckaert, J. P., and Bellemans, A., Molecular dynamics of liquid n-Butane near its boiling point, *Chemical Physics Letters*, **30**, 1 (1975) 123 - 125.

43. Scott, R. A., and Scheraga, H. A., Conformational analysis of macromoleclues II: The rotational isomeric states of the normal hydrocarbons, *The Journal of Chemical Physics*, **44**, 8 (1966) 3054 - 3069.

44. Helfand, E., Wasserman, Z. R., and Weber, T. A., Brownian dynamics study of polymer conformational transitions, *Macromolecules*, **13**, (1980) 526 - 533.

45. Chopra, M., and Larson, R. G., Brownian dynamics simulations of isolated polymer molecules in shear flow near adsorbing and nonadsorbing surfaces, *Journal of rheology*, **46**, 4 (2002) 831 - 862.

46. Tuzun, R. E., Noid, D. W., and Sumpter, B. G., Efficient computation of potential energy first and second derivatives for molecular dynamics, normal coordinate analysis, and molecular mechanics calculations, *Macromolecular theory simulation*, **5**, (1996) 771 - 788.

47. Larson, R. G., Constitutive equations for polymer melts and solutions, Butterworth Publishers, Stoneham, MA (1988).

48. Krushev, S., Paul, W., and Smith, G. D., The role of internal rotational barriers in polymer melt chain dynamics, *Macromolecules*, **35**, 10 (2002) 4198 - 4203.

49. Faller, R., and Muller-Plathe, F., Modeling of poly(isoprene) melts on different scales, *Polymer*, **43**, (2002) 621 - 628.

50. Ewen, B., and Richter, D., Neutron spin echo investigations on the segmental dynamics of polymer in melts, networks, and solutions, *Advances in Polymer Science*, **134**, (1997) 1 - 129.

51. Putz, M., Kremer, K., and Grest, G. S., What is the entanglement length in a polymer melt? *Europhysics letters*, **49**, 6 (2000) 735 - 741.

52. Binder, K., and Kob, W., Glassy materials and disordered solids, World Scientific Publishing Co. Ltd., Singapore (2005).

53. Allen, M. P., and Tildesley, D. J., Computer simulation of liquids, Oxford University Press, New York (1987).